

AERODYNAMIC CHARACTERIZATION OF FLOW OVER A THREE-DIMENSIONAL
RIGID MICRO AIR VEHICLE WING

By

PARVEZ NAOROZE KHAMBATTA

A THESIS PRESENTED TO THE GRADUATE SCHOOL
OF THE UNIVERSITY OF FLORIDA IN PARTIAL FULFILLMENT
OF THE REQUIREMENTS FOR THE DEGREE OF
MASTER OF SCIENCE

UNIVERSITY OF FLORIDA

2008

© 2008 Parvez N. Khambatta

To my Family.

ACKNOWLEDGMENTS

I would like to start by thanking Dr. Lawrence Ukeiley for giving me the opportunity to work with and learn from him over the past two years. I would like to thank Dr. Rick Lind, who gave me the opportunity to come and study at University of Florida in Spring 2006, and I would also like to thank Dr. Peter Ifju and Dr. Rick Lind for sitting on my supervisory committee.

Many thanks go to Bret Stanford and members at the MAV lab in Gainesville, who manufactured the carbon fiber wing models for these experiments. I would also like to thank Mr. William Clements and Mr. Richard Runyon for their assistance with machining parts for the experiments and for maintaining the wind tunnel facilities.

I would also like to thank Dr. Charles Tinney for his expertise and advice with regard to the flow measurements. Last but not least, I would like to thank my peers in the Unsteady Fluid Dynamics Group for their support and willingness to lend a hand when I needed it.

Lastly, I would like to thank the Air Force Office of Scientific Research (AFOSR), for funding my studies and my research over the past two years.

TABLE OF CONTENTS

	<u>page</u>
ACKNOWLEDGMENTS	4
LIST OF TABLES	6
LIST OF FIGURES	7
ABSTRACT	10
CHAPTER	
1 INTRODUCTION	12
Motivation for Research	15
Background	16
Outline	25
2 EXPERIMENTAL DETAILS	26
Micro Air Vehicle Wing Model	26
Wind Tunnel Facility	28
Seeding Mechanism	32
Particle Image Velocimetry (PIV) Flow Measurements	36
Errors in the Particle Image Velocimetry (PIV) Measurements	45
3 PARTICLE IMAGE VELOCIMETRY RESULTS AND DISCUSSION	48
Mean Velocity Field	50
Fluctuating Velocity Levels in the Flow	67
Velocity Correlation Analysis	80
Vorticity Calculations	92
4 SUMMARY AND CONCLUSIONS	97
LIST OF REFERENCES	100
BIOGRAPHICAL SKETCH	108

LIST OF TABLES

<u>Table</u>		<u>page</u>
2-1	Locations for two-component PIV measurements.....	44
2-2	Locations for stereoscopic PIV measurements.	45

LIST OF FIGURES

<u>Figure</u>	<u>page</u>
1-1 Ensemble-averaged features of a transitional separation bubble.....	18
1-2 The CFD computational domain and details of the mesh near the wing surface.	21
1-3 CFD streamlines and pressure distribution at various angles of attack.	21
1-4 Flow structure at the root of a rigid UF MAV wing.....	23
2-1 The rigid micro air vehicle wing used in this study.....	27
2-2 The wing mounted in the test section for 3-component PIV.	28
2-3 Photographs of the medium speed wind tunnel facility at UF REEF.....	29
2-4 Photographs showing the flow control mechanism of the wind tunnel.	29
2-5 Horizontal velocity profiles in the z-y plane at $x = 0.1L$	30
2-6 A sample CTA calibration curve	31
2-7 The Laskin nozzle, high-volume liquid droplet seeding generator.....	32
2-8 The cardboard mixing chamber that was assembled to promote uniform seeding.....	33
2-9 Hot-wire, normalized velocity and percentage turbulence profiles	34
2-10 Comparison of the turbulence energy spectra at $x = 0.1L$	35
2-11 Schematics of the PIV setups inside the test section of the wind tunnel.	36
2-12 Images showing planes illuminated by the laser for PIV	37
2-13 A convergence plot of normalized mean vs. sample size	41
2-14 Distribution of estimated vectors in the flow field	43
2-15 Measurement locations for 2-component and 3-component PIV over the wing.....	44
3-1 Examples of ‘bloom’ in the raw data.....	49
3-2 Stream-wise velocity vectors in the flow at various angles of attack.....	51
3-3 Normal velocity vectors in the flow at various angles of attack.....	52
3-4 Identifying the location of the wing-tip vortex center	53

3-5	Distribution of the vertical component in the flow field and estimated vectors at 15°	54
3-6	Distribution of the stream-wise component at $\alpha = 15^\circ$, $x/c = 0.4$ and $x/c = 0.7$	55
3-7	Distribution of the stream-wise component at $\alpha = 15^\circ$, $x/c = 0.8$ and $x/c = 0.9$	55
3-8	The span-wise component and the stream-wise vorticity at $x/c = 0.6$ $\alpha = 15^\circ$	56
3-9	Regions of strong downward and upward flow near the wing-tip at $\alpha = 18^\circ$	58
3-10	Progression of the wing-tip vortex downstream over the wing for $\alpha = 18^\circ$	59
3-11	Span-wise circulation over the wing at $\alpha = 18^\circ$	60
3-12	Stream-wise and normal components of the flow at $\alpha = 25^\circ$, $z/b = 0$ and $z/b = 0.46$	63
3-13	Stream-wise components in the flow at $\alpha = 25^\circ$, $x/c = 0.8$ and $x/c = 1.1$	64
3-14	Flow field distributions for $\alpha = 25^\circ$ and $z/b = 0.42$	65
3-15	Separation bubble at the leading edge of the wing at $\alpha = 25^\circ$ and at $z/b = 0.42$	66
3-16	Span-wise vorticity levels at the leading edge at $\alpha = 25^\circ$, at $z/b = 0.42$ and $z/b = 0.46$	66
3-17	Stream-wise velocity fluctuation levels at various angles of attack	68
3-18	Normal velocity fluctuation levels in the flow field at various angles of attack	69
3-19	Turbulent shear stress levels in the flow at various angles of attack	70
3-20	High fluctuation levels in the stream-wise and normal components $\alpha = 15^\circ$ and 25°	72
3-21	Comparison of the normalized stream-wise turbulence levels at $\alpha = 15^\circ$	74
3-22	Normalized velocity fluctuations at $x/c = 0.3, 0.5$ and 0.8 , at $\alpha = 15^\circ$	75
3-23	Normalized fluctuating velocity levels at $\alpha = 18^\circ$ and $x/c = 1.0$	77
3-24	Fluctuating velocity levels at $\alpha = 18^\circ$; $x/c = 1.1$ and 1.4	77
3-25	Developing fluctuating velocity profiles at $\alpha = 25^\circ$; $x/c = 0.4, 0.6$ and 0.8	79
3-26	Spatial cross correlation in the fluctuating components of the flow at $\alpha = 10^\circ$	81
3-27	Spatial cross correlation in the fluctuating components of the flow at $\alpha = 15^\circ$	82
3-28	Spatial cross-correlations from measurements at $\alpha = 18^\circ$ and $x/c = 0.4$	84
3-29	Spatial cross correlations in the fluctuating span-wise component at $\alpha = 18^\circ$	85

3-30	Development of turbulent structures in the wake at $\alpha = 18^\circ$	86
3-31	Spatial cross correlations at $\alpha = 25^\circ$, at $x/c = 0.6$ and $z/b = 0.08$	88
3-32	Spatial cross correlations at $\alpha = 25^\circ$, at $x/c = 0.8$ and $z/b = 0.08$	88
3-33	Spatial cross correlations in the stream-wise and normal components at $\alpha = 30^\circ$	90
3-34	Development of turbulent structures in the flow at $\alpha = 30^\circ$, $y/c = 0.05$ & $z/b = 0$	91
3-35	Span-wise vorticity at various angles of attack.....	93
3-36	Distribution of the vertical component of the flow at $\alpha = 15^\circ$	95
3-37	Distribution of the span-wise component and the stream-wise vorticity at $\alpha = 21^\circ$	95
3-38	Span-wise vorticity at $\alpha = 25^\circ$, $z/b = 0.42$ and 0.46	96

Abstract of Thesis Presented to the Graduate School
of the University of Florida in Partial Fulfillment of the
Requirements for the Degree of Master of Science

AERODYNAMIC CHARACTERIZATION OF FLOW AROUND A THREE-DIMENSIONAL
RIGID MICRO AIR VEHICLE WING

By

Parvez Naoroze Khambatta

August 2008

Chair: Lawrence Ukeiley
Major: Mechanical Engineering

With an increase in the study and development of Micro Air Vehicles in recent years, the research in this document hopes to shed some light on the flow characteristics of a thin rigid MAV wing. Flow measurements were conducted over the airfoil using 2 & 3-component PIV techniques. The MAV wing has a wingspan of 0.15 m and a nominal chord length of 0.124 m. Experiments were conducted at various angles of attack and at a Reynolds number of $\sim 75,000$ based on the chord length of the wing model. A Dantec Dynamics TR PIV system was used to acquire the data from the experiments and process the particle images into 2 and 3 component velocity fields.

The flow over the wing was described using discussions of the mean velocity field, the fluctuating velocities in the three components of the flow, the turbulence shear stress levels and the out of plane vorticity. Spatial cross correlations were also performed on the results to try and identify dominant length scales within the flow.

The mean velocity fields over the airfoil show an increase in the thickness of the shear layer and the fluctuating velocity levels within as a function of the angle of attack; except at an angle of attack of 18° , where the shear layer is thinner and the velocity fluctuations are of a lower magnitude. The flow over the wing visibly separates from the top surface of the airfoil

between $21^\circ \leq \alpha \leq 25^\circ$. The flow measurements also identified regions of span-wise circulation over the wing caused by the wing-tip vortices. It was also observed that with an increase in the angle of attack, there was an increase in the magnitude of the downward velocities over the top of the wing, due to stronger wing-tip vortices.

Now that the baseline characteristics for a rigid MAV wing have been identified in this research, tests should be performed on flexible membrane wings and the results compared; in an effort to try and identify the flow characteristics that make flexible wings superior to rigid wings in terms of flight characteristics.

CHAPTER 1 INTRODUCTION

Micro Air Vehicles (MAVs) today, are described as aircraft smaller than six inches in any dimension (wingspan, length or height), and are typically designed to complete a mission while carrying a miniaturized payload, simple avionics and a communication link (Mueller & DeLaurier, 2003). This study comprises quantitative flow measurements, to add to the existing knowledge base, above a wing that has been studied extensively from an aerodynamic loads perspective and has been used for MAV flight competitions. The following section provides the reader with insight into some of the characteristics of rigid wing MAVs from previous studies, for the purpose of designing an efficient MAV.

Due to their unique flight characteristics and because they typically have a top speed on the order of 14 m/s or about 30 mph, MAVs operate in what is typically viewed as a low Reynolds numbers regime (less than 150,000), based on mean chord length and nominal cruise speed. The design of vehicles which operate at Reynolds numbers below 150,000 is difficult, largely due to the fact that many of the classical theories which are valid for large Reynolds numbers are not valid in this flight regime, where viscous forces are more dominant (Torres & Mueller, 2000). With their reduced size, MAVs gain favorable scaling characteristics such as low inertia and a reduced stalling speed. However, such a flight regime also tends to be dominated by laminar boundary layer separation, turbulent transition in boundary and the separated free shear layers and low lift-to-drag ratios, leading to a substantial loss in efficiency (Torres, 2002). Many MAV wings also have low Aspect Ratios (AR, defined as the square of the wingspan divided by the total wing area), typically on the order of unity, in effort to maximize the area of the lifting surface while keeping within the specified dimensions (Mueller, 1985). This feature has been historically driven by the need to maximize the wing area while minimizing its maximum

dimension. These Low Aspect Ratio (LAR) wings are prone to the development of strong longitudinal and lateral vortical flow structures over the wing (Shyy et al., 2005), which plays a crucial role in their aerodynamic properties. In fact, this complex, highly three dimensional combination of the separated flow over the wing and the lateral vortices generated at the wing tips can lead to vortex destabilization (Tang & Zhu, 2004) and be the prominent cause for roll instabilities during flight.

The development of MAVs, typically adopt one of the following paths: (1) Using flapping wings for the generation of lift and thrust; (2) Employing the use of rotating wings (as in a micro helicopter); (3) Using a rigid wing for generating conventional lift; (4) Using a membrane wing with rigid reinforcement. From the design point of view, the fixed wing configuration is a tried and true method and is easiest to implement on a MAV due mostly to conventional thinking from the higher Reynolds number counterparts. However, flapping wings, which are difficult to employ due to their complex wing kinematics and power requirements, excel in terms of lift generation and maneuverability at low Reynolds number and are the topic of much ongoing research; but it is a topic that will not be discussed in this paper.

Because of the ease of implementation of a fixed wing and the stall resistant characteristics of a compliant wing, a compromise has been found in flexible membrane wings that have been reinforced with sections of rigid material. It is the deformation in flexible membrane wings that allows for a significant re-distribution of pressure which in turn increases lift and longitudinal static stability when compared to a rigid MAV wing. The simplicity in design of a fixed wing MAV, as a replica of a larger airfoil, is counterbalanced by deterioration in performance due to the development of separation bubbles, as its operating Reynolds number drops to the range of 10^4 to 10^5 (Young & Horton, 1966). Also, aerodynamic problems related to vortex lift on wings

of aspect ratios lower than two, make it difficult to extend existing analytical and empirical techniques to lower Reynolds numbers (Tang & Zhu, 2004).

Geometrically, a high aspect ratio indicates long narrow wings and a low aspect ratio indicates short stubby wings. High aspect ratio wings are commonly found on low speed aircraft such as gliders where a high lift to drag ratio is required. Conversely, low aspect ratio wings are found on supersonic military aircraft where compressibility effects are a major issue. The coefficient of drag, C_D , is inversely related to the AR of a wing. Therefore, for an increase in AR, C_D will decrease. This demonstrates that with an increase in wing area, not only would an aircraft be able to fly slower but it would even require less thrust to maintain forward flight, in the bargain, increasing fuel efficiency with a reduction in the drag coefficient. Overall, LAR wings would provide better pitch stability and maneuverability, whereas a HAR wing would be more efficient in terms of 'lift to drag' ratio.

In recent years, the size restrictions on MAVs have led to the elimination of horizontal stabilizers, resulting in 'flying wing' designs. Such designs require a 'reflexed' airfoil which generates a zero pitching moment under flight. It is the trailing edge curvature beneath the mean chord line that is referred to as the 'reflex' of the airfoil. This wing geometry tends to create negative lift and opposes the pitching moment of the wing in an effort to provide a larger margin of pitch stability (Sytsma, 2006).

Also, the aerodynamics of LAR wings tend to differ drastically from their higher aspect ratio counterparts, exhibiting unique aerodynamic properties such as high-stall angles and non-linear 'lift versus angle of attack' curves (Mueller et al., 2007). These characteristics resemble those seen in delta wings at higher Reynolds numbers and are particularly dominant for wings of AR less than or equal to one (Lissaman, 1983). Furthermore, it is only in the past few decades

that concerted efforts have been made to study and document the behavior of LAR wings at low Reynolds numbers.

Motivation for Research

Laminar boundary layer separation is an integral part of the flow characteristics over low Reynolds number MAV wings. Laminar flow tends to separate under adverse pressure gradients and may thereafter experience a transition in the free shear layer. If there is enough energy via entrainment from the vortical structures in the shear layer, this flow can reattach to the wing's surface as it transitions, which then forms a turbulent boundary layer, leaving behind it a closed circulation bubble, referred to as a 'laminar separation bubble'. Such a condition results in significantly lower drag over the airfoil, than one where the free shear layer is unable to reattach and becomes massively separated. However, there are a number of factors that greatly influence the creation of a 'laminar separation bubble', including Reynolds number, pressure distributions, airfoil geometry, surface roughness, angle of attack, and free-stream turbulence intensity.

A thorough analysis and review of LAR wings was performed by Hoerner and Borst (1975), who presented a variety of correlations, analytical methods and experimental data corresponding primarily to higher Reynolds numbers than those of typical MAVs. However, Torres (2002) later showed that parts of aerodynamic theory still held for MAV flight regimes. This theory correctly predicts that a finite wing of a given aspect ratio generates lift from counter-rotating vortical structures near the wing tips. These vortices tend to strengthen as the angle of attack increases, and for low aspect ratio wings, these tip vortices might be present over a large part of the surface, thus influencing the aerodynamic characteristics of the wing.

It is further believed that wings with aspect ratios smaller than 1.5 tend to exhibit both, linear and non-linear sources of lift. The linear lift is what is commonly observed in the form of circulation around the wing. The non-linear lift is created by the formation of low-pressure cells

on a wing's top surface by tip-vortices, commonly observed in delta wings at high angles of attack. It is this non-linear lift effect that increases the slope of the lift-curve as the angle of attack increases and is what primarily contributes to the high value of stall angle of attack of an LAR wing (Mueller et al., 2007).

To date most of the analysis of flow over these wings has been accomplished through extensive computational fluid dynamics (CFD) methods. These results have been augmented with experiments on the aerodynamic loads and deformations of the wings in various states, however, little quantitative analysis has been performed on experimental data collected from flow measurement techniques such as Particle Image Velocimetry (PIV).

The goal of this research is to take PIV measurements in the flow over an LAR rigid MAV wing to provide a data set which can be used to develop a better understanding of the characteristics of the flow. This will include an attempt to shed some light onto the effect of separation bubbles and tip vortices, amongst other phenomenon, on the flight performance of rigid airfoils used on MAVs. Additionally this data set will provide a benchmark from which results from current CFD models can be validated, specifically that of Stanford et al (2007) who has been studying the exact wing used in this study.

Background

In the following section there will be a review of past studies that have lead to the design of low aspect ratio cambered airfoil that is being examined in this study. The innovative research performed on low Reynolds number airfoils is most pertinent to the design of efficient MAV airfoils today (Schmitz, 1953). Schmitz measured the aerodynamic characteristics of several airfoil geometries including thin-flat and thin-cambered plates over Reynolds numbers ranging from 21,000 to 168,000 (Mueller et al., 2007). Research continued by B. H. Carmichael in the 1980s showed that for the range of Reynolds numbers between 30,000 and

70,000 the choice of airfoil section is very important because relatively thick airfoils (6% and above) can have significant hysteresis in lift and drag forces caused by separation and transition of laminar to turbulent flow (Mueller, 1985). It was also observed that below chord Reynolds numbers of $\sim 50,000$, the free shear layer after laminar separation would not be able to transition to turbulent flow in time to reattach to the airfoil surface. When the point of separation is as far upstream as the leading edge of the airfoil, there is decrease in lift and a simultaneous increase in drag, a condition where the airfoil is said to be stalled. At chord Reynolds numbers between the range of 70,000 to 200,000 (the regime in which most MAVs operate), extensive laminar flow is usually observed and airfoil performance is greatly increased unless the presence of a laminar/transition separation bubble for that airfoil causes excessive drag.

It is the post separation behavior of the laminar boundary layer over an airfoil that leads to deterioration in its performance at low Reynolds numbers and results in an increase in drag and a decrease in lift over the entire airfoil (Mueller, 1999). In this flow regime, the boundary layer on an airfoil often remains laminar downstream of the minimum pressure and then separates, which in turn forms a shear layer, the moment it starts running into an 'adverse' pressure gradient. As previously mentioned, for Reynolds numbers below 50,000, this separated shear layer does not reattach. However, at Reynolds numbers greater than 50,000, transition typically takes place in the separated shear layer and provided that the adverse pressure gradient is not too large, the flow can recover sufficient energy through entrainment to reattach to the airfoil surface. Thus, over a short period of time, a region of re-circulating flow is observed, as shown in Figure 1-1 (Horton 1968), and because this bubble acts as a boundary-layer trip, the phenomenon is referred to as a transitional separation bubble. At low Reynolds numbers, a transitional bubble can

occupy anywhere from 15%–40% of the airfoil surface, in which case it is referred to as a long bubble.

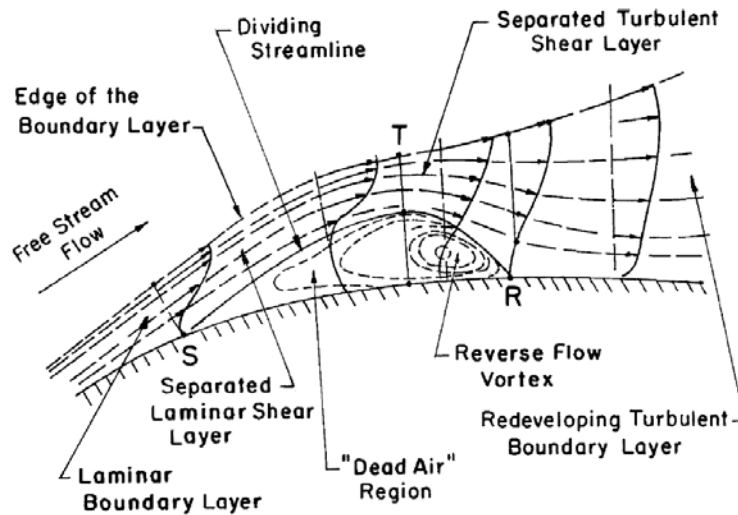


Figure 1-1. Ensemble-averaged features of a transitional separation bubble (adapted from Horton, 1968).

As can be imagined, a separation bubble has a great deal of effect on the flow and stall characteristics of an airfoil at different angles of attack. At higher Reynolds numbers a short bubble is observed near the leading edge of a wing and is usually 2-3% of the chord length. In such cases the lift is noted to increase linearly with angle of attack until stall occurs. This is referred to as the bursting of the short bubble. On the other hand, when a long bubble tends to form over the wing surface, usually at low Reynolds numbers, a stall condition occurs when the bubble extends all the way to the trailing edge of the airfoil (Mueller, 1985). The length of the two types of bubbles is linearly proportional to their thicknesses, and increasing turbulence levels in the tunnel tends to decrease bubble thickness. Therefore, by comparing the characteristics of the separation bubble of a standardized airfoil to another airfoil at a particular Reynolds number can provide a quantitative comparison of the flow quality in different low Reynolds number facilities. The bubble behavior is inherently unsteady, and in some cases the flow will have an

oscillatory reattachment behavior. These bubbles are also typically characterized by a constant pressure distribution applied along the airfoil. The formation of the separation bubbles also tends to be path dependent, hence significant hysteresis in the lift curve will often exist for low Reynolds number airfoils (Mueller, 2003).

As can be seen in Figure 1-1, the flow becomes unsteady downstream of the point of maximum vertical displacement of the bubble (labeled as point T in Figure 1-1). However, it is steady upstream of T, where the transition from laminar to turbulent flow is thought to take place. Hence, accurate prediction of the existence and extent of a separation bubble is necessary when implementing an efficient design for a low-speed airfoil (Brendel, 1988).

When employing a MAV design, it is necessary to obtain characteristic data about the aircraft using physical and/or numerical experiments. Many designers of rigid wing MAVs use the 'Eppler Airfoil Design and Analysis' code or the 'Drela XFOIL' code to obtain a suitable wing cross section and then select a planform, after which they experiment to arrive at the final three-dimensional wing shape. These programs allow for the input of a number of parameters, such as the basic airfoil geometry, the operating Reynolds number, angle of attack, etc... In fact, the designers of XFOIL claim that the flow characteristics of "thin indoor-model wing airfoils can be predicted reasonably well" (even around Reynolds number of 10^3 , XFOIL 6.4 Help File, 1994). Numerical outputs from programs like this can allow one to investigate specific areas of interest, such as the onset of separation over an airfoil, etc.

Research by Torres and Mueller (2004) provides aerodynamic data corresponding to LAR wings at low Reynolds numbers for the purpose of supporting the analysis of small aircraft operating at low speeds. The data are based on wind-tunnel experiments of flat-plate wings with 2% thickness and aspect ratios between 0.5 and 2.0 on four distinct planforms. Discussion of the

data includes identification of key performance parameters, such as lift-curve slope, drag characteristics, comparison with nonlinear lift theories, maximum lift coefficient and corresponding angle of attack, and location of the center of lift (Torres *et al*, 2004). While the aerodynamic information is important using quantitative flow measurements there is still much to be learned.

Computational fluid dynamics (CFD) studies performed by Viieru (2006) on very thin undercambered MAV wings shows a distinctive laminar separation behavior (with a wing thickness of 0.3% of chord length). To do this, a moving grid, 3D, unsteady, incompressible Navier-Stokes solver was used with a capability for turbulence modeling to simulate the airflow over a MAV wing (similar to the one studied here). The moving grid was used so as to allow for the simulation of the movement of flexible membrane covering regions of the wing, although only the rigid case will be discussed here. Figure 1-2 is a graphic showing the grid and model used by the solver. Figure 1-3 depicts the circulation effects observed over the wing at an angle of attack of 6° and 10° and a free-stream velocity of 10 m/s. The CFD results showed that at low angles of attack, the flow on the bottom side of the wing re-circulates. It also appeared that a region of recirculation, reminiscent of a long separation bubble was present on the top side of the wing extending from the mid-chord to an attachment point not quite all the way to the trailing edge (TE). The pressure distribution over the surface of the wing is also presented in Figure 1-3, and shows that the wing tip vortices cause extra lift due to the low pressure they apply at the wing tips. Experiments were tailored to address issues raised by previous UF MAV research such as separation type and location, and the nature of the wing tip vortices. The difference in flow properties between a rigid and perimeter reinforced (PR) wing were also investigated by Sytsma (2006) in an attempt to explain the different loading properties of each.

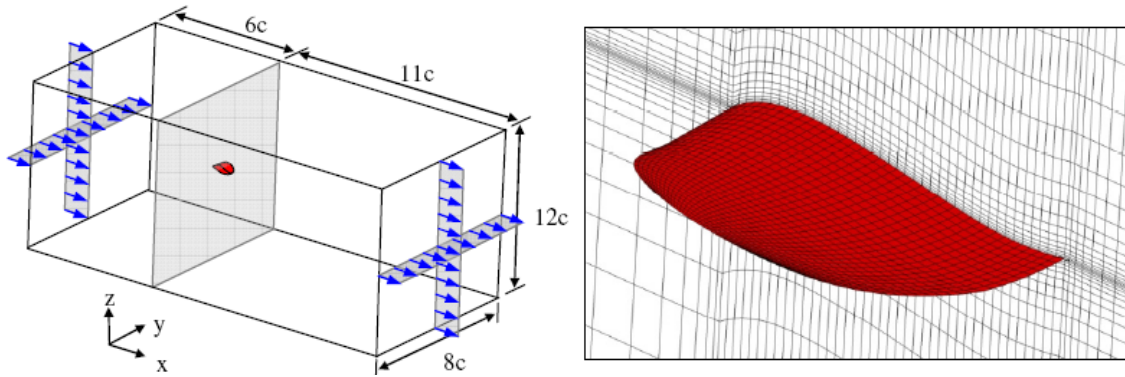


Figure 1-2. The CFD computational domain and details of the mesh near the wing surface (Stanford, 2007).

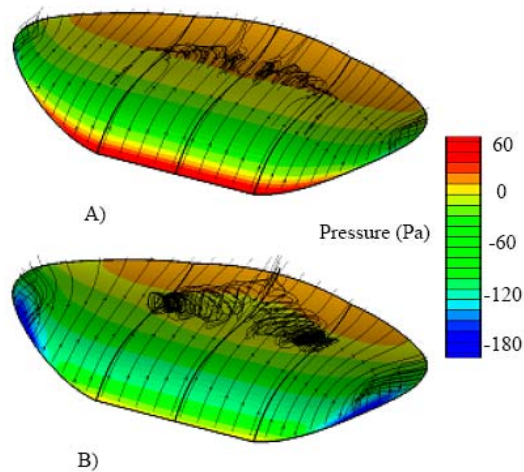


Figure 1-3. CFD streamlines and pressure distribution at a free-stream velocity of 10 m/s and A) $\alpha = 6^\circ$ & B) $\alpha = 10^\circ$, (Stanford, 2006).

Over the past several years, a series of wind tunnel tests were performed at UF in order to validate a static aeroelastic model for low Reynolds number, low aspect ratio membrane micro air vehicle wings with adaptively inflating camber (Sytsma, 2006). A visual image correlation system, in conjunction with a standard strain gage sting balance, were used to measure the wing loads, displacements, and strains for a range of pre- and post-stall angles of attack. Modeling

efforts included coupling a membrane finite element with geometric nonlinearities to a laminar Navier-Stokes solver. A comparison of experimental and numerical deformed membrane profiles indicates poor predictive capabilities of the steady aeroelastic solver at low angles of attack: massive separation under the wing leads to unsteady flow phenomena. A comparison of numerical and experimental (via laser flow visualization) flow structures shows discrepancies in the flow separation/reattachment behavior, most likely a result of laminar-turbulent transition that occurs above a separation bubble at low Reynolds numbers (Stanford, 2007).

Good correlation in wing displacements and strains are attainable at moderate angles of attack (where the flow is steady), and even at post-stall angles (where the flow is not). The Navier-Stokes solver is able to calculate the longitudinal aerodynamics over rigid MAV wings within experimental error for the entire sweep. The aeroelastic solver correctly indicates the trends in aerodynamic performance with adaptive camber adjustment (increased lift, lift slope, and drag), though the magnitude of the shift is generally under-predicted. Turbulence effects, unsteady flow, and membrane wrinkling are all identified as candidates for upgrading the model fidelity. An examination of the computed pressure distributions identifies several key aeroelastic effects: decreased tip vortex strength, pressure spikes and flow deceleration at the tangent discontinuity of the inflated membrane boundary, and an adaptive shift of high pressure (on the bottom surface) and low pressure (on the top surface) regions towards the trailing edge, thereby increasing the nose-down pitching moment and the static margin.

Streamlines at the root of a rigid MAV wing can be seen in Figure 1-4, for three angles of attack (0° , 15° , and 30°). Both numerical data (computed using the CFD algorithm detailed above) and experimental data (laser-based flow visualization) are given. A Model 95 Lexel continuous argon-ion 4.0 W laser is directed through a 1000 mm biconvex lens and a 25.4 mm

semi-cylindrical lens to create a laser sheet. This sheet is then directed into the test section, oriented parallel to both the incoming flow and the gravity vector and focused on the root of the wing. This experimental setup affords flow visualization at other spanwise locations, but the strong cross-flow elsewhere over the MAV wing limits the usefulness of this two-dimensional technique.

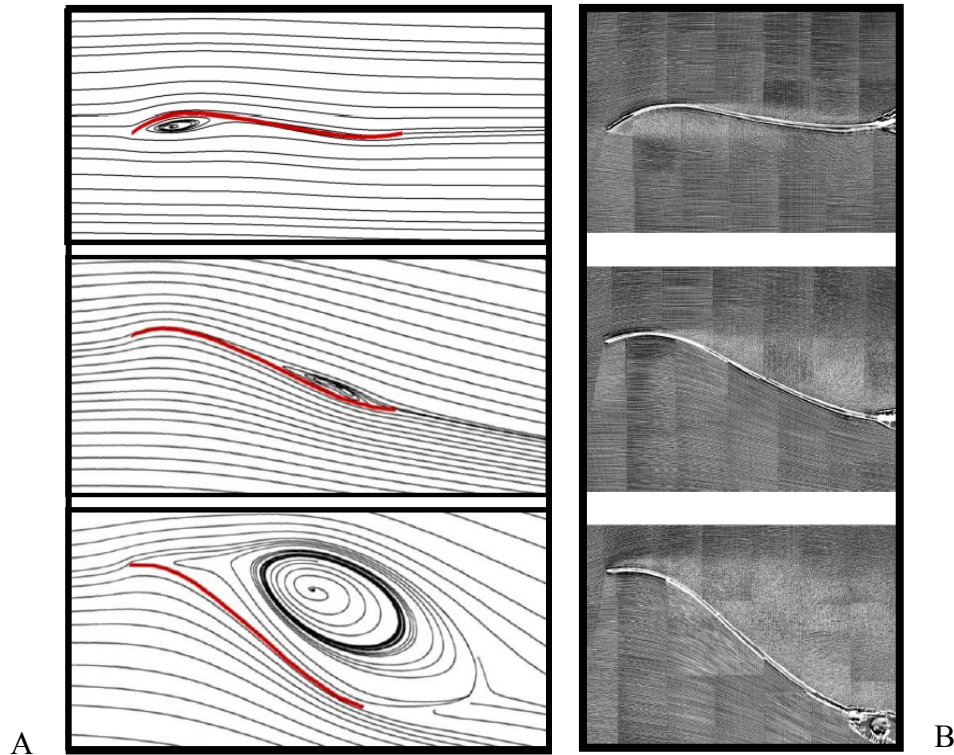


Figure 1-4. Flow structure at the root of a rigid UF MAV wing for 10 m/s and $\alpha = 0^\circ, 15^\circ$ & 30° . A) Numerical results, B) Experimental flow visualization, (Stanford, 2007).

While the Reynolds number, planform shape, and airfoil are identical for the computational wing and the wind tunnel model seen in Figure 1-4, the latter has no dihedral. The airfoil shape at the root is simply extruded to both wingtips, which provides the camera with an unobstructed view across the span of the wing. However, since the wing being researched here and the one modeled by Stanford and Viieru (2006) includes a 7° dihedral between $2z/b = 0.4$ and the wingtips, the comparison to the data in Figure 1-4 is not completely ideal, since the experimental

flow visualization shown in Figure 1-4 was performed on a simplified representation of the actual airfoil. This was done in order to view the entire flow field close to the center-span of the wing and to avoid excessive blooming from the laser.

Both model and experiment indicate a large separation bubble on the lower surface of the wing, towards the leading edge, at 0° angle of attack. The model's success in predicting both the size and location of this separation bubble perhaps signifies completely laminar flow over the bottom wing surface at this angle. The flow visualization also indicates that the flow separates over the location of maximum camber on the upper wing surface, and reattaches towards the trailing edge. The numerical flow simulation also predicts a separation bubble at this angle, though significantly smaller and entirely confined towards the trailing edge. Similar prediction problems exist at the moderate angle of attack of 15° . While both experimental and numerical data show that the flow on the underside of the wing is completely attached, the predicted zone of separated flow over the upper surface of the wing is again significantly under-predicted. Grid refinement studies have indicated that adding more nodes to the structured mesh seen in Figure 1-2 (from 210,000 to a million) can increase the size of the computed separation bubbles: grid-independent solutions are difficult to obtain at such low Reynolds numbers. The lack of a transition/turbulence model probably also prevents a better correlation between the experimental and the numerical results; the visualization mosaic at $\alpha = 15^\circ$ shows that the flow does not have sufficient room to reattach to the upper wing surface, while the numerical flow does. At $\alpha = 30^\circ$, both numerical and experimental results show completely separated flow over the upper wing surface, starting at the leading edge. It can be assumed that that the data presented in the images would lack the complex effects of the highly three dimensional flow in the region due to the mixing of wing-tip vortices with the layer of separated flow over the wing. It was the aim of this

research to try to identify and attribute certain characteristics in the flow over the wing to the physical properties of the wing itself.

As Stanford and Viieru's work has provided confidence in their aeroelastic model's ability to predict deformed wing shapes, accumulated membrane strains, and aerodynamic forces/moments, attention can now be turned to numerical data that was not earlier verified in the laboratory due to the limited capability of their experimental apparatus.

Outline

In the following study, an effort has been undertaken to investigate the flow around a three dimensional low Reynolds number airfoil, with quantitative flow field data obtained from Particle Image Velocimetry experiments. The airfoil being investigated is rigid in nature and has a slight reflex towards the trailing edge. Previous investigations have used this airfoil as a baseline configuration for studying the effects of passively compliant wings configurations. These studies have included those by Ifju et al. (2005), Stanford et al. (2006), Albertani (2005) and Viieru (2006) which used numerical simulations to predict lift and drag coefficients for this airfoil. Measurements by Sytsma and Albertani showed some discrepancies with the lift and drag predictions from the simulations beyond an angle of attack of 20° . This research will try to shed some light on identifying some of these discrepancies by comparing the flow obtained from these numerical simulations to the experimental data obtained from PIV measurements under identical conditions and different angles of attack.

CHAPTER 2 EXPERIMENTAL DETAILS

In the following chapter there will be a description provided of the various components of the experimental setup. This discussion will include the physical characteristics of the wing model, the wind tunnel facility, the seeding mechanism and the various components of the flow measurement system. The discussion of the wind tunnel facility will include the flow characteristics and potential effects of the physical hardware to introduce seed in to the test section. A brief background on PIV measurements has also been provided, accompanied by a description of the various settings used to obtain the data as well the procedure used to analyze the data thereafter.

Micro Air Vehicle Wing Model

As mentioned above, the discussion in this thesis will be limited to flow measurements on a fully rigid wing configuration, which can be seen in Figure 2-1. This Zimmerman planform is representative of a typical MAV developed at the University of Florida, with the fuselage, propeller, and stabilizers removed (Albertani et al., 2005, Claxton et al., 2006 & Mueller et al., 2007) and has been extensively studied by Albertani (2005), Viieru (2006), Sytsma (2006) and Stanford (2007). Therefore, apart from performing a characterization of the flow around such a low aspect ratio wing, the aim of this research was also to compare the experimental results obtained from PIV, to results obtained from a numerical model utilized by Viieru & Stanford (2006), which was presented in Khambatta et al. (2008). A comparison of the results obtained from previous load testing on the wing at various angles of attack and the numerical model had been performed under identical conditions with some discrepancies being observed around the critical stall angle (Stanford, 2007). Therefore, it was important that the identical airfoil be chosen for the PIV experiments so as to be able to form a basis for comparison of the results.

The wing (Figure 2-1) has a wingspan, $b = 0.152$ m, the root chord, $c = 0.124$ m, resulting in an aspect ratio is 1.25 (defined as the square of the wingspan divided by the total wing area). The remainder of this document will adopt the following coordinate system: x is chord-wise (LE to TE), z is span-wise (center-span to right wing tip), and y is along the vertical direction. Figure 2-1 also displays a side view of the wing where the maximum camber at the root is 6.8% (at $x/c = 0.22$), the maximum reflex at the root is 1.4 % (at $x/c = 0.86$), and 7° of positive geometric twist (dihedral) is built into the wing-tip between $z/b = 0.2$ and the wingtip. The wing in the wind tunnel model shown in Figure 2-1 is constructed from 5 layers of bi-directional plain weave carbon fiber laminate. For the range of flight speeds typically seen by such a vehicle (6 – 10 m/s), the wing is considered to be nominally rigid. For the flow measurements presented in this work, the origin of the coordinate system is located at the center of the leading edge of the wing. The wing was mounted inverted in the wind tunnel (to facilitate an easier PIV setup) and was rotated about a point at approximately $c/2$ through the various angles of attack. For these experiments, the angle of attack of the airfoil was obtained by resting the flat edge of a digital protractor between the leading edge of the wing and the bottom of the reflex of the wing ($\sim x/c = 0.8$). The images in Figure 2-2 show how the wing was mounted in the test section for the PIV experiments.

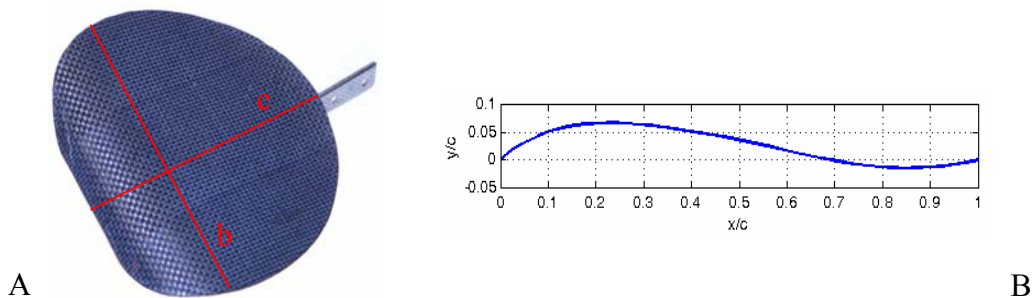


Figure 2-1. The rigid micro air vehicle wing used in this study, A) three dimensional view, B) the centerline profile of the wing normalized by chord length.



Figure 2-2. The wing mounted in the test section for 3-component PIV.

Wind Tunnel Facility

The experiments were conducted in the open jet test section of the low speed, open loop wind tunnel at the University of Florida Research Engineering and Education Facility (UF REEF). The wind tunnel has an overall length of 5.2 m and comprises an inlet with some flow conditioning, a contraction, a test section and a diffuser connected to a blower. A room (see Figure 2-3) with dimensions 2.5m x 2.5m x 2.5m houses the contraction, test section and the beginning stages of the diffuser. The air enters the contraction through a bell mouth and a 0.1 m long flow straightening section that consists of a plastic honeycomb material (0.025 m equivalent diameter, $l/D = 4$) sandwiched in between two layers of fine mesh screen. A settling section 0.15 m in length is located immediately after the honeycomb material and transitions to a 1.22 m long square contraction with an area ratio of 3.87. The inlet to the test section is nominally a 0.775 m square ($W \times H$) and has a length of 0.86 m long (L) before the inlet to diffuser. The wing is mounted in the center of the test section, where the wing tips are approximately $2.4c$ from the edge of the shear layer that develops due to the interaction of the open jet with the air surrounding the test section. The entrance to the diffuser starts as a 0.91 m square cross-section and leads to a circular cross-section with a nominal diameter of 0.76 m and can be seen in Figure 2-4. At the end of the diffuser there is an azimuthal array of adjustable vanes controls the volumetric flow rate through the test section. The vanes sit between the diffuser and a 0.76 m

diameter impeller fan which spins at a constant rate of 1050 rpm. The impeller fan is belt driven by a Baldor 3-phase 5.0 HP electric motor spinning at 1750 rpm. The wind tunnel is capable of providing free-stream velocities between 2.0 m/s and 10.0 m/s depending on the angle of the vanes. Although after much work on vane system it was determined that there is no repeatable way of setting the velocity so all of the measurements here were acquired with it fully open.



Figure 2-3. Photographs of the medium speed wind tunnel facility at UF REEF (above).

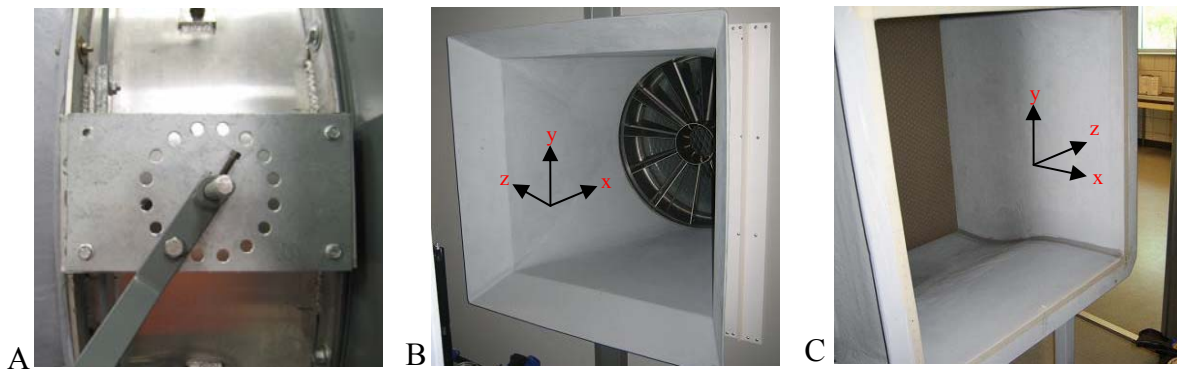


Figure 2-4. Photographs showing the flow control mechanism of the wind tunnel. The lever (A) controls the angle of the vanes sitting in the diffuser (B).

For the purposes of this document, the origin of the coordinate system in the wind tunnel is placed at the center of the entrance to the test section as displayed in the rightmost photograph in Figure 2-4. It was determined that the setup would require the wing to be installed inverted in a region around $x = 0.1L$. Therefore to ensure that it was being placed in a uniform environment horizontal velocity profiles have been presented here for measurements taken in the z-y plane at

$x = 0.1L$ and at $y = H/4, 0$ & $-H/4$. A Heise (Model ST-2H) 0-0.5” H₂O pressure transducer with an accuracy of 0.005% FS (~ 0.1 m/s) was used to collect static and stagnation pressure data from a Pitot Probe. The pressure transducer was sampled at 1.67 Hz and a total of 120 samples were collected at each location. Temperature data was also recorded simultaneously and a reading was also taken for the local pressure in order to calculate the density of the air. Assuming the flow to be incompressible, from the pressure measurements and the density calculations, it was possible to arrive at the flow velocity for the probe location. As can be seen in Figure 2-5, the horizontal velocity profiles from the three different y -locations vary by less than 1.0% of the mean centerline velocity which lies well within the error bounds of the pressure transducer (0.005% FS). Where 0.005% corresponds to approximately 0.1 m/s and full scale (0.5” of H₂O) corresponds to approximately 14.4 m/s.

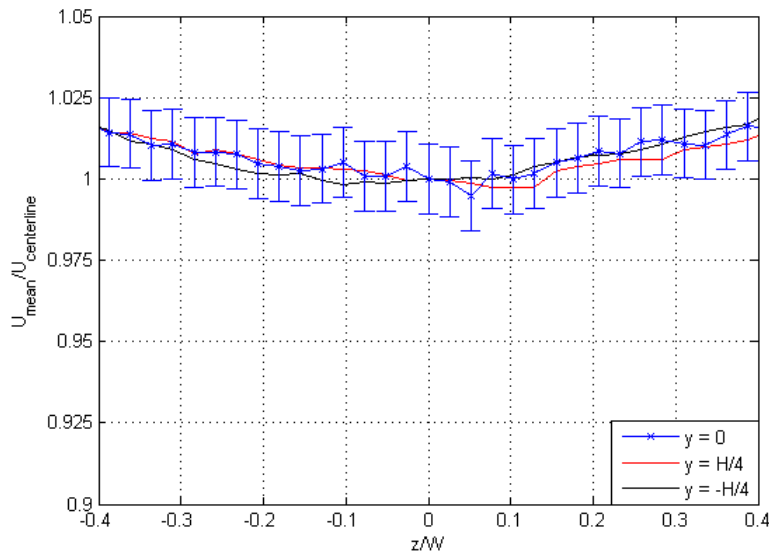


Figure 2-5. Horizontal velocity profiles in the z - y plane at $x = 0.1L$. Velocity normalized by centerline velocity at $x = 0.1L$. Horizontal dimension (z) normalized by the width of the test section (W).

Apart from taking preliminary pitot tube measurements, turbulence levels at the centerline of the test section of the wind tunnel were also measured using a constant temperature anemometer. A Dantec Dynamics (55M10) CTA bridge was used in conjunction with the hot

wire probe which had a sensing element of length 1.0 mm and nominal diameter of 5 microns. Measurements were collected at 2.0 kHz and a total of 50 ensembles of 4096 samples each were recorded. The CTA was first calibrated by simultaneously collecting pressure/velocity data from the Heise pressure transducer at a location near enough to the hot-wire probe so that it can be assumed that the velocity is identical. These voltage and velocity measurements were collected at various wind-tunnel flow velocities after which a 4th order polynomial was fitted to the data in order to compute a calibration equation for the CTA for that run (George et al., 1987). Error bars were computed for the calibration curve of the CTA based on the maximum error between the measured values and the estimated values from the curve. However, these values were well below the error that propagated through the measurements due to the accuracy of the pressure transducer (± 0.1 m/s). Figure 2-6 shows a sample calibration curve plotted alongside the actual data it was derived from. Error bars have been shown on the plot, but are not clearly visible because of their small magnitude (± 0.035 m/s). The centerline turbulence values were thus measured at $x = 0.1L$ and found to be less than 0.5 % of the free-stream velocity at 9.0 m/s.

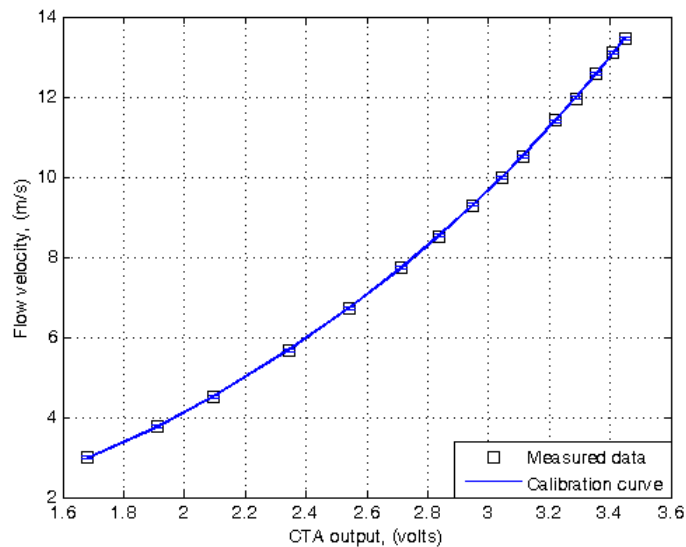


Figure 2-6. A sample CTA calibration curve computed before using the anemometer for experiments. The accuracy of the curve is ± 0.035 m/s (± 0.3 %) around a flow velocity of 9.0 m/s.

Seeding Mechanism

The ability to acquire high quality PIV measurements is limited by the size, density and distribution of the tracer particles being introduced into the flow. A Laskin nozzle high-volume liquid droplet seeding generator from Dantec Dynamics (model 10F03) was used to atomize olive oil and produce seed particles which are expected to be in the size range of 2-5 μm (Dantec Dynamics Manual: High Volume Liquid Droplet Seeding Generator).

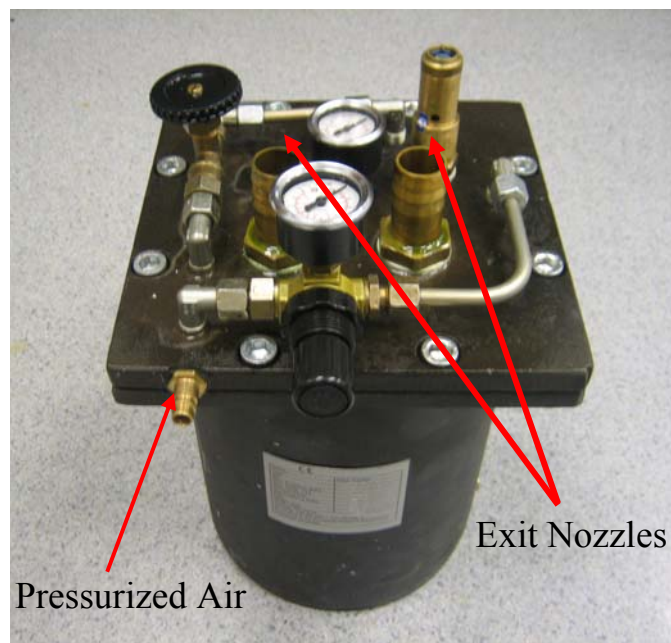


Figure 2-7. The Laskin nozzle, high-volume liquid droplet seeding generator from Dantec Dynamics.

As can be seen from Figure 2-7, the atomized olive oil is forced out through two circular ports (outer diameter of 1.0”) that allow a maximum compressed air flow of 20.9 l/min, when the incoming compressed air supply is pressurized to 2 bar. Using the nozzles by themselves was not enough to adequately seed the flow around the wing during the experiment. A mixing chamber (Figure 2-8) with a rectangular cross-section of 0.9m x 0.7m was built and positioned upstream of the inlet-contraction to the wind tunnel in such a manner so as to allow the seed to

be uniformly distributed in a 0.45m x 0.35m cross-section around the wing. This meant that there was approximately a $1c$ distance between each wing tip and the edge of a turbulent mixing layer that had been induced into the flow by the seeding mechanism upstream of the wind tunnel.



Figure 2-8. The cardboard mixing chamber that was assembled to promote uniform seeding in a 0.45m x 0.35m cross section around the wing.

The mixing chamber also contained two flow straightening sections spaced 0.4 m apart. These sections contain honeycomb material with an L/D ratio of 4. It was clear that this apparatus would cause a loss of pressure in a section of the flow around the wing. Therefore, in an effort to see exactly what effect the seeder was having on the flow in the test section, horizontal velocity and turbulence profiles were developed in the region where the wing was to be mounted. As can be seen in Figure 2-9, there is a pressure loss associated with the region obstructed by the seeder, which results in a 5% slower mean centerline velocity. Though not ideal, the velocity profile appears to be uniform over a region corresponding to the span of the wing, after which it gradually starts to increase. When looking at the fluctuating component of velocity in the same region, locations can be clearly identified, where the effects of the walls of

the seeder can be seen on the flow in the test section, defining a clear boundary where slower moving air from within the seeder meets the faster flow entering the contraction around it.

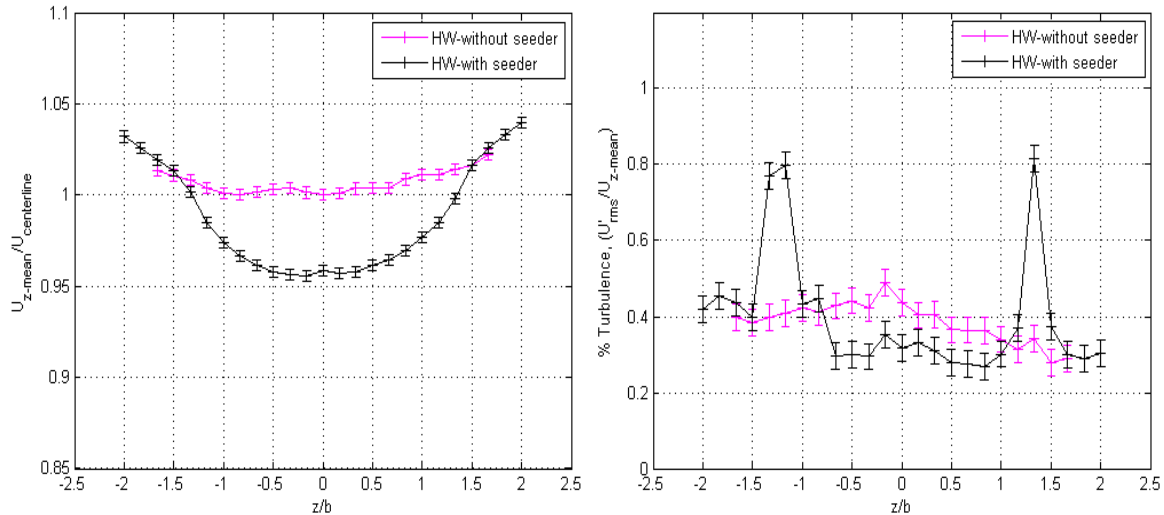


Figure 2-9. Hot-wire, normalized velocity and percentage turbulence profiles. Locations on the z -axis have been normalized by the wing-span, b .

The wing was therefore mounted in the center of that region to try and minimize any effects of the turbulent mixing layers on the characteristics of the wing. From the turbulence profile one can estimate that there is a distance greater than $0.5b$ between the wing-tips and the edge of the mixing layer, hence it is assumed that the flow over the wing will not be affected. It can also be noted that there is a clear reduction in the turbulence levels ($\sim 0.1\%$) in the region of the flow coming through the seeder when compared to the flow in the wind tunnel without it. This is most likely due to the presence of the two additional flow straightening sections that are embedded within the seeding mechanism.

Turbulence spectra was also calculated at the centerline of the test section ($x = 0.1L$, $y = 0$, $z = 0$) for flow conditions with and without the seeder. Based upon the previous measurements presented, the turbulent energy at the centerline is less with the seeder upstream of the inlet than without (from Figure 2-9). This is verified by looking at the turbulence energy spectra show in

Figure 2-10A for both cases at $z = 0$, ($\text{rms } U'_{\text{w/ seeder}} = 0.027 \text{ m/s}$, $\text{rms } U'_{\text{no seeder}} = 0.038 \text{ m/s}$). Comparisons have also been drawn for the turbulence energy spectra at the centerline and the turbulent mixing layers (approximately $2.6b$ apart) around $z = -1.3b$ and $z = 1.3b$. A clear relation can therefore be drawn between the higher turbulence levels shown in Figure 2-9 at $z = -1.3b$ & $z = 1.3b$ and the corresponding increased turbulence energy levels shown in Figure 2-10C; indicating high levels of velocity fluctuations in those regions, a possible effect of the seeding mechanism. Figure 2-10B also shows that the turbulence energy levels between $z = -1.3b$ & $1.3b$ are very similar, and negate the presence of any mixing layer in the flow at that location, thus clarifying that the increased turbulence levels at $z = -1.3b$ & $1.3b$ are due to the seeding mechanism.

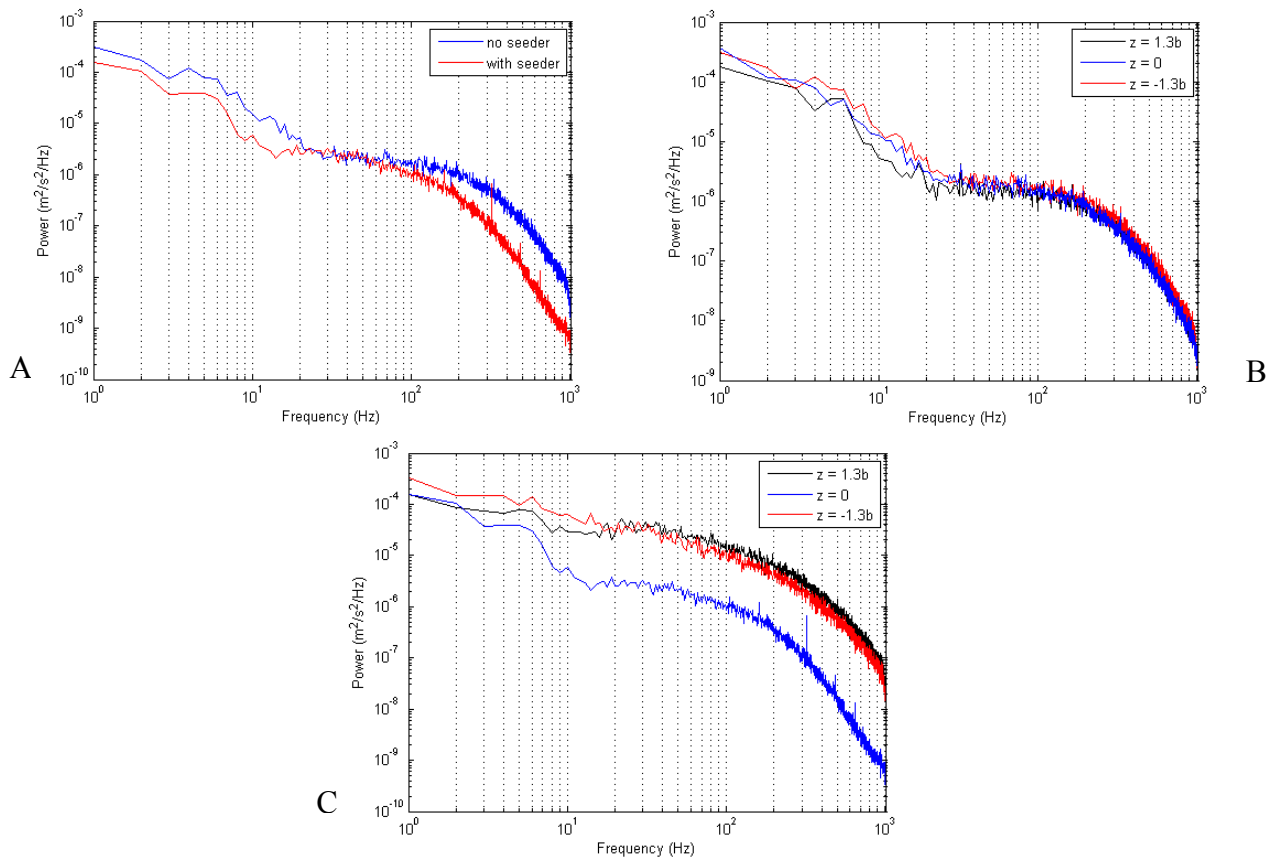


Figure 2-10. Comparison of the turbulence energy spectra at $x = 0.1L$; A) at $z = 0$, with and without seeder upstream of inlet, B) with no seeder, C) with the seeder.

Particle Image Velocimetry (PIV) Flow Measurements

The flow experiments to measure planes of the velocity field over the wing were performed using two different camera configurations with respect to the wing. The first configuration comprised a single camera perpendicular to the laser light sheet illuminated in the x-y plane and traversed to various span-wise locations, z, (2-component PIV). The second configuration used two cameras in a stereoscopic configuration (3-component PIV) with a laser light sheet oriented in the z-y plane and traversed to various chord-wise locations (Figure 2-11). Illustrations of these two configurations are presented in Figure 2-12A & B respectively, including a definition of the coordinate system to be used for subsequent discussion.

Free-stream conditions were verified before the experiment by means of a pitot-static probe connected to a Heise (ST-2H) 0-0.5" of H₂O, pressure transducer with an accuracy of 0.005% FS (~0.1 m/s). The time scale to ensure the capture of statistically independent snapshots of the flow field from the PIV system was calculated to be ~0.028 s, assuming that the largest conceivable scale being on the order of the wing-chord. This implies that the sampling frequency of the PIV system should be less than 35.5 Hz, to ensure statistically independent samples.

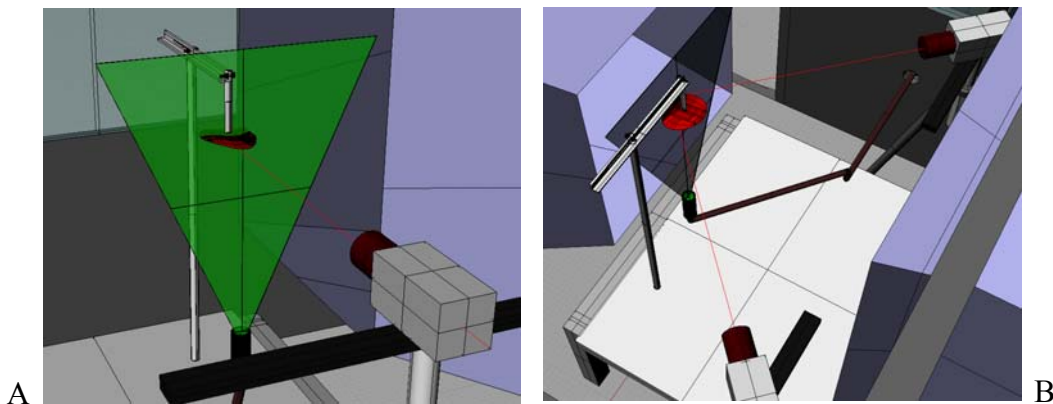


Figure 2-11. Schematics of the PIV setups inside the test section of the wind tunnel. A) 2-component PIV and B) 3-component PIV.

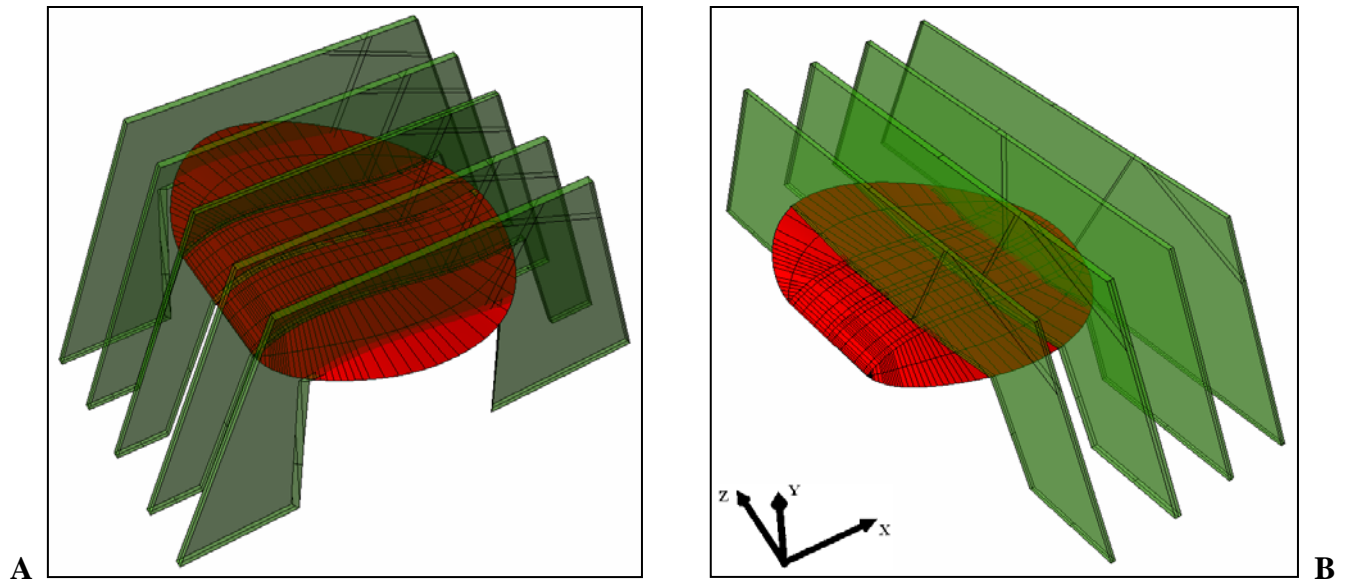


Figure 2-12. Images showing planes illuminated by the laser for PIV, A) span-wise slices in the x-y plane and, B) chord-wise slices in the y-z plane.

The instantaneous measurements of the velocity field were acquired using a Dantec Dynamics TR PIV system. The components of the PIV system include a Lee Laser Series 800-PIV/40G Nd:YAG laser system, light sheet optics including a light arm, two IDT XS-5 high speed digital cameras with 2 GB onboard memory, f-2.8 Nikkor lenses and version 4.71 of Dantec's Flow Manager software. The cameras have pixel dimensions of $12\mu\text{m}$ square and a resolution of 1260×1024 . For the 2-component PIV setup, the camera lens used had a focal length of 60 mm and the magnification was set at $M = 0.11$ at a distance of 0.625 m from the plane of illumination. For the 3-component PIV setup, the camera lens used had a focal length of 105 mm and the average lens magnification was $M = 0.09$ at a distance of 0.93 m. The light sheet optics were adjusted for the 2-component setup so that the laser sheet thickness was ~ 2 mm. For the 3-component PIV setup, the laser sheet thickness is increased to approximately twice the size of the interrogation area projected out into object space (Dantec Manual on 3D Stereo PIV, 2005). The thickness of the laser sheet should be enough so that the high speed

cameras can adequately capture the out-of-plane velocity component of the flow (in this case, the axial velocity in the wind tunnel, u). Through some preliminary tests, it had been determined that the best results were obtained when a final interrogation area of 32 x 32 pixels was applied to the images. This setting resulted in the least number of erroneous and estimated vectors per image frame when compared to the results obtained with using the minimum possible interrogation area of 16 x 16 pixels. Therefore, with an interrogation area of 32x32 pixels, a camera pixel pitch of 12 μm (each pixel is 12 μm square), and a magnification factor of $M = 0.09$, the approximate light sheet thickness is calculated using the formula;

$$2 \frac{(L_{IA} P_P)}{M}, \quad (2-1)$$

where L_{IA} is the length dimension of the interrogation area in pixels and P_P is the pixel pitch on the CCD array in meters. The resultant laser sheet thickness was thus calculated to be ~6 mm.

As previously mentioned, the seeding particles are introduced into the flow just upstream of the inlet-contraction to the wind tunnel in such a manner that they produced a region of uniformly seeded flow all around the wing within the test section. Given the magnification of the lenses, an $f\# = 2.8$, and the wavelength of the laser, $\lambda_L = 532 \text{ nm}$, one can calculate the diffraction limited spot size, d_{sp} for a single lens (Meinhart & Wereley, 2003) using the following relationship,

$$d_{s_p} = 2.44(M + 1)\lambda_L f\#. \quad (2-2)$$

The particle image diameter, d_r on the pixel array is then calculated using equation (2-2), where d_p is the diameter of the seeding particles (Westerweel, 2000):

$$d_r \cong (M^2 d_p^2 + d_{s_p}^2)^{\frac{1}{2}}. \quad (2-3)$$

For these calculations, d_p was assumed to be 5.0 microns, based on specifications provided by Dantec. Based on equations (2-1) & (2-2), d_{sp} & d_r were calculated to be 4 microns for both PIV setups. For cases where $M \ll 1$, $d_r \rightarrow d_{sp}$ (Westerweel, 2000), therefore the average ratio of particle image diameter to pixel dimension was 0.33. Ideally this ratio should be greater than 1.0 to avoid any ‘pixel locking’ effects between successive image frames, but the limitations of the setup prevented the cameras from being installed any closer to the wing and the effects will be discussed below.

Before collecting data in either of the setups, a flat 200 mm square calibration target (with black dots on it, spaced 5 mm apart) was lined up with its face in the plane of the laser sheet. The camera was then focused on the face of the target so as to make sure that the particles passing through the illuminated region would be photographed clearly. For the 2-component PIV setup, great care was taken to make sure that the face of the target was perpendicular to the CCD array of the camera in order to minimize the propagation of errors induced by an incorrect alignment of the camera with the flow.

For the 3-component PIV setup, the cameras were aligned at a 42° angle to the target and focused such that their focal planes rested directly on the center of the target. As can be imagined, the left and right regions of the target were severely out of focus. As a result, a Scheimpflug mount was used to offset the angle between the CCD array and the complex lens by 9° (Scheimpflug, 1904) to bring the entire region of interest into focus. The calibration target was then traversed to several known locations in the stream-wise direction and photographed each time. With this series of photographs and known locations, the Flow Manager software was then able to perform a calibration of both cameras and develop a grid for calculations that encompassed the common region between the fields of view of the two cameras. It should be

noted that the three dimensional displacement field is computed using a model that describes how displacements in 3D are mapped onto 2D planes (the cameras in this case). Thus, by performing an image correlation on the data from each camera, the resultant 2-component vector maps can be used to build one data-set that contains all three components of the velocity for the overlapping regions of the flow captured by both cameras.

For flow that is perpendicular to the camera, a trace particle should ideally travel a maximum distance of $0.25L_{IA}$ between successive images to ensure a reasonable signal to noise ratio (Dantec FlowManager Manual, 2005), i.e. ~ 4 pixels for an interrogation area of 16×16 pixels or ~ 8 pixels for an interrogation area of 32×32 pixels. Based on this estimate and the knowing the flow velocity, one can compute dT , the time delay between successive images. For 2-component PIV, the size of the image window was 0.14×0.114 m and to be able to apply a final interrogation area of 16×16 pixels to an image pair, the time delay (dT) between successive images in a pair was set at $38 \mu s$. For 3-component PIV, the sizes of the image windows were 0.1×0.08 m and a final interrogation area of 32×32 pixels was applied to the data.

To obtain statistically independent data, the frame rate was set at 35.0 Hz. A sample of the convergence is taken from the measurements at a point in the region of separated flow over the wing at $\alpha = 25^\circ$ and is shown in Figure 2-13; the data has been averaged over n samples, then normalized by the mean of the total number of samples (\bar{N} , where $N = 810$). It can be seen that once the sample size exceeded 750, the variations in the mean velocity were less than 0.5% of the mean, indicating that an adequate number of samples had been collected. It should be noted that the location chosen to evaluate the convergence of the mean was one with large fluctuating

velocities (within the region of separated and re-circulating flow), so in some sense it should represent a worst case scenario.

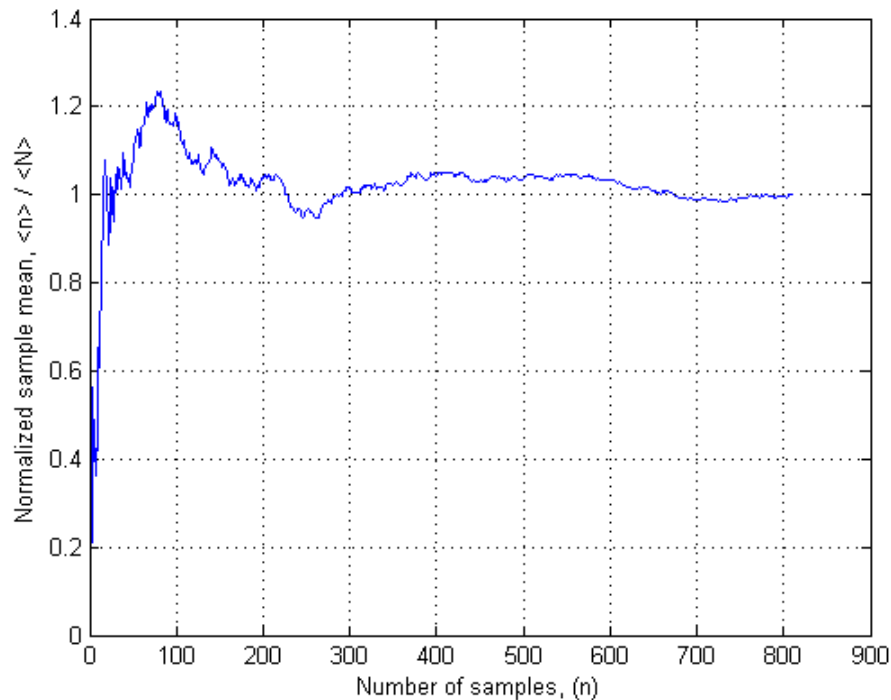


Figure 2-13. A convergence plot of normalized mean vs. sample size in the region of separated flow over the wing at $\alpha = 25^\circ$.

After the raw images had been obtained, cross-correlations were performed on the data using an iterative technique called adaptive correlation in the Flow Manager software. This algorithm starts from an initial guessed offset value (based on dT), an offset is introduced from the first window (the interrogation area in the image frame from laser pulse one) to the second window. The obtained vector is validated and is used as a new estimate for the window offset. A new run is made, but this time with a smaller interrogation area. The main benefit derived from using the shifted window is capturing the particle images that left the interrogation area during the time between the two light pulses, causing what is known as ‘in-plane dropout’ or ‘loss of signal’. This in turn, increases the number of successful vectors that can be obtained from that region. Therefore, adaptive correlation helps to boost the signal strength due to the capture of

the particles originally lost due to in-plane dropout and also allows for a possible refinement of the original interrogation area by applying an adaptive window offset that would allow the capture of the best signal. For the purposes of these experiments, the data was processed with a final interrogation area set at 32 x 32 pixels. Two adaptive correlation runs were performed beforehand, with interrogation areas of 128 x 128 pixels and 64 x 64 pixels respectively.

An overlap of 50% was also used on the data, which effectively reduced the grid spacing down to 0.83 mm square for 2-component PIV and to 1.9 x 1.3 mm for 3-component PIV. The correlation within an interrogation area contains peaks that represent a good signal and also contain noise from ‘ghost’ particles (trace particles that entered the interrogation area in the second frame) and any ‘in-plane dropout’. Thus applying a Gaussian filter to the results greatly improved the signal to noise ratio. The width of the window used was 0.1. A low-pass filter was also applied to the data after correlation in order to improve sub-pixel interpolation. This interpolation scheme is based on peak values in the correlation plane along with correlation values for the neighboring points. As mentioned earlier, the ratio of the particle size to pixel size was ~ 0.3 . Therefore, using a low-pass filter increased the number of validated results over the span of the vector map. For instance, Figure 2-14 shows the distribution of estimated vectors for different span-wise locations at $\alpha = 10^\circ$. The quality of the data in the flow over the wing appears to be good, as less than 10% of the vectors have been estimated in that region.

However, the majority of the vector maps resulting from the 2-component PIV experiments show a large number of estimated vectors near the outer regions of the image frame, this is the effect of poor correlation between image pairs due to the presence of ‘ghost’ particles, particles that came into the second frame but were not present in the first. This is also observed in regions where the flow is highly three-dimensional (such as at the wing tips or in the wake of

the airfoil, as in Figure 2-14), where there might be loss of signal or in-plane dropout. In such a case, depending on the filters used, the resulting vectors in such locations are ‘estimated’ based on the behavior of their neighbors. Another reason for a large number of estimated vectors close to the wing tip is due to intense ‘blooming’, which essentially prevents any particles from being tracked in that region due to a ‘white-out’ type effect.

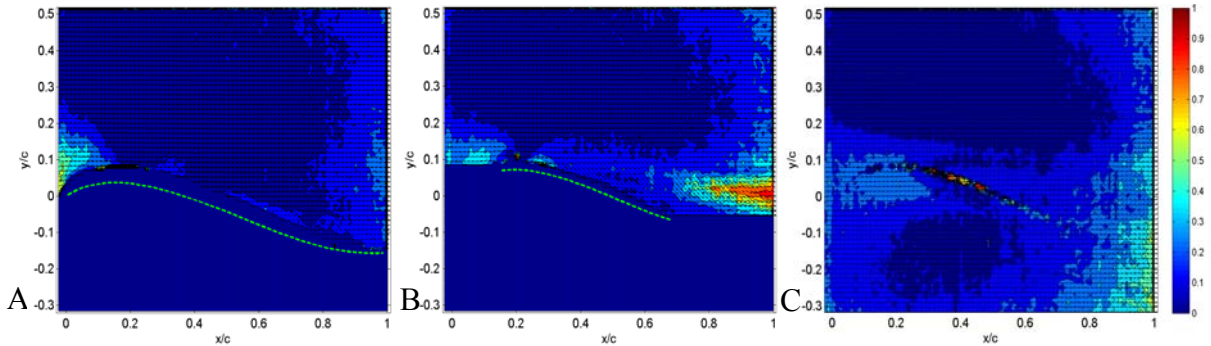


Figure 2-14. Distribution of estimated vectors in the flow field at A) $z/b = 0$, B) 0.46 and C) 0.54. The number of estimated vectors has been normalized by the total number of ensembles.

While some of these vectors might be erroneous, not all of them should be discounted because they might be the after-effects of phenomenon taking place at the leading edge of the wing or very close to this wing surface, that are not being observed. For instance, the view of the flow over wing in the 2-component PIV setup was partially obstructed by the dihedral of the wing; therefore, the presence of a separation bubble or the onset of separation of flow over the wing could not be captured. In such a case, the flow going around the bubble may be the only source of information available, in order to try and identify the possible locations of such a structure.

A series of high speed measurements were also acquired at 400 Hz in an effort to resolve the temporal behavior of the more energetic features of the flow. While the system is capable of sampling at up to 512 Hz in double-frame mode, measurements collected above 400 Hz appeared to suffer from inadequate optical conditions. These high speed measurements were collected

under limited conditions: at $\alpha = 25^\circ$ & 30° in the x - y plane at $b/z = 0$ & 0.5 (2-component PIV); at $\alpha = 30^\circ$ in the z - y plane at $x/c = 0.5, 0.87$ & 1.1 (3-component PIV).

All measurements (2-component, 3-component configurations, statistically independent and high speed), comprised 810 samples. These measurement locations described should provide a sufficient description of the flow topology surrounding this MAV wing to be compared with numerical simulations, and provide some insight into the non-linear lifting characteristics of low Reynolds number airfoils, in particular, the vortices near the wing tips and the regions of separated flow on top of the wing. Figure 2-15 and Tables 1 & 2 represent the locations where PIV measurements were taken around the wing.

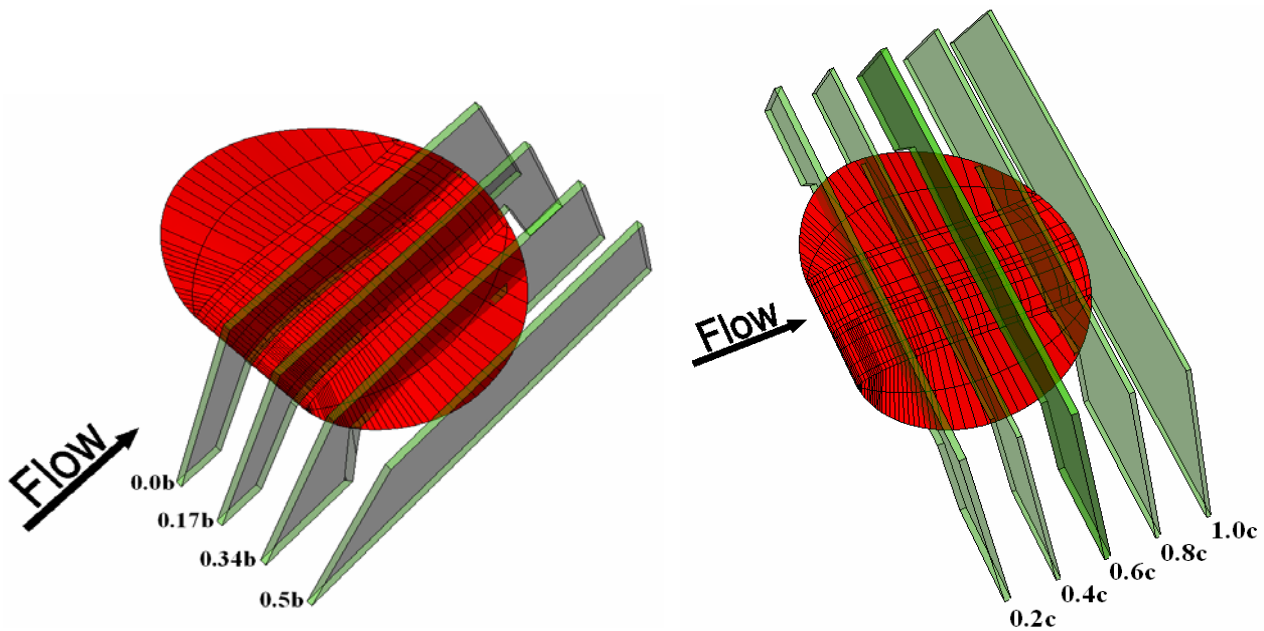


Figure 2-15. Some of the measurement locations for 2-component and 3-component PIV over the wing.

Angles of attack	0°	10°	15°	18°	20°	21°	25°	30°			
Span-wise locations, $2z/b$ (2-component PIV, x - y plane)	0	0.167	0.25	0.33	0.5	0.67	0.75	0.83	0.92	1.0	1.08

Table 2-1. Two-component PIV measurements: Angles of attack and span-wise locations.

Angles of attack	15°	18°	21°	25°	30°						
Chord-wise locations, x/c (3-component PIV, $y-z$ plane)	0.3	0.4	0.5	0.6	0.7	0.8	0.9	1.0	1.1	1.2	1.4

Table 2-2. Stereoscopic PIV measurements: Angles of attack and chord-wise locations.

Errors in the Particle Image Velocimetry (PIV) Measurements

From a classical point of view, the smallest possible displacement that could be resolved from an optical perspective would be on the order of the size of the image of the trace particle on the CCD array. Given that the ratio of the particle image diameter to pixel size for these experiments was approximately 0.3, and since it is not possible to tell which portion of a pixel is excited by the light from a trace particle (the entire pixel detects light), there is a reduced accuracy in the measurements. This would be a problem in specific cases where the particle image would fall directly onto one pixel on the CCD array and nowhere else. For this and a few more reasons, the ideal ratio of particle image diameter to pixel size is approximately 2 (Westerweel, 1997).

For the 2-component PIV setup, this meant that the accuracy of the results was potentially ± 1 pixel, which corresponds to ± 2.9 m/s. This velocity corresponds to a particle displacement of 111.11 μm between two successive image frames, where 111.11 μm is the distance projected onto one pixel (12 μm square) with a lens magnification factor of 0.11.

The Dantec Dynamics FlowManager software uses FFT (Fast Fourier Transform) processing to determine image displacements in PIV. There end up being a discrete number of points representing the correlation plane, with the spacing between the pixels on the CCD array acting as the spacing between the discrete values of the FFT function. Therefore, it is possible to fit a continuous curve to the discrete values of the FFT function and then interpolate on the curve

to allow for sub-pixel resolution. The current version of the PIV analysis software allows for a sub-pixel resolution of $1/64^{\text{th}}$ of the pixel pitch, ~ 187 nm (Dantec FlowManager Manual). But for effective sub-pixel interpolation, the dimensions of the images of the trace particles must be greater than 1 pixel pitch (distance between the centers of two adjacent pixels). If this minimum requirement is not met, then by the Nyquist criterion, the image map would be under sampled and there would be an uncertainty of ± 1 pixel pitch in the recorded location of the trace particle, ± 2.9 m/s (Dantec FlowManager Manual).

However, there is also another school of thought that states that on the correlation plane, the auto-correlation of the particle sensing pixel determines the width of the peak on the correlation plane. Thus, even for a pixel that has completely captured a particle-image, the discrete correlation peak will always cover more than one pixel in the correlation domain (Westerweel, 1997). This approach, coupled with the fact that many particles in the flow would excite more than one pixel on the CCD array, would lead us to believe that the software was able to perform successful sub-pixel interpolations in most cases. Even if $d_p / P_p < 1$, higher seeding density could further improve the quality of the results by increasing the information content of the correlation peaks, i.e. improve the ‘reliability’ of the results by way of a larger number of particle-image pairs having the same displacement.

It has also been observed that for cases where the ratio of particle image diameter to pixel pitch is much less than 1, the measurement error is dominated by bias errors, i.e. pixel locking effects (where the particle-image size does not occupy more than one pixel), and that when this ratio is much greater than 1, the measurements are more prone to random errors. In fact, it has been shown that the estimation error is at a minimum when $d_p / P_p \sim 2$ (Westerweel, 1997).

Even if the image of the particle was projected entirely over two pixels, a curve joining the peaks in the correlation plane (at those two pixels) could be interpolated to determine the center of the image of the particle, however, the presence of noise in the correlation plane would bias the interpolated location of the particle towards one peak or the other (toward the location of either pixel). Therefore, sub-pixel interpolation does not end up being optimal if the particle image diameter is less than twice the pixel pitch of the CCD array (Dantec FlowManager Manual).

Through a process of slight defocusing of the camera (to increase the footprint of the particle-image), increasing the laser light intensity and by concentrating the seeding particles in a tight region around the wing model, a large number of successful correlations and valid vectors were obtained over each vector map. A typical value for the minimum measurement error is ~1% for a particle displacement that is approximately one quarter of the interrogation area (± 0.1 m/s in the case of these experiments). Furthermore, the precision of the measurements is determined using the relation, d_p / D_I , where d_p is the particle image diameter (4 microns) and D_I is the size of one dimension of the interrogation area (16 pixels for the 2-component PIV results and 32 pixels for 3-component PIV). The resulting precision error of the measurements is therefore 0.25 microns/pixel for the 2-component PIV results (2.08 % error) and 0.125 microns/pixel for the 3-component PIV results, 1.04 % error (Westerweel, 1997). In addition, the reliability of the measurements is a direct factor of the seeding density, and a minimum of 5 particle-image pairs is recommended for reliable cross-correlation results (Dantec FlowManager Manual). The seeding density was observed to be >10 particle-pairs per interrogation area for the majority of the cases in the 2 & 3-component PIV setups, with relatively poorer seeding around the edges of the frames in some cases.

CHAPTER 3
PARTICLE IMAGE VELOCIMETRY RESULTS AND DISCUSSION

The following chapter presents the results obtained from the PIV experiments performed on the flow over the model of a rigid MAV wing. As discussed in the previous section, experiments were performed over the wing at various angles of attack and at a free-stream velocity of approximately 9.0 m/s, corresponding to a Reynolds number of 73,000 based on a wing chord length of 0.124 m.

The discussion on the data will be based on the mean flow over the wing, the fluctuating velocities in the three components (u'_{rms}/\bar{U}_∞ , v'_{rms}/\bar{U}_∞ & w'_{rms}/\bar{U}_∞ , where $u = \bar{u} + u'$, $v = \bar{v} + v'$ and $w = \bar{w} + w'$), turbulence shear stress normalized by the square of the free-stream velocity ($\overline{u'v'}/\bar{U}_\infty^2$), and the span-wise and stream-wise vorticity normal to the plane of measurement,

$$\omega_z = \frac{\partial v}{\partial x} - \frac{\partial u}{\partial y} \quad \text{and} \quad \omega_u = \frac{\partial w}{\partial y} - \frac{\partial v}{\partial x} \quad (3-1) \ \& \ (3-2)$$

In an effort to try and identify the evolution of the dominant length scales, spatial cross correlations were also performed on the normal and stream-wise components of the velocity field by selecting an origin and cross correlating the rest of the flow field with respect to it according to the relations,

$$R_{ij}(\delta_x, \delta_y) = E[u'_i(\bar{x}, \bar{y}) \cdot u'_j(\bar{x} + \delta_x, \bar{y} + \delta_y)], \quad (3-3)$$

where E is the expected value of the function and δ_x is the horizontal separation and δ_y is the vertical separation between the measurement locations. The correlation coefficient, ρ_{ij} , was then calculated using equation 3-4;

$$\rho_{ij}(\delta_x, \delta_y) = \frac{R_{ij}(\delta_x, \delta_y)}{\mu(u'_i)\mu_{u'}(u'_j)}, \quad (3-4)$$

where $-1 \leq \rho \leq +1$. In some of the figures in the following sections, the correlation coefficient has been plotted, with values ranging between +1 and -1, where a value of $\rho = -1$ still means that the data is well correlated, but just 180° out of phase.

Due to the dihedral in the wing and because the camera in the 2-component PIV setup was perpendicular to the x - y plane, the flow adjacent to the wing surface could not be characterized in certain regions, (as is indicated by a space between the wing profile and the data). This was due to the combination of the laser “blooming” on the wing surface in addition to obstructed view, see Figure 3-1 below. These regions do not exceed $0.04c$ in height above the wing surface and will be clearly visible in the figures presented through out this section.

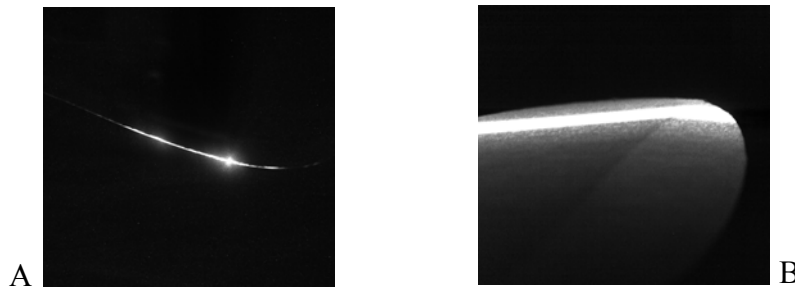


Figure 3-1. Examples of ‘bloom’ in the raw data, at A) the wing-tip, $z/b = 0.5$ and B) near the TE of the wing, $x/c = 0.9$.

In all of the figures in the following sections, the wing surface is clearly outlined (represented by a dotted line), and velocity vectors have been superimposed on top of contour graphs; of the mean velocity fields (stream-wise and normal to the flow), fluctuation levels in the mean velocity fields, turbulence shear stress, spatial cross correlation values and the out-of-plane vorticity.

Mean Velocity Field

Looking at the ensemble-averaged mean velocity data over all the angles of attack in Figure 3-2 and Figure 3-3, as expected, there is clear indication of an acceleration of the flow over the wing at the point of greatest camber ($\bar{u} \sim 1.25\bar{U}_\infty$ & $\bar{v} \sim 0.6\bar{U}_\infty$). The favorable pressure gradient over the positively cambered portion of the wing increases with an increase in the angle of attack, thus leading to an increase in the velocities over the leading edge of the wing. An increase in the angle of attack also leads to an increase in the magnitude of the downward velocities over the top of the wing. The region that contains this strong downward flow ($\bar{v} \sim -0.6\bar{U}_\infty$), grows in size with an increase in the angle of attack of the airfoil.

In the figures showing the distribution of the stream-wise component of the flow at $z/b = 0$, a shear layer with strong gradients in y , is seen above the reflexed portion of the airfoil. This layer appears to grow in thickness between $10^\circ \leq \alpha \leq 15^\circ$, after which it seems to shrink at $\alpha = 18^\circ$ and then increases in thickness again between $20^\circ \leq \alpha \leq 21^\circ$. In the flow above the wing at $\alpha = 25^\circ$ and 30° , the shear layer has clearly separated from the surface of the wing and sits between the free-stream and a region of re-circulating flow. It should be noted that the flow is most likely separated at the lower angles of attack but due to the inability to get near wall measurements the reverse flow vectors could not be seen. While the stream-wise component of the velocity maintains almost similar levels over the span of the wing, the normal component grows stronger in magnitude as $z/b \rightarrow 0.5$ (as much as $\bar{v} \sim -0.75\bar{U}_\infty$ at $z/b = 0.46$). However, for $z/b \leq 0.17$, the normal component of the velocity appears to be mostly affected by the downwash effect over the airfoil due to its angle of attack ($\bar{v} < 0$).

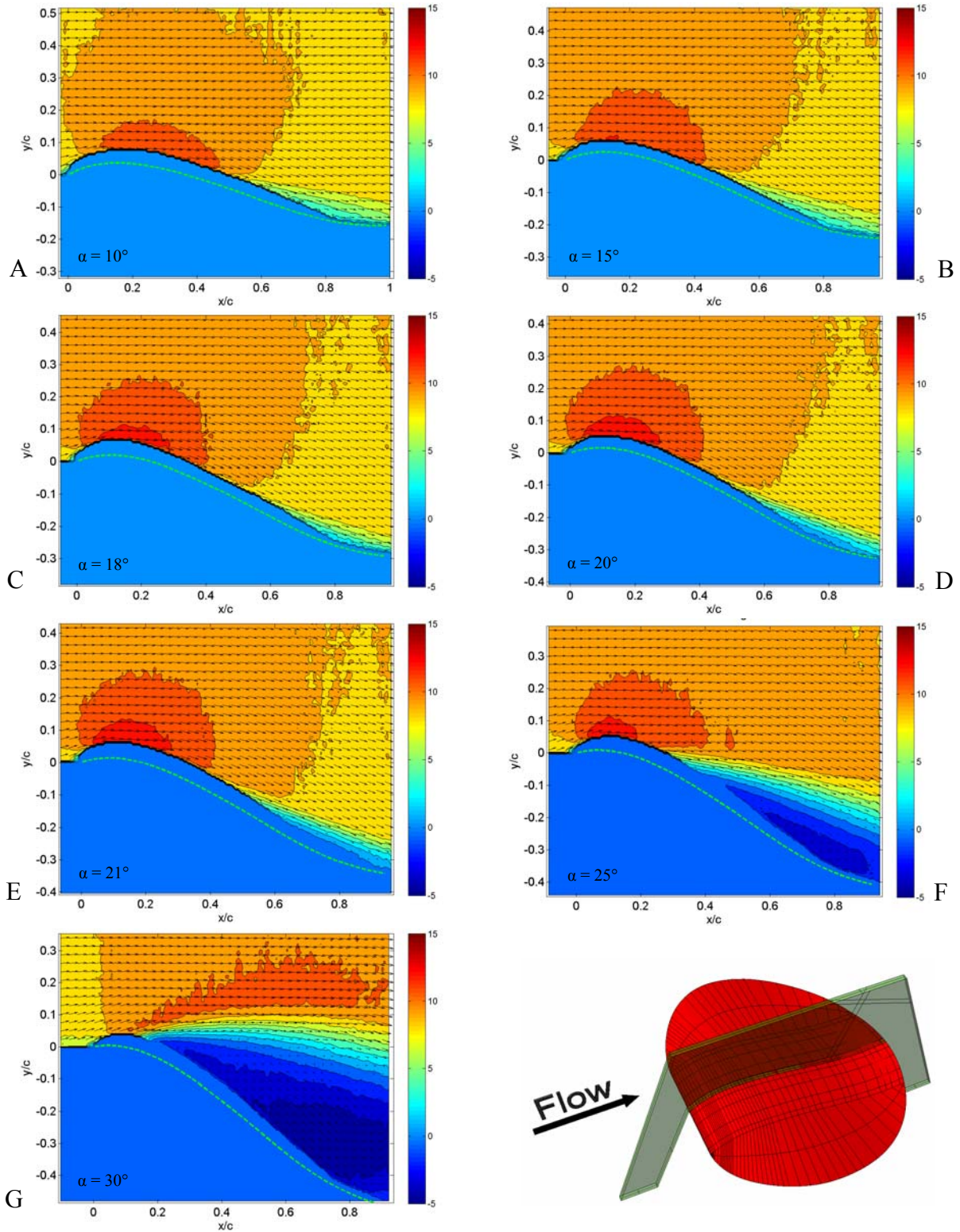


Figure 3-2. Distribution of the stream-wise velocity vectors in the flow field at various angles of attack, $z/b = 0$; A) 10° , B) 15° , C) 18° , D) 20° , E) 21° , F) 25° and G) 30° .

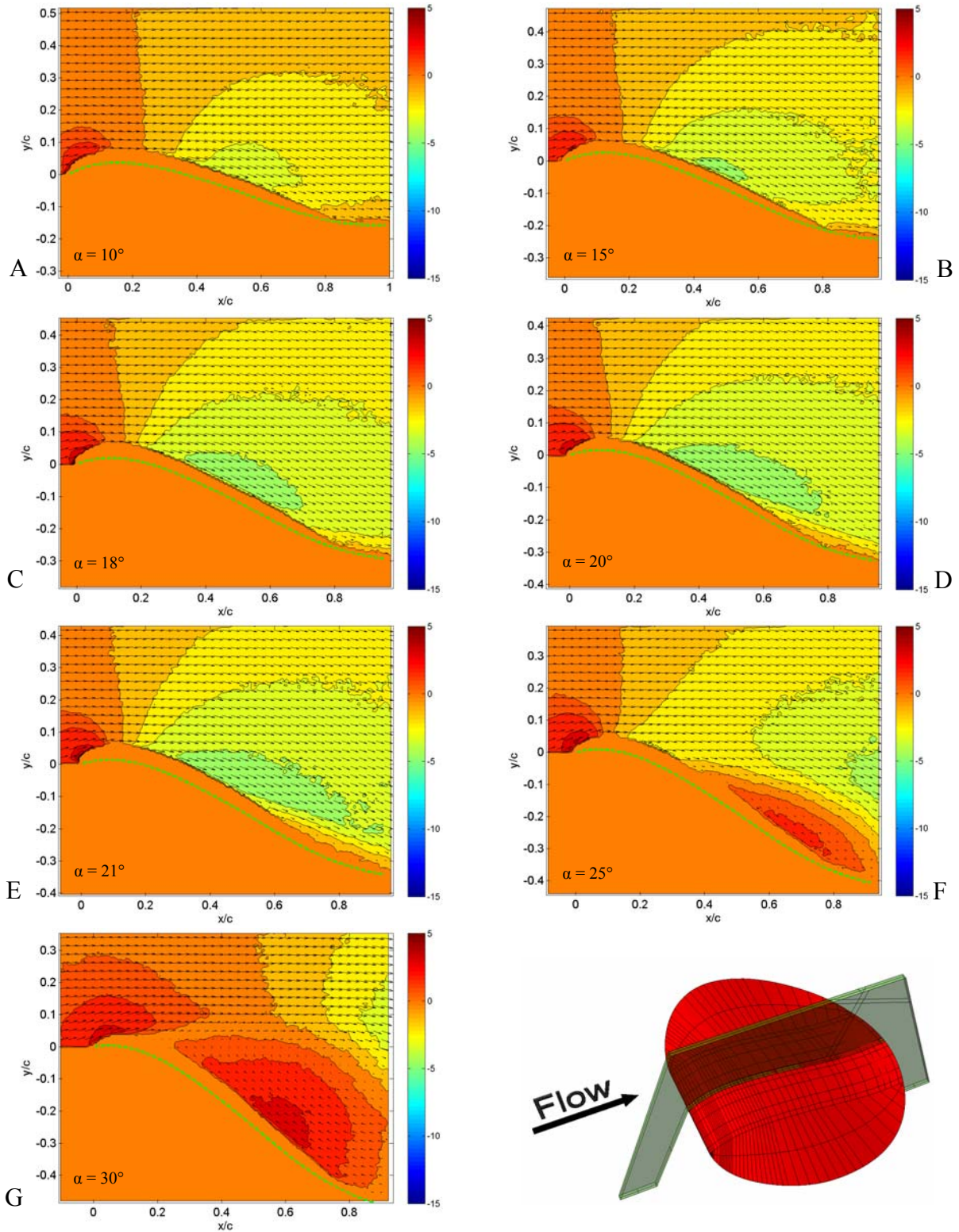


Figure 3-3. Distribution of the normal velocity vectors in the flow field at various angles of attack, $z/b = 0$; A) 10° , B) 15° , C) 18° , D) 20° , E) 21° , F) 25° and G) 30° .

However, at $z/b \geq 0.25$, the magnitudes of the normal component start to grow within the same region and it is believed that at this point, there is a larger effect of the wing-tip vortices on the flow over the wing, which would cause the flow to grow stronger in downward direction.

In Figure 3-4, the mean vertical velocity is plotted from the 2-component PIV measurements at $z/b = 0.46$ and for $\alpha = 10^\circ$. It is noticed that at $z/b = 0.46$, the measurement plane is adjacent to the core of the wing tip vortex and there is a strong downward spiral motion. At $z/b = 0.5$, the flow has transitioned to a relatively strong upward spiral motion, where $\bar{v} \sim 0.5\bar{U}_\infty$, and so it may be concluded that the center of the wing-tip vortex lies between $z/b = 0.46$ and $z/b = 0.5$ (Figure 3-4). It is also observed that the horizontal component of the velocity accelerates within the core of the separation region, as can be seen at $z/b \geq 0.46$.

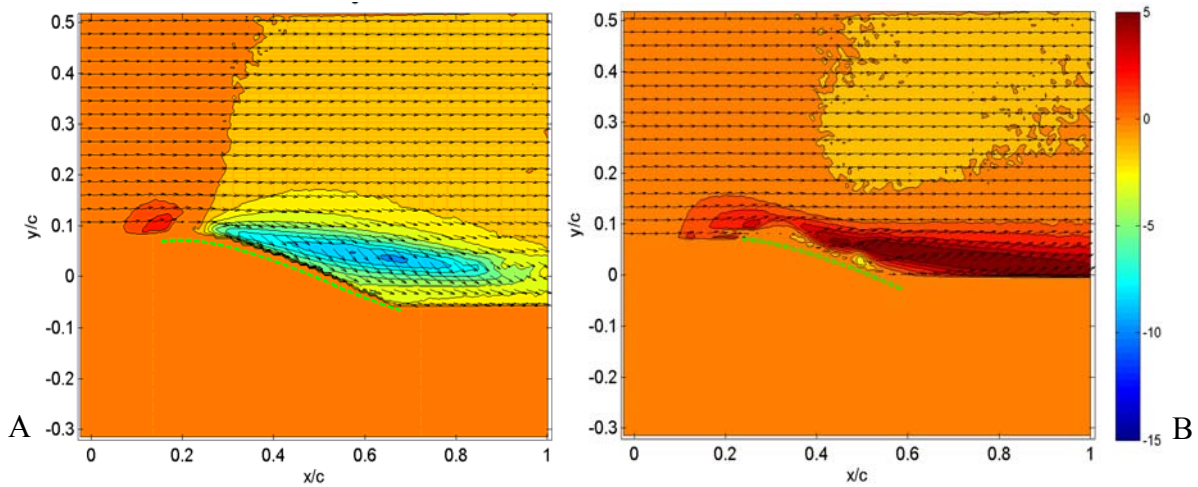


Figure 3-4. Distribution levels of the vertical component in the flow at $\alpha = 10^\circ$; A) indicating downward motion of the spiral at $z/b = 0.46$ and B) upward motion of the spiral at $z/b = 0.5$. Velocity is in m/s.

For $\alpha = 15^\circ$ (Figure 3-5), the distribution of \bar{u} and \bar{v} in the flow over the wing is similar to that when $\alpha = 10^\circ$. While the flow accelerates over the first half of the wing and then appears to separate in the measurements at $z/b = 0$ and between $x/c = 0.4$ & $x/c = 0.5$, the vertical component of the velocity continues to grow stronger in a downward direction as $z/b \rightarrow 0.5$.

Once again, it is hard to characterize the shear layer past $z/b > 0.25$ from the 2-component results, due to the fact that the dihedral of the wing obstructs the line of view adjacent to the surface of the wing (as seen in Figure 3-2). In the ensemble-averaged results at $z/b = 0.46$, there is a small region ($\sim 0.25c$ in length), that appears over the leading edge of the airfoil, with strong velocity gradients in the vertical direction ($\bar{v} \sim 1.4\bar{U}_\infty$), Figure 3-5A. This appears to be valid since the normal component of the velocity should be strongest in the flow closest to the core of the wing-tip vortex, at $x/c \sim 0.3$. Unfortunately, the reliability of the data at this location is also compromised due to the relatively higher number of estimated vectors in the region (Figure 3-5B), however, the results still seem plausible.

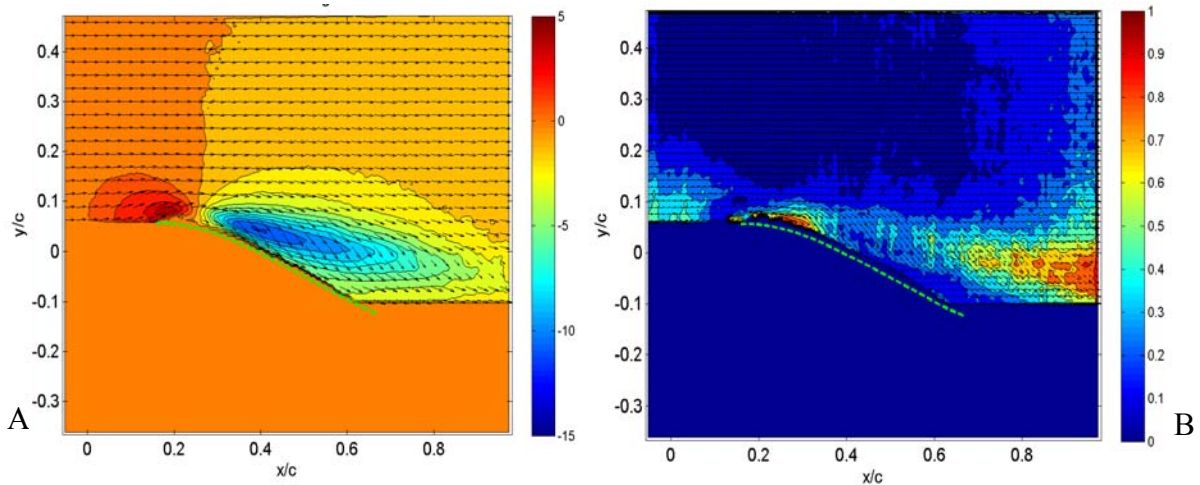


Figure 3-5. Distribution of the vertical component in the flow field at $\alpha = 15^\circ$ and $z/b = 0.46$. A) Showing a sharp velocity gradient in the stream-wise direction (m/s) and B) the distribution of estimated vectors in the measurement plane (normalized by the total number of vectors).

For $\alpha = 15^\circ$, the stream-wise and normal velocity components nearest to the wing surface (where $z/b < 0.25$) seem to maintain consistently low levels between the measurements at $x/c = 0.4$ and $x/c = 0.6$, possibly indicating the presence of a separation layer ($\sim 4\text{mm}$ thick). As would be expected (and as can be seen in Figure 3-6), the gradients in the stream-wise velocity in the vertical direction, $d\bar{u}/dy$, are large within the region of separation just above the surface of

the wing. It is also noted that this separation layer gradually thickens between $0.4 \leq x/c \leq 0.7$, but then starts to shrink, until at $x/c = 0.9$, where it appears as though the separation layer re-attaches to the surface, just before the trailing edge of the wing, Figure 3-7.

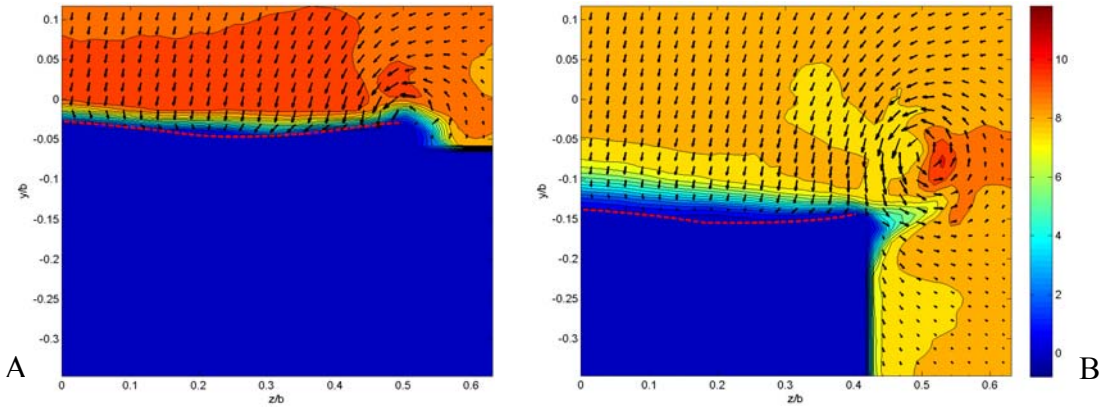


Figure 3-6. Distribution of the stream-wise component in the flow at $\alpha = 15^\circ$; A) $x/c = 0.4$ and at B) $x/c = 0.7$. Velocity is in m/s.

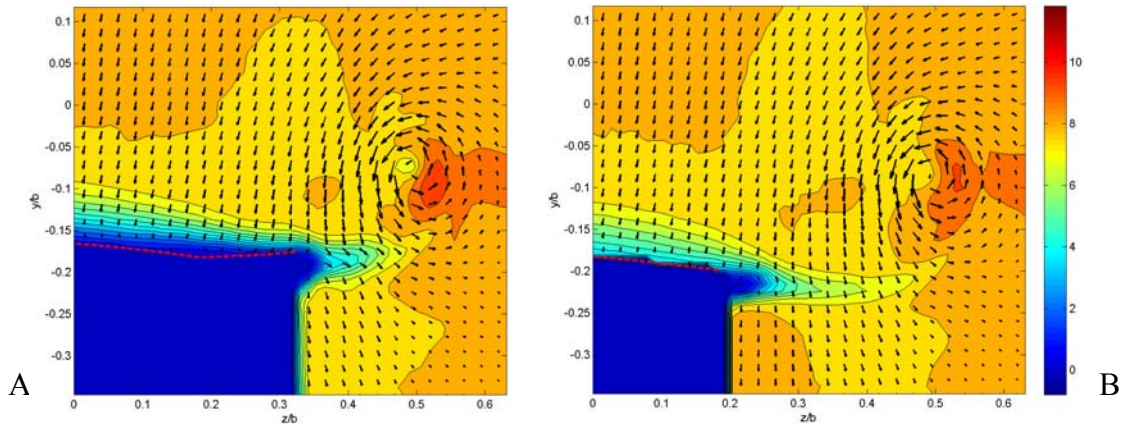


Figure 3-7. Distribution of the stream-wise component in the flow at $\alpha = 15^\circ$; A) $x/c = 0.8$ and at B) $x/c = 0.9$. Velocity is in m/s.

From Figure 3-8 it is interesting to note that at $\alpha = 15^\circ$, negative stream-wise vorticity is observed just above the wing surface and over the portion of the wing that forms the dihedral. The vector plots indicate that the circulating flow from the wing-tip vortex comes down directly on the dihedral of the wing and the flow gets re-directed toward the root of the wing along the wing surface, thus creating a small clock-wise flow over the wing. The region closest to the

wing ~ 4 mm in has a strong span-wise velocity component towards the root of the airfoil, thus inducing the flow above it to circulate in a clock-wise fashion. However, this trend is only observed in regions where the geometry of the wing re-directs part of the flow towards the wing root. In the latter half of the wing where $x/c \geq 0.7$, little is seen of this span-wise re-circulation.

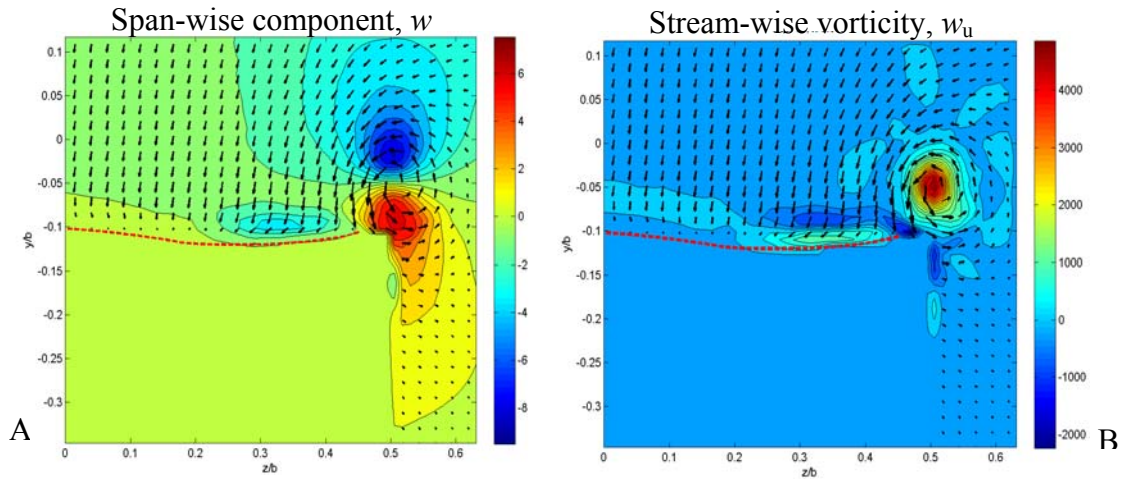


Figure 3-8. Distribution of the span-wise component of the flow, \bar{w} in m/s (A), and distribution of the stream-wise vorticity, s^{-1} (B), indicating span-wise re-circulation at $x/c = 0.6$ and at $\alpha = 15^\circ$.

The 3-component PIV results also show the development and downstream progression of the wing tip vortex. It is interesting to note that in the center of the tip-vortex, the magnitude of the stream-wise component does not grow much weaker than the free-stream velocity until the flow is in the vicinity of $x/c = 1.1$ (where $\bar{u} \sim 0.6\bar{U}_\infty$).

The vortex core also appears to move down and towards the root of the airfoil as the flow progresses downstream of the leading edge. The change in the vertical position of the vortex core was as much as 15 mm between $x/c = 0.3$ and $x/c = 1.1$, while the horizontal change in position was ~ 7 mm. This behavior may be attributed to the downwash over the wing and the effect of the dihedral on the flow over the wing. The dihedral on the wing is supposed to promote roll stability by generating equal amounts of lift on both sides of the wing, thus re-

directing some of the lift force to be angled in towards the root of the airfoil and in the process turns the flow.

The 2-component PIV results for the $\alpha = 18^\circ$ case show that the height of the shear layer above the surface of the wing has decreased and it is speculated that separation has been delayed till the flow is a little further downstream than in the previous two cases. The flow of the wing is similar to the $\alpha = 15^\circ$ case, except that the vertical component of the velocity has stronger downward momentum, possibly due to the downwash over the wing. The wing-tip vortices have also grown stronger and appear to affect a larger region of the flow above the wing than before (Figure 3-9), as far in as $z/b = 0.375$, where a region of strong downward flow is observed in the core of the separated flow in the wake of the wing, ($\bar{v} \sim 0.9\bar{U}_\infty$). These observations are corroborated by looking at the results from the 3-component PIV setup, where one can see a region of high downward velocity between $z/b = 0.3$ and $z/b = 0.5$. As seen in Figure 3-10, the stream-wise velocity builds up momentum on the outside of the vortex core ($\sim 1.2\bar{U}_\infty$), and that the velocity on the side of the vortex core, closer to the wing tip, is almost the same as the free-stream velocity, $\sim 0.95\bar{U}_\infty$. In this case, the velocity in the core of the vortex starts showing signs of slowing down where $x/c > 0.7$ ($\bar{u} \sim 0.75\bar{U}_\infty$). It maintains this velocity till $x/c = 1.0$ and then suddenly loses even more momentum for $x/c \geq 1.1$, where $\bar{u} \sim 0.45\bar{U}_\infty$. It is only after $x/c \geq 1.4$, that the stream-wise component in the core picks up momentum again, $\bar{u} \sim 0.75\bar{U}_\infty$.

The velocity distributions of the three separate components of the flow also indicate the presence of a separation layer past $x/c = 0.4$. The separation layer starts with a thickness of approximately 2 mm and transitions to a ~ 5 mm thick layer at $x/c = 0.5$, after which it shrinks in size and is not visible by the time the flow reaches $x/c = 0.9$. Perhaps, this trend indicates that

the separated shear layer was re-attaching itself to the wing surface before the flow left the TE of the wing. It is also worth noting that as the flow moves further downstream, the effect of the wing-tip vortex on the vertical component of the flow over the wing grows weaker.

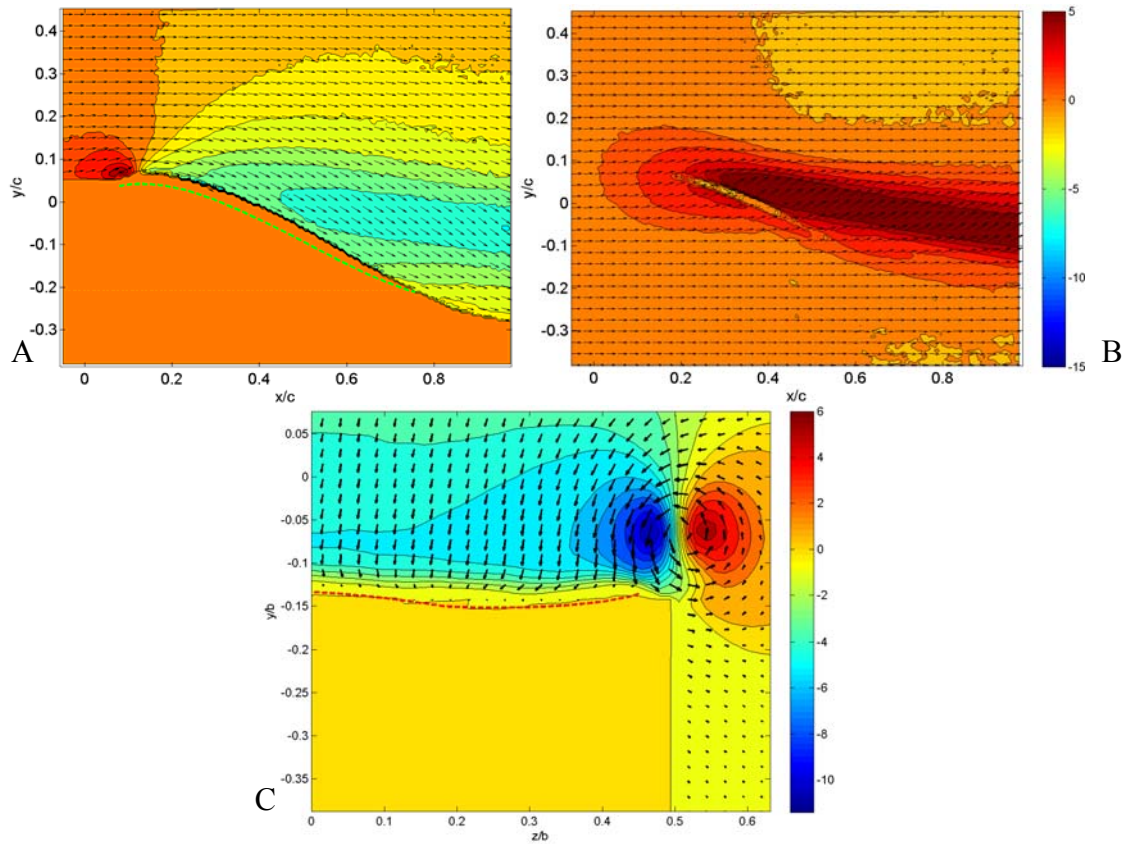


Figure 3-9. Plots showing the regions of strong downward and upward flow near the wing-tip at $\alpha = 18^\circ$; A) 2-component PIV at $z/b = 0.375$, B) 2-component PIV at $z/b = 0.5$ and C) the corresponding 3-component PIV results. The vertical component of the flow, \bar{v} , is depicted in the contour levels (m/s).

As was inferred for the previous case, when the circulating flow from the wing-tip vortex comes in contact with the dihedral of the wing, a portion of the flow is directed towards the wing root, causing positive stream-wise vorticity closest to the wing surface and negative vorticity, of comparable strength, just above it. But in this case, it was also observed that at the root of the wing, circulating flow from the tip vortex is re-directed back towards the wing-tip causing negative stream-wise vorticity close to the wing surface (in the center half of the wing), and

positive vorticity just above it. This phenomenon is clearly observed in the measurements taken between $x/c = 0.3$ and $x/c = 0.8$, Figure 3-11. In these regions, there is a considerable dihedral in the wing and the tip vortex is close enough to the edge of the wing so as to force a portion of the circulating flow onto it. After $x/c \geq 0.9$, there is relatively little momentum in the span-wise component of the velocity in the flow over the wing.

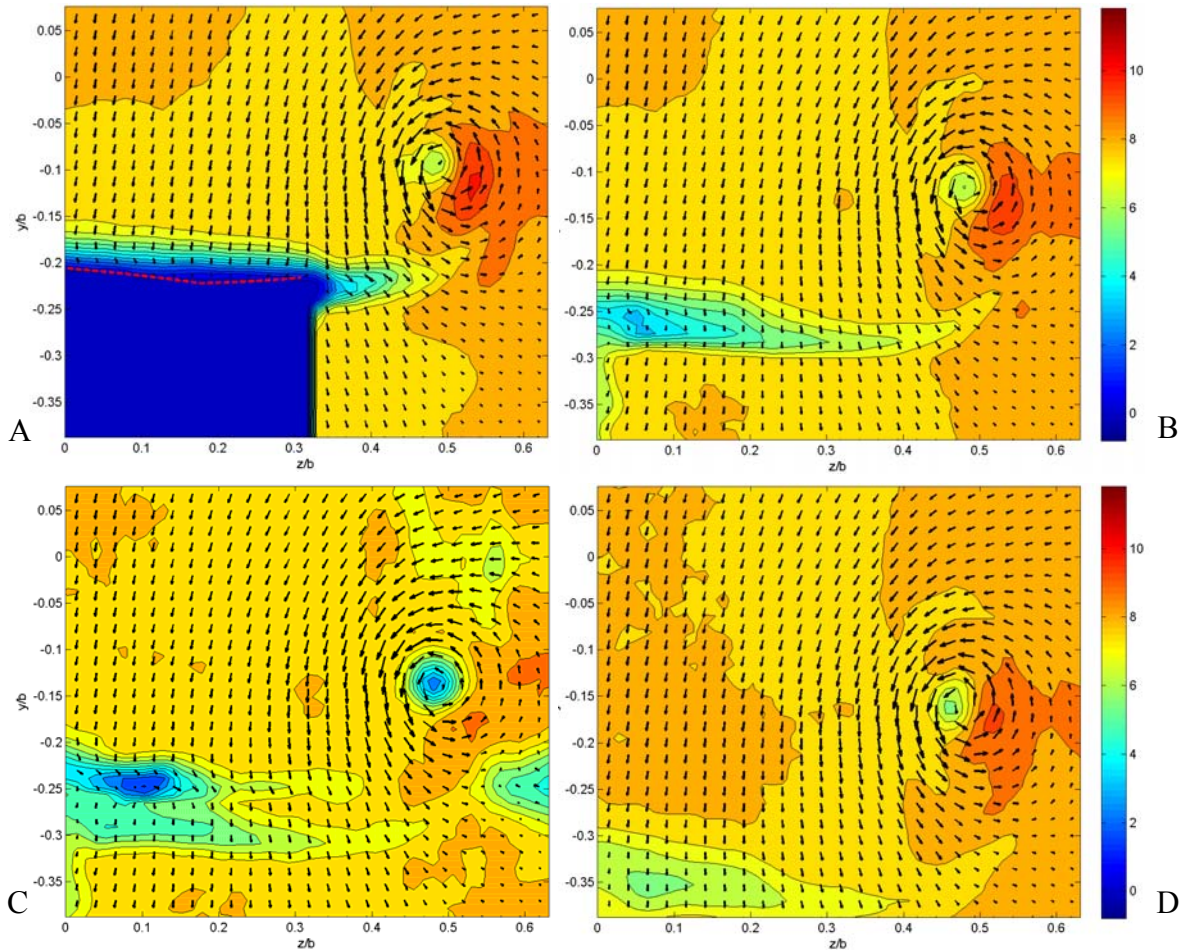


Figure 3-10. Stream-wise velocity distribution, \bar{u} , and the progression of the wing-tip vortex downstream over the wing for $\alpha = 18^\circ$ and at: A) $x/c = 0.8$, B) $x/c = 1.0$, C) $x/c = 1.1$ and D) $x/c = 1.4$. Velocities are in m/s.

Due to the downwash over the wing, the vortex center also moved lower as the flow progressed downstream of the leading edge (~ 23 mm, for $0.3 \leq x/c \leq 1.4$), and also moved slightly in the direction of the root of the airfoil (~ 7 mm).

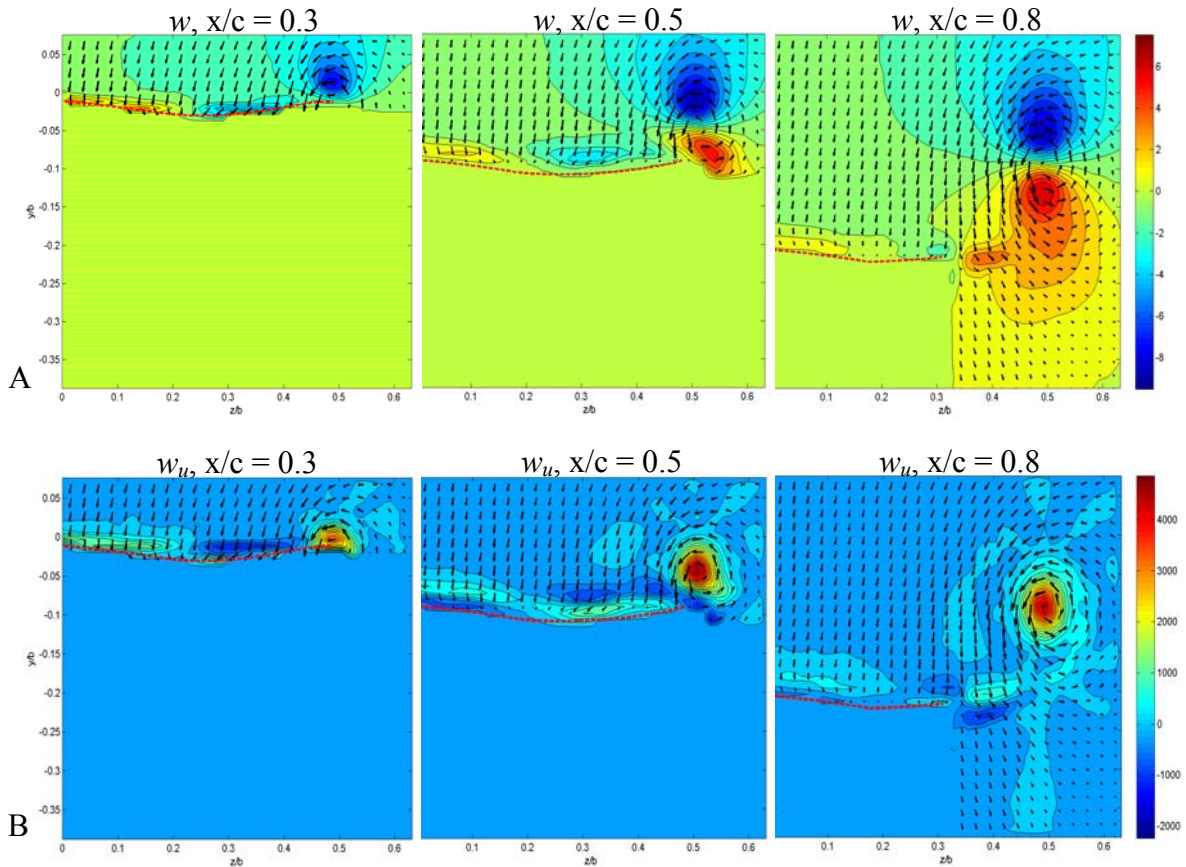


Figure 3-11. Measurements in different chord-wise planes, indicating the presence of span-wise circulation over the wing at $\alpha = 18^\circ$; A) Distribution of the span-wise component of the velocity in the flow field and B) Stream-wise vorticity (ω_z) in the flow field, at $x/c = 0.3$ (left), $x/c = 0.5$ (center) and $x/c = 0.8$ (right). Velocities are in m/s.

For the $\alpha = 20^\circ$ case, the 2-component PIV results showed that the stream-wise flow over the first half of the airfoil was accelerated to higher levels than had been seen in the previous cases ($\bar{u} \sim 1.5\bar{U}_\infty$). This was coupled with an increase in the magnitude of the downward component of the flow where $0.3 \leq x/c \leq 0.8$, Figure 3-2D & Figure 3-3D. It was noted that the levels of \bar{u} near the LE of the wing grew larger as $z/b \rightarrow 0.5$. The measurements at $z/b \geq 0.33$ show the development of a gradient in the distribution of the normal velocity vectors in the wake of the wing. The magnitude of the velocity levels grows larger close to the center of this region and grows stronger as $z/b \rightarrow 0.5$. This pattern depicts the flow within the wing-tip vortex core

where the normal components of the velocity are the strongest. The plots also indicate that the center of the wing tip vortex may lie between $z/b = 0.46$ and $z/b = 0.5$. In addition, the results showed an increase in the thickness of the separation layer above the wing at $x/c = 0.8$ as compared to the results in the previous case (~ 12 mm thick).

For the $\alpha = 21^\circ$ case, velocity distributions from the 2-component PIV results indicate that the flow over the wing may be separating further upstream than in the previous cases, see Figure 3-2 & Figure 3-3. The results from the 3-component PIV data did not indicate any new characteristics in the flow over the wing than what has been previously observed. Since this was at higher angle of attack, the wing-tip vortices were stronger than in the previous cases, and as a result, the magnitudes of the components of the flow around the vortex center were stronger as well, in particular, the downward component of the circulating flow from the tip vortex appeared to be dominant over a larger section of the wing than before. The distribution of the span-wise component of the flow, once again, indicated the presence of opposing span-wise recirculation taking place over the central part and the dihedral portion of the wing.

The development of the separation layer is also visible in a distribution of the stream-wise and vertical component results from the measurements where $x/c \geq 0.4$. The separation layer maintains a maximum thickness of ~ 4 mm between $0.5 \leq x/c \leq 0.7$. Downstream of this location, the separation layer begins to get smaller ($0.8 \leq x/c \leq 0.9$) and it appears as though the flow tries to re-attach to the wing surface just before the trailing edge of the wing. Like the other cases, there is a downward (~ 25 mm at $x/c = 1.4$), and sideways (~ 7 mm at $x/c = 1.4$) motion of the wing-tip vortex center as the flow progresses downstream.

The PIV results at $\alpha = 25^\circ$ indicated a stalled condition for the airfoil, the flow over the wing having completely separated from the surface of the wing. Similar to the previous cases,

the 2-component PIV results show that the flow speeds up over the top of the airfoil, but shortly after, at $x/c \sim 0.15$, the flow comes in contact with an adverse pressure gradient and a separated shear layer is formed. Within this layer and closest to the wing surface is a region of re-circulating flow with a maximum stream-wise component $\sim 0.6 \bar{U}_\infty$ and a maximum normal component $\sim 0.5 \bar{U}_\infty$, Figure 3-12. This region of re-circulating flow is largest at $z/b = 0$, after which it shrinks in size as $z/b \rightarrow 0.5$.

The results from the 2-component PIV setup show separated flow over the wing without any re-circulation in the instances where $z/b \geq 0.25$. For $z/b \geq 0.25$, the stream-wise component of the flow forms a shear layer over the wing surface with strong vertical gradients in the velocity. The normal component of the flow also forms a gradient in the wake of the airfoil, but in this case, the gradients are almost axially symmetrical about $y/c \sim -0.14$, where the innermost region contains the flow with the strongest downward component.

The results from the 3-component PIV data are similar in nature to the results from the other cases. When looking at the distribution of the velocity components over the flow field one can clearly observe the development of a large region of separation between $0.3 \leq x/c \leq 1.4$. At $x/c = 0.3$, the flow over the airfoil is very close to surface of the wing (< 2 mm). One can see the wing-tip vortex developing and also see the span-wise circulation that has been discussed earlier. At $x/c = 0.4$, the stream-wise and vertical components of the flow begin to separate from the surface while the span-wise component of the flow is still attached and still showing signs of span-wise re-circulation.

Between $0.5 \leq x/c \leq 0.9$, the region of re-circulating stream-wise flow continues to grow in height but is bounded on the sides by the flow around the perimeter of the wing. This region of re-circulating flow is thickest over the middle of the airfoil at $x/c = 0.8$ and $z/b = 0$, ~ 18 mm tall.

Adjacent to this region and all around it is the separated shear layer over the wing that is approximately 9 mm thick at $z/b = 0$ and the top layer of which is ~ 27 mm from the surface of the wing at $x/c = 0.8$, Figure 3-13.

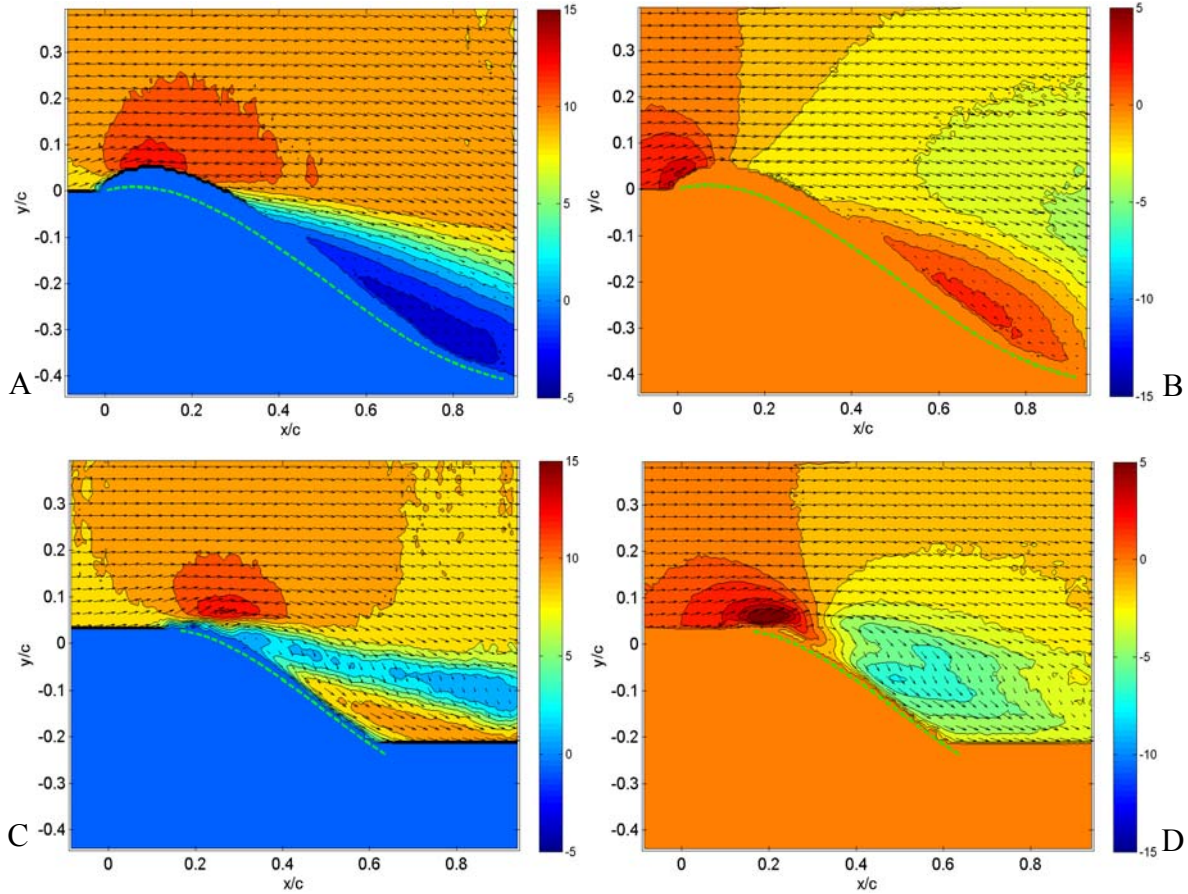


Figure 3-12. Distribution of the ensemble-averaged stream-wise and normal components of the flow field (m/s), at $\alpha = 25^\circ$. A) \bar{u} at $z/b = 0$, B) \bar{v} at $z/b = 0$, C) \bar{u} at $z/b = 0.46$ and D) \bar{v} at $z/b = 0.46$.

It seems as though the phenomenon of re-circulating flow over the back of the wing is primarily two dimensional, i.e. the u & v vectors contribute mostly to the characteristics of the flow. The span-wise velocity in this region of re-circulation is very low and negative, indicating a slight flow in the direction of the wing root. Corresponding with the negative levels in the distribution of the stream-wise component of the flow, the vertical component of the flow indicates regions of slightly positive flow, which is intuitive and corroborates the results from the

2-component PIV setup. The region of negative stream-wise flow extends beyond the trailing edge of the wing, as is observed in the measurements at $x/c = 1.1$ (Figure 3-13), but not thereafter, giving some idea of how far the region of re-circulation extends into the wake of the wing. The stream-wise component of the flow over the wing is also considerably faster in the measurements at $x/c = 0.3$ and loses a lot of momentum by the time the flow reaches $x/c = 1.4$.

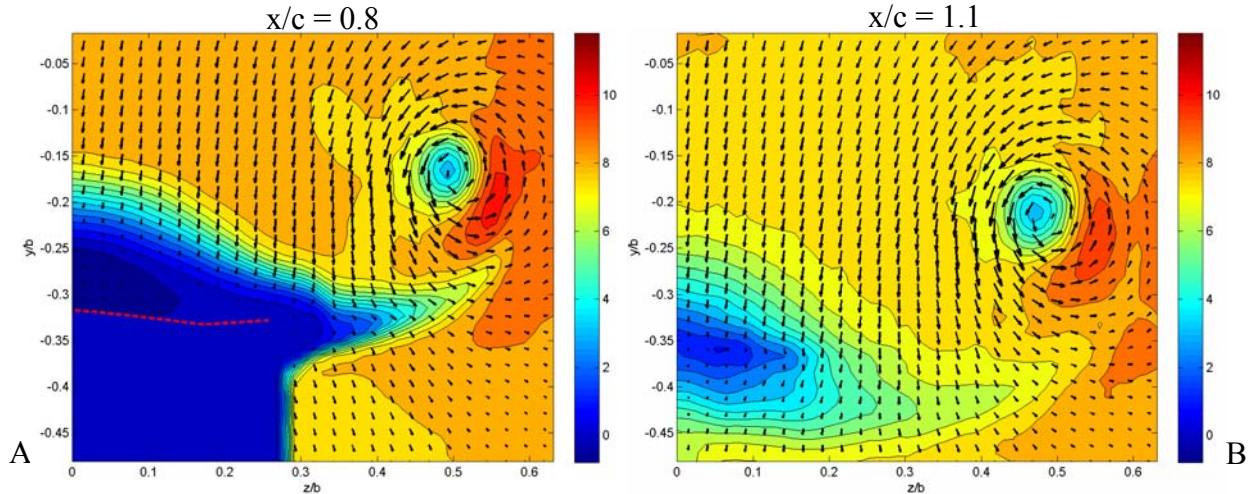


Figure 3-13. Distribution of the stream-wise component in the flow (m/s), at $\alpha = 25^\circ$; A) $x/c = 0.8$ and B) $x/c = 1.1$.

For all the cases, 2-component PIV results showed that small pockets with high levels of span-wise vorticity were developing at the leading edge of the airfoil in the region close to the wing-tips. At these locations the flow can be seen going around (separating then re-attaching), what appears to be a separation bubble. However, since these bubbles reside in the regions closest to the wing surface, this phenomenon could not be accurately documented.

Looking at the 2-component PIV results in Figure 3-14 & Figure 3-15, for $\alpha = 25^\circ$, the presence of a separation bubble was inferred close to the leading edge of the airfoil at a span-wise location of $z/b = 0.42$. There is a clear separation of the flow from the surface of the wing at $x/c \sim 0.1$ and then a re-attachment of the flow to the wing $x/c \sim 0.35$. Even though the recirculation within the bubble is not visible (due to a partially obstructed view), the flow vectors

can clearly be seen going over the top of the bubble and then re-attaching to the wing surface behind it.

However, in the ensemble-averaged data collected at $z/b = 0.46$ for the same angle of attack, this bubble appears to be unstable, leading to separation of the flow over the wing, and again creating high vorticity levels near the point of separation. It is possible that the circulatory flow induced by the tip vortex creates an adverse pressure gradient in the stream-wise direction in the regions near the wing-tip; this adverse pressure gradient then leads to the separation of flow over the airfoil at that span-wise location. Because of the complex interactions between the flow over the wing and the circulatory flow induced by the wing-tip vortex, the exact cause of separation at this location is unknown. It is plausible that vortex shedding could be taking place at this location over the wing.

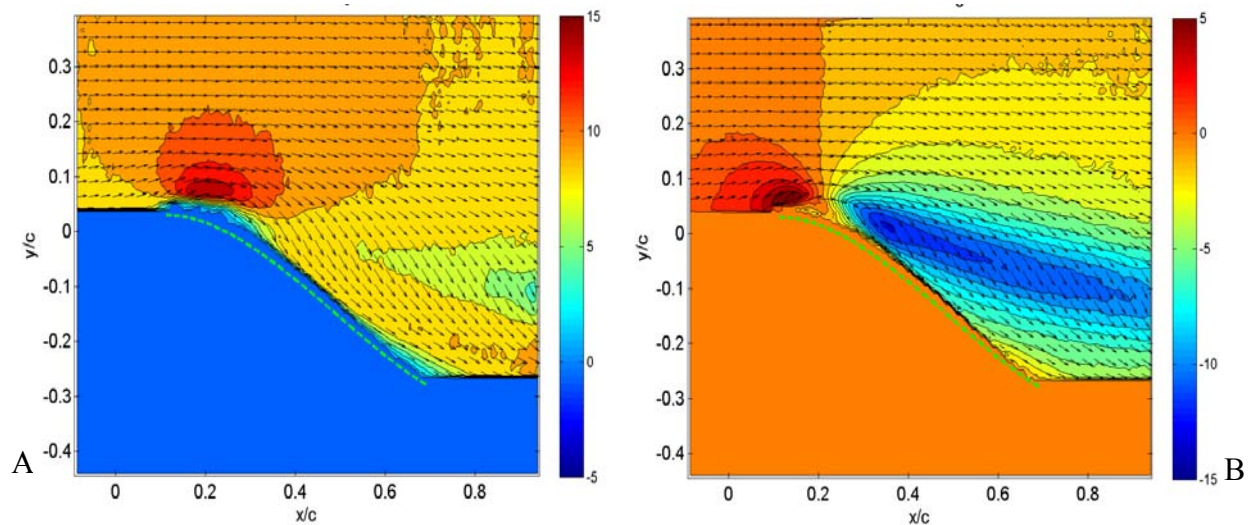


Figure 3-14. Flow field distributions for $\alpha = 25^\circ$ and $z/b = 0.42$; A) stream-wise component of the velocity and B) the normal (vertical) component of the velocity.

The presence of a separation bubble at $\alpha = 25^\circ$ and $z/b = 0.42$ could also be inferred from Figure 3-16, where the span-wise vorticity levels indicate the presence of recirculation within the

region of separation. One can also clearly see the instability of the separation bubble at the leading edge at $z/b = 0.46$.

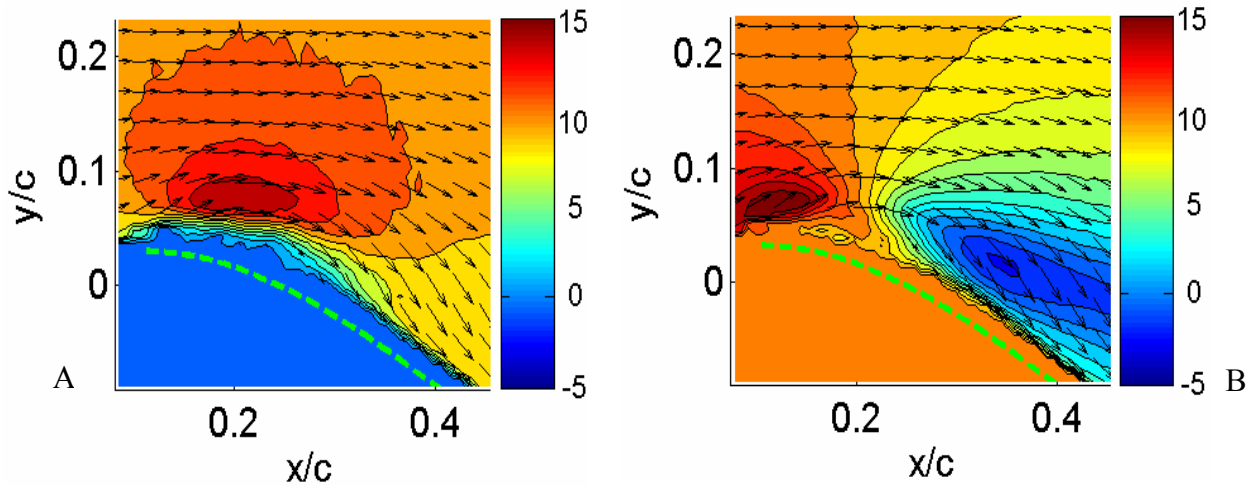


Figure 3-15. Close up of the flow over the leading edge of the wing at $\alpha = 25^\circ$ and at $z/b = 0.42$; A) stream-wise component and B) the normal component.

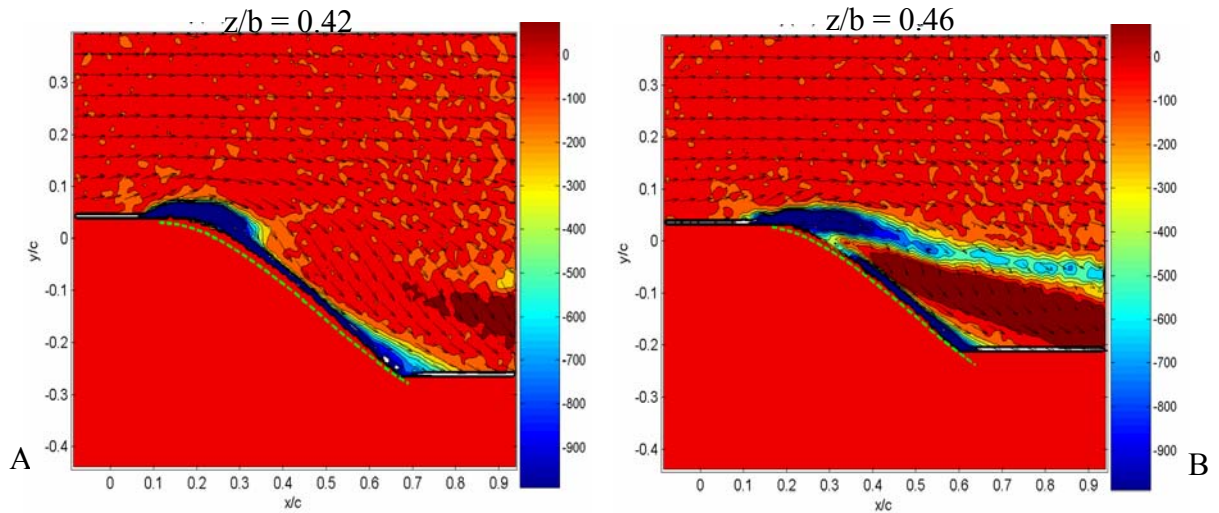


Figure 3-16. Span-wise vorticity levels (s^{-1}) at $\alpha = 25^\circ$; A) at $z/b = 0.42$ and B) $z/b = 0.46$.

For $\alpha = 30^\circ$, the flow behind the wing was massively separated just downstream of the leading edge of the airfoil. Since the flow is now massively separated, there is no visible sign of any separation bubbles along the span of the airfoil.

Fluctuating Velocity Levels in the Flow

As described in the previous section, the velocity fluctuations in the flow over the airfoil occur primarily within the shear layer that develops over the top of the wing. Figure 3-17 & Figure 3-18 show a distribution of the fluctuations in the stream-wise and normal components of the flow, normalized by the free-stream velocity (u'_{rms}/\bar{U}_∞ and v'_{rms}/\bar{U}_∞). The normalized turbulent shear stress levels ($\overline{u'v'}/\bar{U}_\infty^2$), have been shown in Figure 3-19. All of these plots are along the centerline of the wing at various angles of attack.

In the figures, for the case where $\alpha \leq 21^\circ$, the highest velocity fluctuations and turbulent shear stress levels are observed to be close to the center of the shear layer, which appears to be just barely separated. However, for $\alpha = 25^\circ$ & 30° , the shear layer is definitely no longer attached to the top surface of the airfoil, instead, a large region of separation is formed over the wing, with flow re-circulating from the trailing edge to the leading edge of the airfoil. It should be noted that even though it is not clearly visible due to the inability to view near the wing surface, the lower angles of attack most likely, do exhibit re-circulating flow.

In these cases, the highest levels of stream-wise fluctuations reside in a region close to the upper boundary of the separated flow, where a shear layer is present and where there is a large velocity gradient in the y direction (Figure 3-17). However, the highest levels of fluctuations in the normal component are observed in the latter half of the region of separation, where the velocity gradient is highest in a direction that is almost normal to the surface of the wing. As expected, the fluctuations in the stream-wise direction are greater in magnitude as compared to the velocity fluctuations in the normal direction. It can be observed that there is a general increase in the fluctuation intensities and thickness of the shear layer with increasing angle of attack, except around 18° .

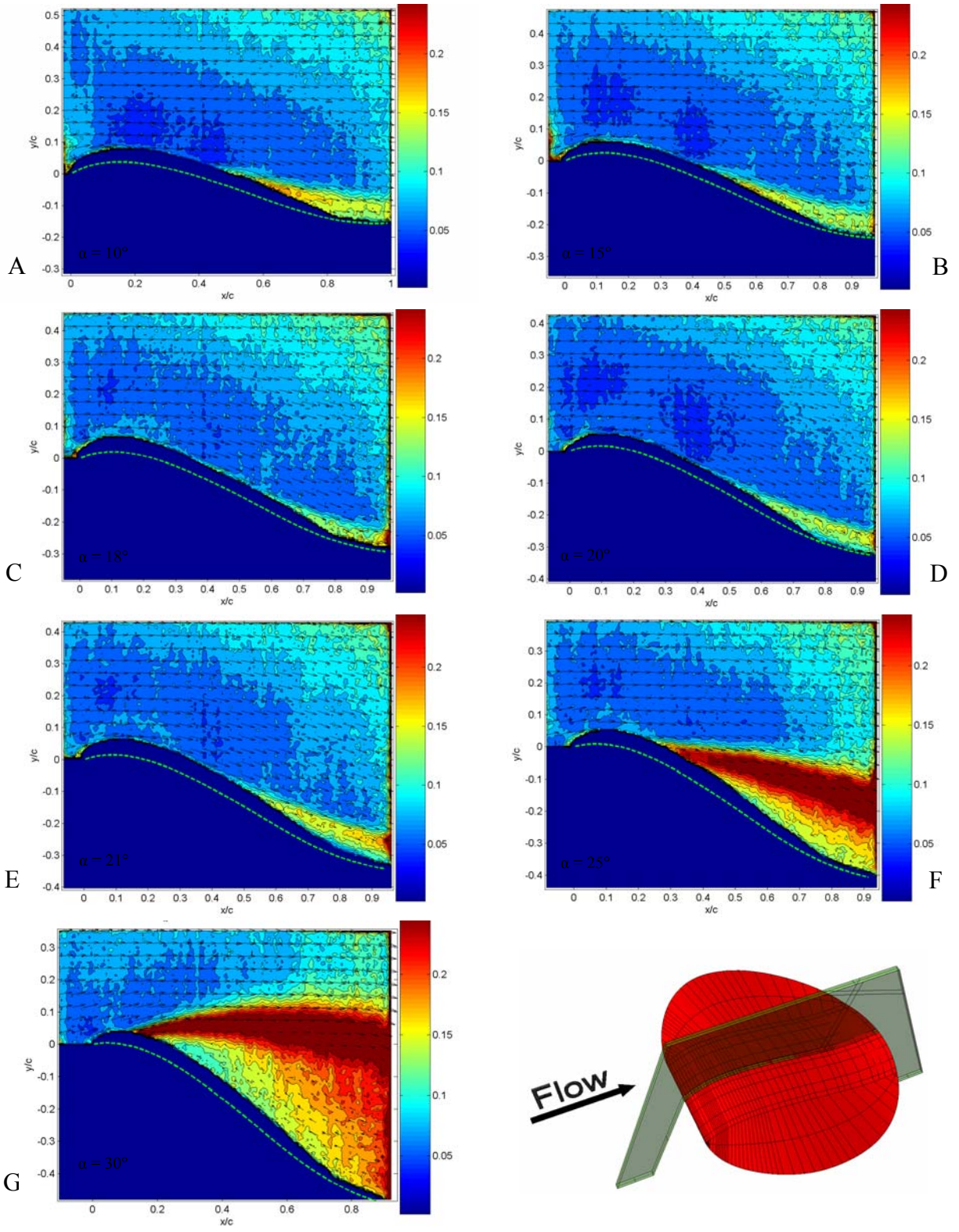


Figure 3-17. Distribution of the stream-wise velocity fluctuation levels in the flow field at various angles of attack at $z/b = 0$; A) 10° , B) 15° , C) 18° , D) 20° , E) 21° , F) 25° and G) 30° .

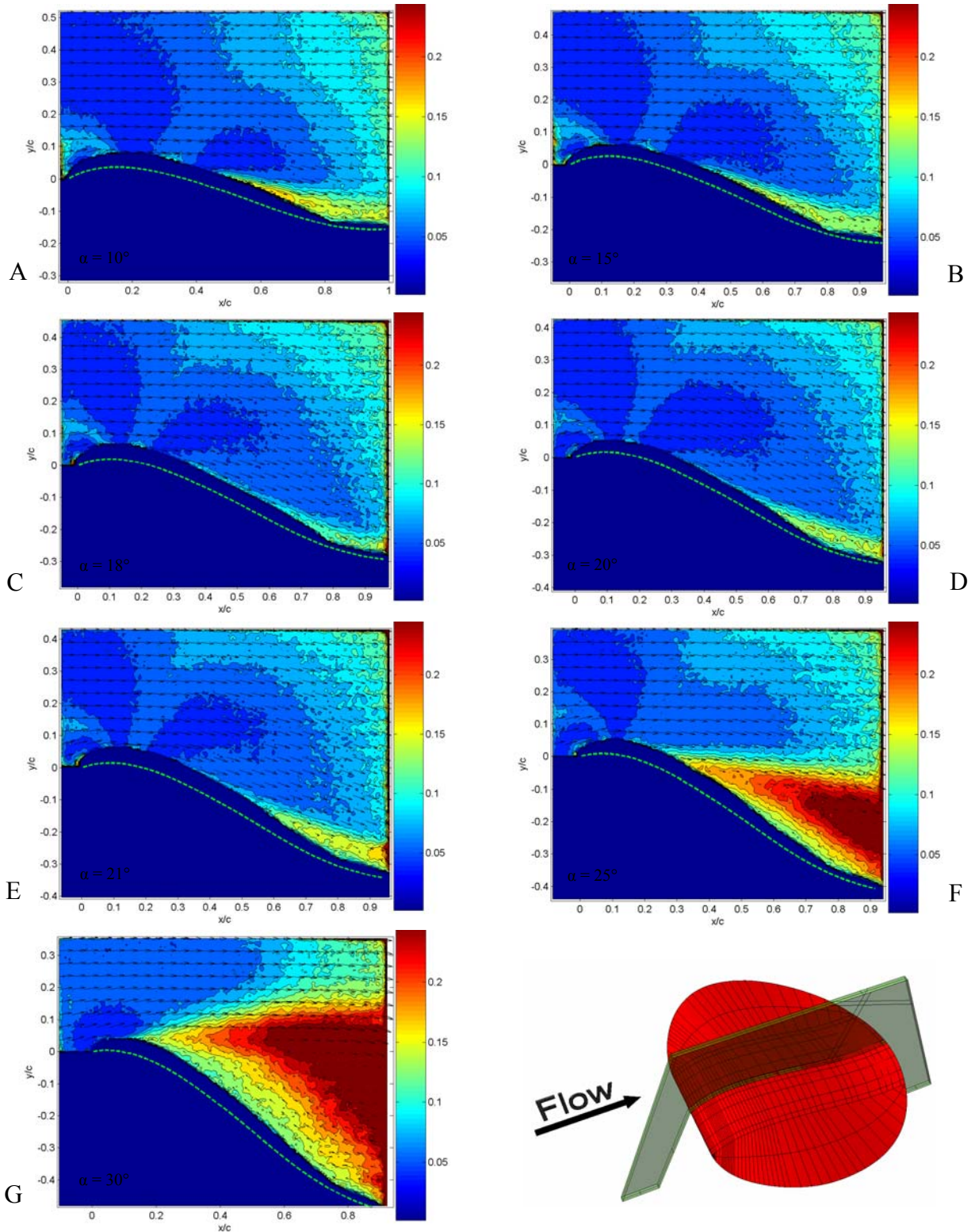


Figure 3-18. Distribution of the normal velocity fluctuation levels in the flow field at various angles of attack at $z/b = 0$; A) 10° , B) 15° , C) 18° , D) 20° , E) 21° , F) 25° and G) 30° .

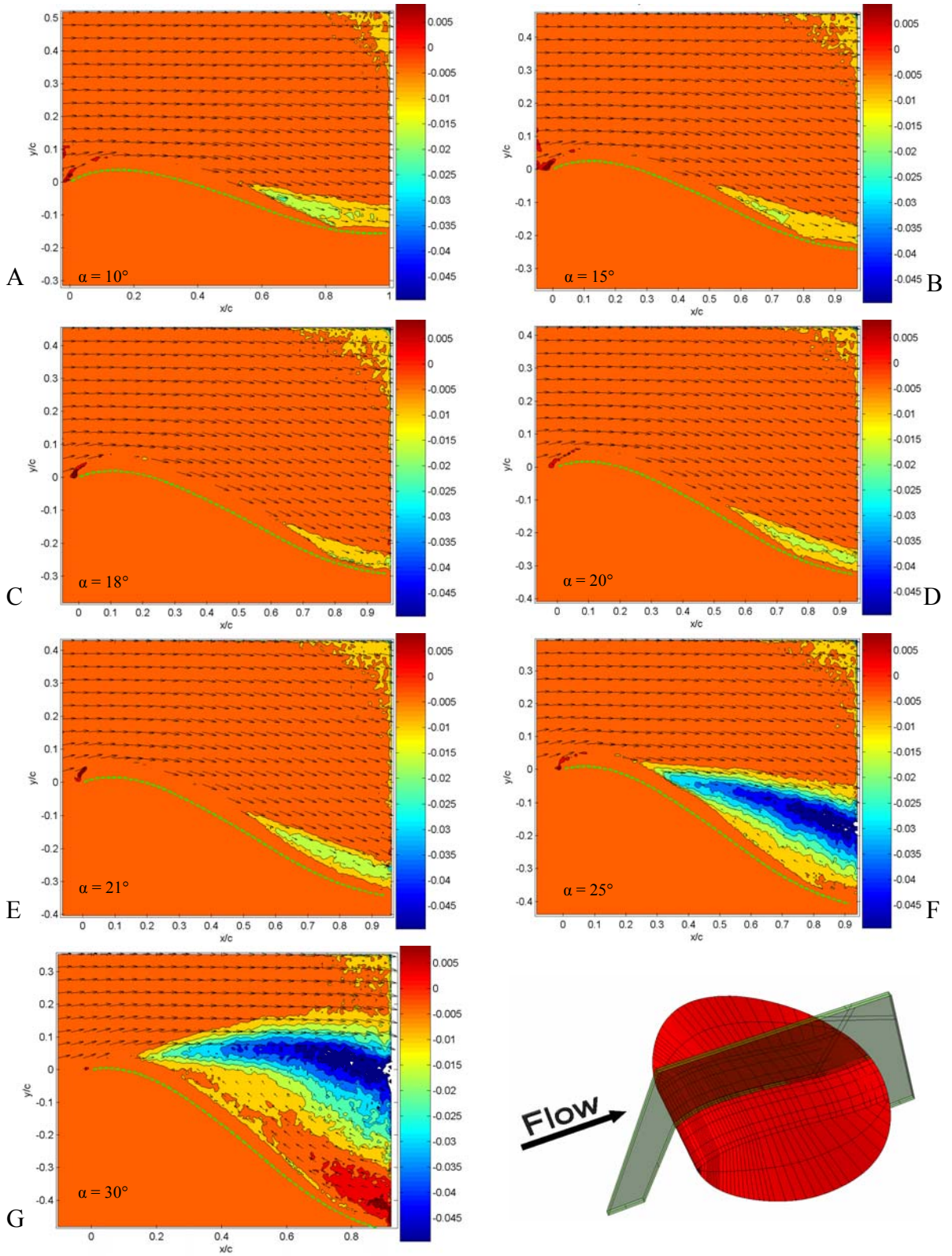


Figure 3-19. Distribution of the turbulent shear stress levels in the flow field at various angles of attack at $z/b = 0$; A) 10° , B) 15° , C) 18° , D) 20° , E) 21° , F) 25° and G) 30° .

For the cases where $\alpha \leq 21^\circ$, Figure 3-19 reveals negative peaks in the turbulent shear stress close to the inner regions in the shear layer over the reflex of the airfoil. The magnitudes of the shear stresses in these regions of the shear layer can be almost twice as large as the stresses in the outer region of the shear layer. However, for $\alpha = 25^\circ$ & 30° , the negative peaks in the turbulent stress levels reside closer to the bottom of the separated shear layer that forms over the wing (Figure 3-19F & G), whereas the positive peaks are in the region of re-circulating flow that is closest to the surface of the wing as is seen in Figure 3-19G.

Small pockets of high fluctuating levels are also observed at the leading edges of the wing (beyond $z/b = 0.25$), and appear to get stronger as $z/b \rightarrow 0.5$. At $z/b = 0.46$, a region is observed in the flow adjacent to the wing, where the fluctuating velocity levels appear to be relatively higher than over the other regions of the airfoil. The ensemble-averaged data here could be representative of some periodic shedding taking place at the leading edge at this location or it might be the effect of the wing-tip vortices. Also, at this same span-wise location and at $\sim x/c = 0.9$, a region of high fluctuating velocity levels develops in the wake of the airfoil (Figure 3-20).

For some angles of attack, this region with high levels of fluctuations was also identified in the results from the 3-component PIV experiments. However, it should be noted that the percentage of estimated vectors in these regions is large, due to the flow being highly three dimensional and causing in-plane dropout, effectively reducing the reliability of the results in those regions.

For the $\alpha = 10^\circ$ case, the stream-wise fluctuations within the separation layer, are in the range of 10-28 % of the free-stream velocity and the normal fluctuations are in the range of 10-15 % of \bar{U}_∞ . Between the regions of high and low fluctuating velocities in the shear layer, the normalized turbulent shear stresses range between ~ -0.01 and ~ -0.025 .

At $\alpha = 15^\circ$, it is interesting to see that the thickness of the shear layer decreases slightly at $z/b = 0$ (Figure 3-17 & Figure 3-18), and that the fluctuating velocity levels have a lower range of values. The turbulent shear stress also peaks at ~ -0.017 , as compared to ~ -0.025 at $\alpha = 10^\circ$. At $\alpha = 18^\circ$, the thickness of the shear layer above the wing shrinks considerably, and the fluctuation levels in the visible flow are the lowest amongst all the cases ($8\% \leq u'_{rms}/\bar{U}_\infty \leq 14\%$ and $8\% \leq v'_{rms}/\bar{U}_\infty \leq 14\%$). The smaller shear layer also has a lower range of turbulent shear values, ~ -0.01 .

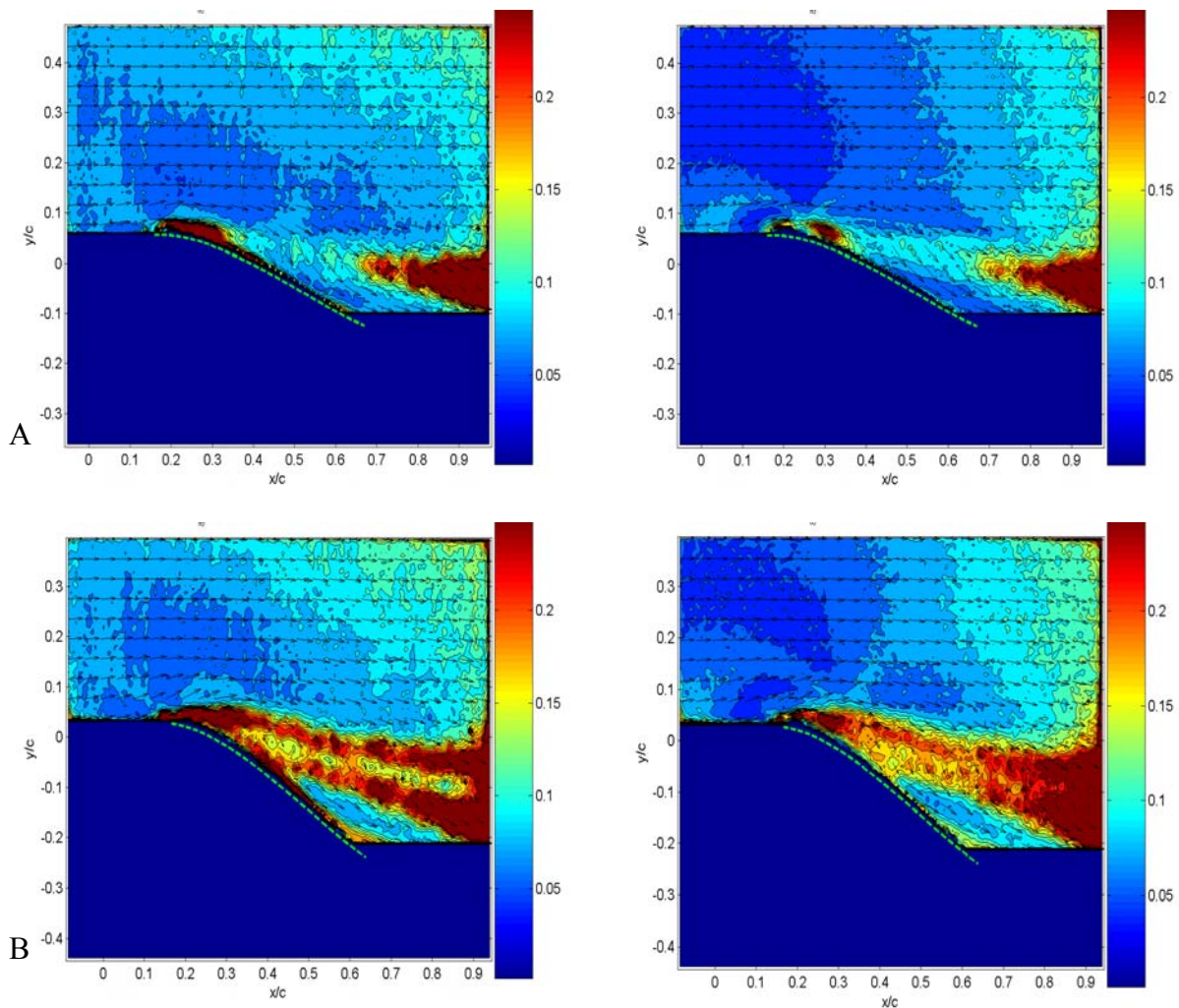


Figure 3-20. High fluctuation levels in the stream-wise (left) and the normal (right) components of the flow, at $z/b = 0.46$ and at, A) $\alpha = 15^\circ$, and B) $\alpha = 25^\circ$.

Between $20^\circ \leq \alpha \leq 21^\circ$, the shear layer once again grows in thickness, with velocity fluctuations in the range of, $11 \% \leq u'_{rms}/\bar{U}_\infty \leq 20 \%$ and $8 \% \leq v'_{rms}/\bar{U}_\infty \leq 14 \%$, and the turbulent shear stress ranges between -0.02 & -0.01. It should be mentioned that for $\alpha = 21^\circ$, the shear layer is thicker, with larger regions of higher fluctuations as compared to the $\alpha = 20^\circ$ case.

It is also noted that for the cases where $\alpha \geq 20^\circ$, at $z/b = 0.46$, high levels of velocity fluctuation were observed in the wake of the wing-tip vortex, resulting in high levels of turbulent shear stress. Results from the 3-component setup did validate the presence of these high velocity fluctuations in the vicinity of the tip-vortex core, with some discrepancies in the magnitudes of the fluctuations. These discrepancies were not surprising, since the flow in this region is so highly three-dimensional; the percentage of estimated vectors in the 2-component PIV results for this region is also large, thus reducing the reliability of these results.

For the $\alpha = 15^\circ, 18^\circ, 21^\circ$ & 25° cases, 3-component velocity data was also collected at various chord-wise locations. These results validated the data from the 2-component PIV setup with regard to the boundaries of the separation layer over the wing and fluctuating velocity levels within the reflex of the airfoil. For instance, the 2-component setup indicated that the top of the separation region was ~ 12 mm from the surface of the wing at $x/c = 0.8$ and at $\alpha = 15^\circ$. The 3-component results for the same case, besides showing that the top of the separation layer was ~ 12 mm from the wing surface, also showed that the velocity fluctuations in the stream-wise component of the flow were in the range of $0.8 - 0.14\bar{U}_\infty$ (higher fluctuation levels being on the inner portion of the shear layer), which is very close to the results indicated by the 2-component setup in the same region (Figure 3-21).

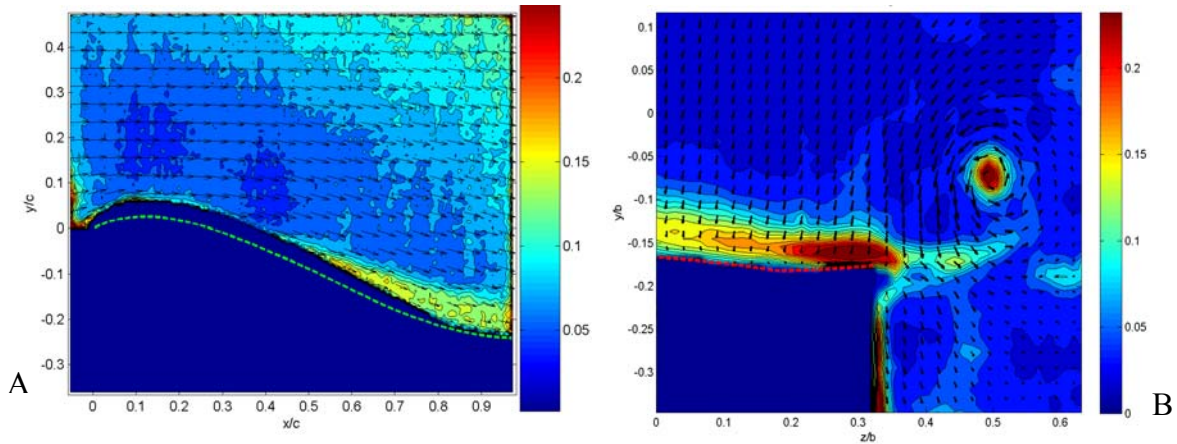


Figure 3-21. Comparison of the normalized stream-wise turbulence levels at $\alpha = 15^\circ$, $x/c = 0.8$ and $z/b = 0$, obtained from, A) the 2-component and B) the 3-component PIV setups.

The results from the 3-component PIV experiments also indicate that the strongest velocity fluctuations are in the stream-wise and span-wise components in the separated shear layer in the flow over the wing, where $0.25 < z/b < 0.5$. These results seem intuitively correct, since this is the region most affected by the downwash over the airfoil as well as the vortex developing off the wing-tip. It is also observed that as soon as the flow passes over the TE of the wing, the velocity fluctuation levels in the wake, drop to much lower levels ($0.1 - 0.15 \bar{U}_\infty$), as compared to within the flow over the wing ($\sim 0.25 \bar{U}_\infty$). In addition, the 3-component PIV results indicate that the fluctuating velocity levels in the core of the vortex decrease as the flow progresses downstream of the leading edge. It is also observed that the fluctuations closer to the perimeter of the wing, persist at higher levels further downstream than the fluctuations at other locations around the wing, as can be seen in Figure 3-22C.

While the 2-component data did not clearly indicate where exactly separation was taking place over the wing for $\alpha = 15^\circ$, the 3-component results show that it might be close to $x/c = 0.5$. The data at $x/c = 0.3$ for this angle of attack shows fluctuation levels $< .15 \bar{U}_\infty$, in the regions closest to the wing (< 2.6 mm from the surface). However, at $x/c = 0.4$, the stream-wise cross

section of the shear layer grows to almost 4 mm in thickness and the fluctuation levels are significantly higher ($\sim 0.25\bar{U}_\infty$). Interestingly, the thickness of the shear layer over the wing changes little between $x/c = 0.4$ and $x/c = 0.5$ and shows indications of growth where $x/c \geq 0.6$, thus validating the statements made earlier about the flow characteristics in the same region.

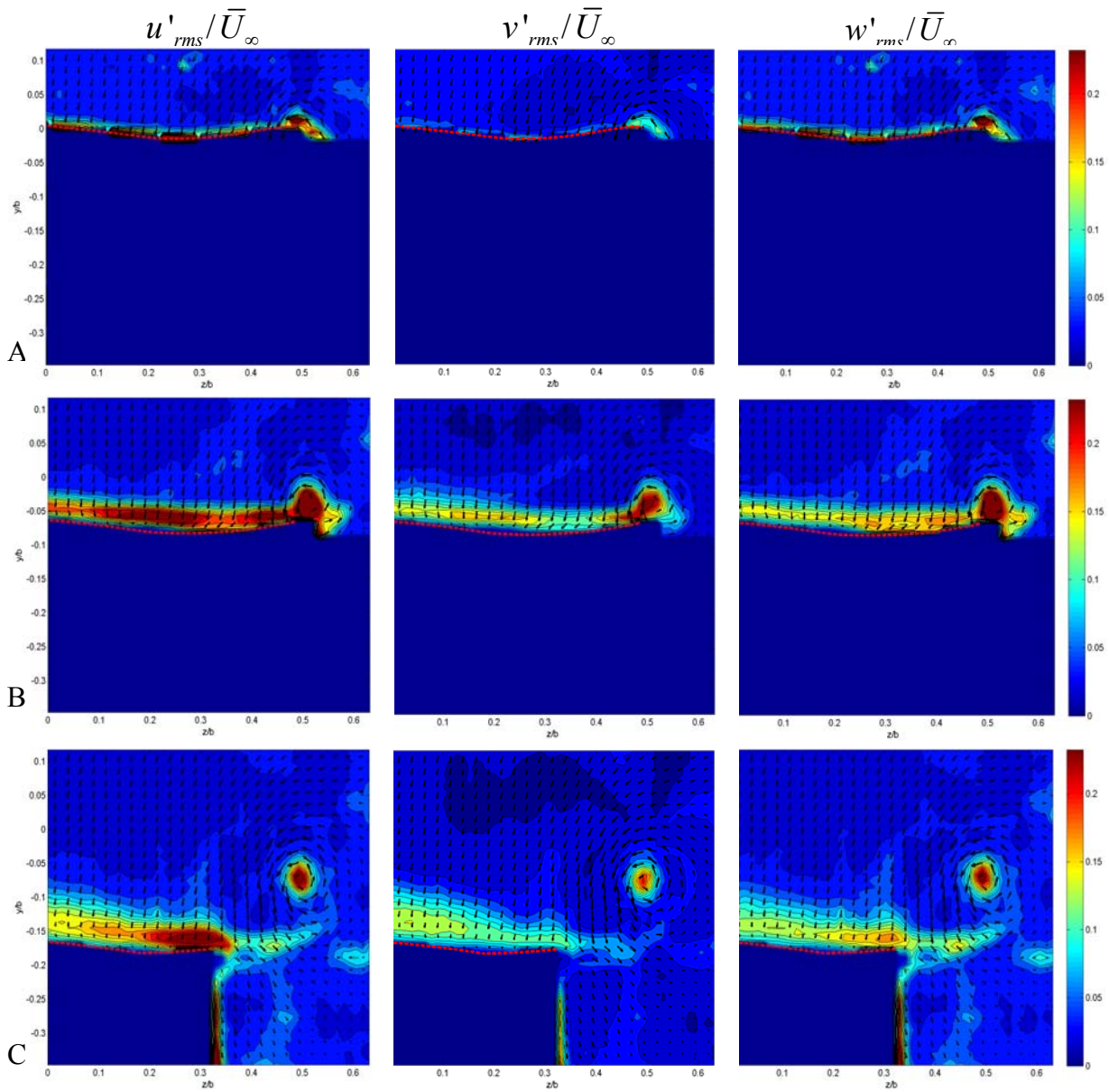


Figure 3-22. Flow field distribution of the normalized velocity fluctuation levels u'_{rms}/\bar{U}_∞ (left), v'_{rms}/\bar{U}_∞ (center) & w'_{rms}/\bar{U}_∞ (right); at A) $x/c = 0.3$, B) $x/c = 0.5$ and C) $x/c = 0.8$, at $\alpha = 15^\circ$.

The chord-wise plots for $\alpha = 18^\circ$ show fluctuating velocity levels that are similar to the $\alpha = 15^\circ$ case. At $x/c = 0.3$, there is a small region that extends over the span of the wing and sits just above the wing surface, ~ 3 mm thick, with relatively large fluctuating velocities in u & w ($\sim 0.25 \bar{U}_\infty$). At $x/c = 0.4$, the turbulent layer grows to ~ 4.5 mm in thickness, with fluctuations still being strongest in u & w . It should be assumed that the separation layer also has some level of velocity fluctuation associated with it, but this is not clearly visible at this stage. In the mean time, the fluctuations in the core of the wing-tip vortex have also maintained similar levels. By the time $x/c = 0.6$, the top of the shear layer over the wing has grown to ~ 8 mm in thickness and the highest fluctuations are now in u ($\sim 0.25 \bar{U}_\infty$), while the fluctuating levels in v & w become lower ($\sim 0.15 \bar{U}_\infty$). A thin region is also seen in between the wing surface and the shear layer (for $0.5 \leq x/c \leq 0.7$), that has very low levels of fluctuating velocities associated with it; this region is probably part of the separation layer that develops over the wing. The fluctuation levels in this separation layer range from being fairly strong at $x/c = 0.3$, where the region is very thin, to less than $0.1 \bar{U}_\infty$ at $x/c = 0.7$, where the shear layer and separation layer are the thickest. As was previously noted for $\alpha = 15^\circ$, the shear layer does not grow thicker between $x/c = 0.6$ and $x/c = 0.8$, after which it actually shrinks in size to ~ 4.5 mm at $x/c = 0.9$, just before the flow leaves the trailing edge of the wing.

In the wake of the airfoil at $\alpha = 18^\circ$ and at $x/c = 1.0$, there is a distinct region (~ 20 mm thick) that surrounds the vortex core where there is very little fluctuation in the circulating flow, Figure 3-23. At the outer perimeter of this region, there are signs of the circulation from the tip vortex interacting with the separation layer coming off the wing. However, at $x/c = 1.1$, the fluctuation levels in u & w grows considerably in the wake of the airfoil and in two other regions, around $y/b = 0.15$ & 0.25 . At $x/c = 1.2$, the fluctuations in the wake of the airfoil are

nearly non-existent, but the regions of high velocity fluctuations near the vortex core are still very strong in u & w (Figure 3-24). By the time the flow reaches $x/c = 1.4$, the fluctuations in all three components are at much lower levels and are confined to regions within the tip vortex.

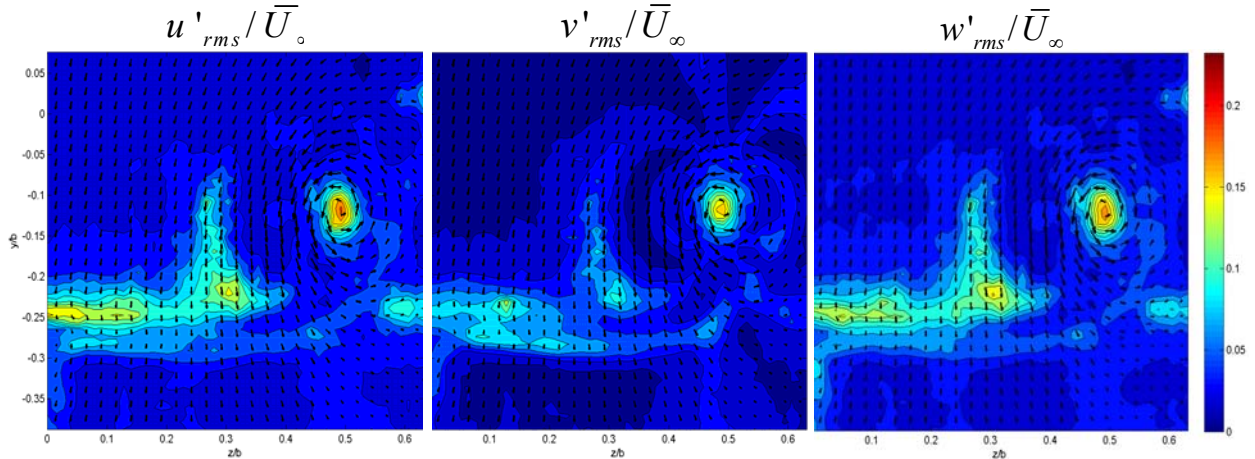


Figure 3-23. Normalized fluctuating velocity levels in the flow field at $\alpha = 18^\circ$ and $x/c = 1.0$.

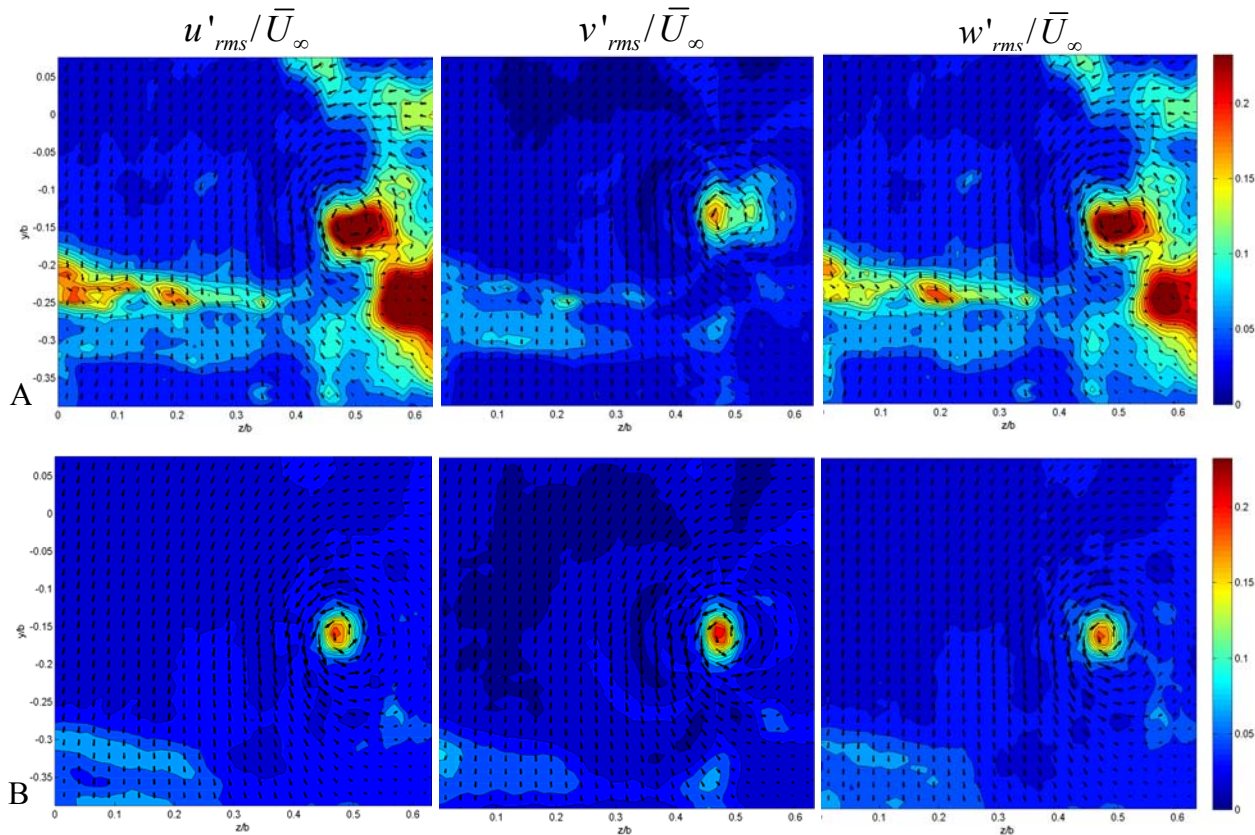


Figure 3-24. Normalized fluctuating velocity levels in the flow field at $\alpha = 18^\circ$; A) $x/c = 1.1$ and B) $x/c = 1.4$; u'_{rms}/\bar{U}_∞ (left), v'_{rms}/\bar{U}_∞ (center) & w'_{rms}/\bar{U}_∞ (right).

Measurements at $\alpha = 21^\circ$ and $x/c = 0.3$ showed the presence of a layer ~ 4 mm thick, above the span of the airfoil, where the higher fluctuation levels were in u & w ($\sim 0.25 \bar{U}_\infty$), and where the fluctuation levels in v did not exceed $0.15 \bar{U}_\infty$. by the time the flow reaches $x/c = 0.4$, the top of the shear layer grows to ~ 8 mm in thickness and turbulence levels in the stream-wise direction continue to remain high, whereas the turbulence levels in v & w drop steadily as the flow moves downstream.

For the case where $\alpha = 21^\circ$, the fluctuation levels in the visible part of the separation layer are less than $0.05 \bar{U}_\infty$. The separated shear layer (with higher levels of velocity fluctuations), actually sits ~ 4 mm above the surface of the wing between $0.5 \leq x/c \leq 0.7$, downstream of which, the separation layer thins out, until finally, the flow appears to reattach to the surface of the wing at $x/c \sim 0.9$. After $x/c = 0.8$, the fluctuation levels in all three components of the velocity start to drop; at $x/c = 1.0$, fluctuations are less than 15% of the free-stream velocity. However, similar to the $\alpha = 18^\circ$ case, at $x/c = 1.1$, the fluctuation levels in u & w suddenly strengthen to $\sim 20\%$ of \bar{U}_∞ , after which the fluctuating velocity levels in all three components drops to less than 5% of \bar{U}_∞ . Also similar to the $\alpha = 18^\circ$ case, at $x/c = 1.1, 1.2$ & 1.4 , there is a region with high levels of fluctuations in u & w that appears to the bottom right of the wing-tip vortex. It is uncertain what this region represents.

At $\alpha = 25^\circ$, the fluctuating velocity levels in the separated region behind the airfoil are in the range of 15-33% of the free-stream velocity for both the components of the flow. Between $0.3 \leq x/c \leq 0.5$, the velocity fluctuations are higher in u & w . However, for measurements taken at $x/c \geq 0.6$, the fluctuation levels grow higher in u & v ($\sim 0.25 \bar{U}_\infty$), but remain below $0.15 \bar{U}_\infty$.

for w . As the re-circulating component of the flow becomes stronger, the fluctuations in the vertical component of the flow begin to grow larger in that region.

For $\alpha = 25^\circ$, Figure 3-25 contains plots that depict that development of the fluctuating velocity profiles for the three components of the flow. As the flow moves downstream over the wing from $x/c = 0.4$ to $x/c = 0.8$, there is an increase in the velocity fluctuations in v , while there is a simultaneous decrease in the fluctuation levels in w .

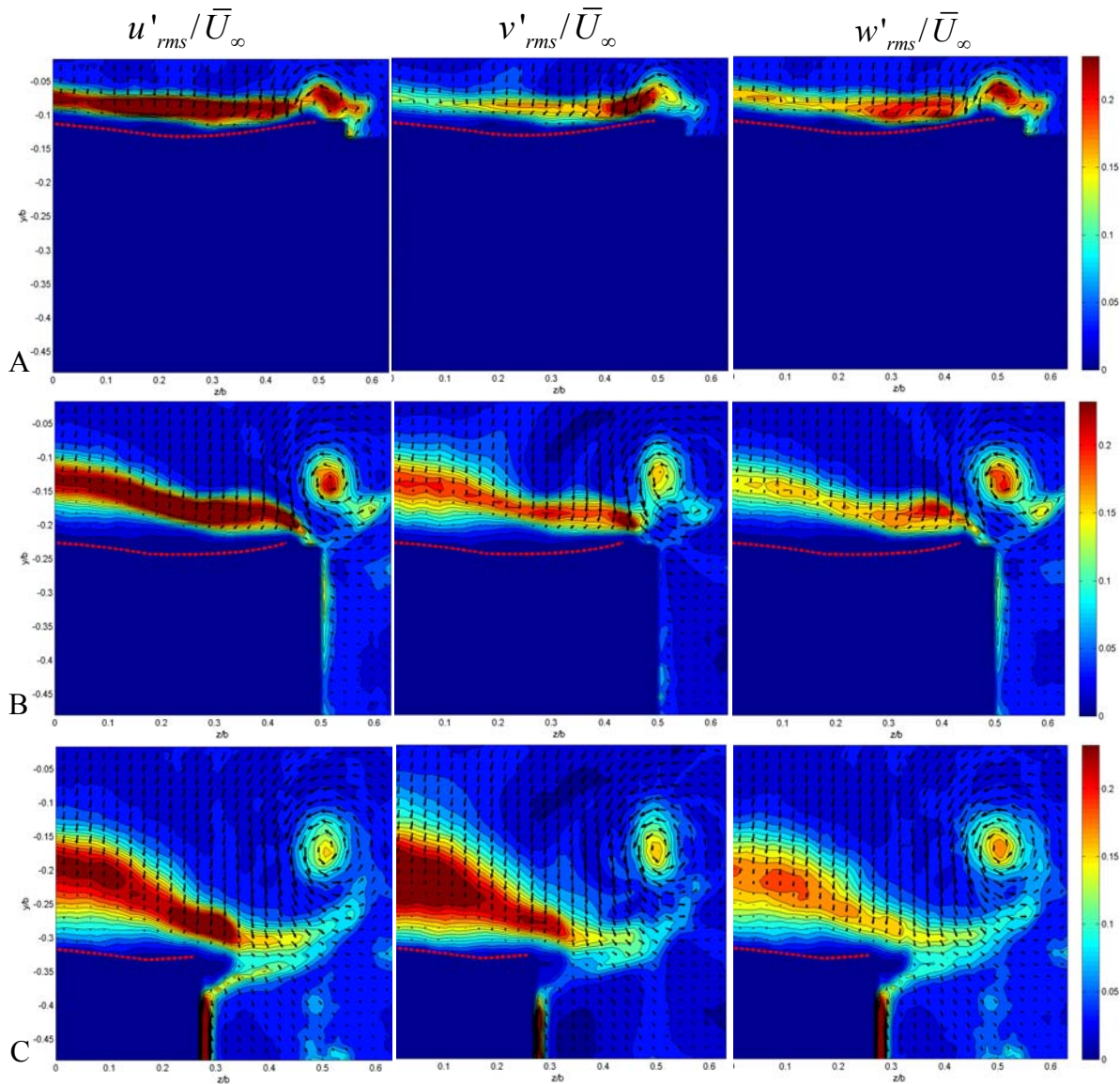


Figure 3-25. Development of the normalized fluctuating velocity profiles in u (left), v (center) & w (right), at $\alpha = 25^\circ$; A) $x/c = 0.4$, B) $x/c = 0.6$ and at C) $x/c = 0.8$.

For $x/c > 0.9$, it is noted that the faster flow from the underside of the wing interacts with the slower flow from above the wing, creating another region of high fluctuation levels beneath the trailing edge. This region soon combines with the separation layer from the flow over the wing and loses intensity in u & w by the time the flow reaches $x/c = 1.4$ (fluctuations are $< 0.12\bar{U}_\infty$). However, the measurements at $x/c = 1.4$ show that the turbulence levels in the vertical component of the velocity persist at relatively higher levels ($v' \sim 0.22\bar{U}_\infty$).

At such a high angle of attack, there is a large amount of interaction between the flow over the wing and the circulatory flow induced by the wing-tip vortex. It appears as though the wing-tip vortex is strong enough to entrain part of the flow over the wing into the outer regions of the vortex. This might explain the slight upward curve in the stream-wise cross-sections of the turbulence in u , v & w , seen in Figure 3-25.

Velocity Correlation Analysis

Results from the spatial cross correlations that were performed on the fluctuating components of the normal and stream-wise components of the velocity data at $\alpha = 10^\circ$ and $z/b = 0.08$ are shown in Figure 3-26. It was observed that at $z/b \leq 0.17$, the average turbulent length scales within the shear layer were on the order of, $L_{TUx} \sim 7$ mm & $L_{TUy} \sim 5$ mm and $L_{TVx} \sim 7$ mm & $L_{TVy} \sim 12$ mm at $x/c = 0.6$. The subscripts U & V indicate which component of the flow the correlations have been performed on, and x & y indicate the axis of the measurement. Similarly, at $x/c = 0.8$, the turbulent length scales were $L_{TUx} \sim 22$ mm & $L_{TUy} \sim 10$ mm and $L_{TVx} \sim 11$ mm & $L_{TVy} \sim 19$ mm, indicating an increase in the turbulent length scales as the flow moved downstream of the point of separation. Interestingly, at $z/b = 0.46$, a strong correlation was also observed in the stream-wise component of the velocity measured close to the LE of the wing; in this case $L_{TUx} \sim 17$ mm & $L_{TUy} \sim 5$ mm and $L_{TVx} \sim 10$ mm & $L_{TVy} \sim 3$ mm. It should be noted

that the noise seen in the cross correlation plots (below and on the following pages), is on the order of ± 0.04 and may be attributed to error in the PIV measurements. Though the levels may appear to be rather noisy (± 0.1), this is just an artifact of the color levels used to depict the data.

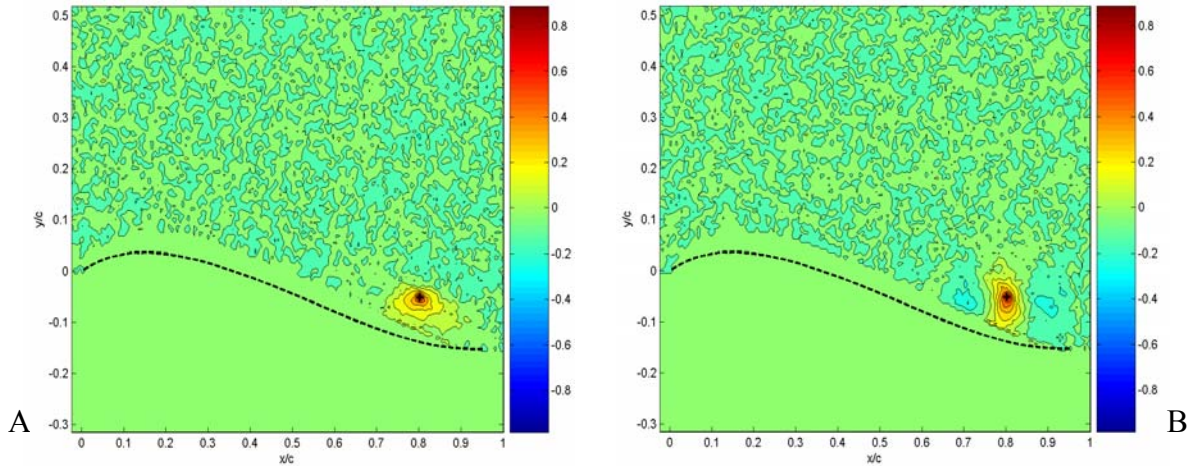


Figure 3-26. Spatial cross correlation performed on the fluctuating components of the flow at $\alpha = 10^\circ$ and $z/b = 0.08$. Cross-correlations in A) the stream-wise component and B) the normal component of the flow. Values for the correlation coefficient are between +1 & -1.

For $\alpha = 15^\circ$, the average turbulent length scale in the region of separation above the wing at $x/c = 0.6$ was $L_{TUx} \sim 6$ mm & $L_{TUy} \sim 7$ mm and $L_{TVx} \sim 8$ mm & $L_{TVy} \sim 12$ mm. Similar to the $\alpha = 10^\circ$ case, further downstream at $x/c = 0.8$, $L_{TUx} \sim 28$ mm & $L_{TUy} \sim 12$ mm and $L_{TVx} \sim 15$ mm & $L_{TVy} \sim 18$ mm.

The correlation on the 3-component PIV data validated the results for L_{TUx} , L_{TUy} , L_{TVx} & L_{TVy} that had been obtained from the 2-component PIV data. The cross correlation results from the 3-component PIV experiments also provided insight into the span-wise extent of the length scales. For instance, the average turbulent length scales in the region of the vortex core was almost identical in size to the structure identified by the stream-wise vorticity distribution at various chord-wise locations. Also, as the flow progressed downstream of the leading edge, the

cross correlations amongst the three components indicated a growing trend in the turbulent length scales.

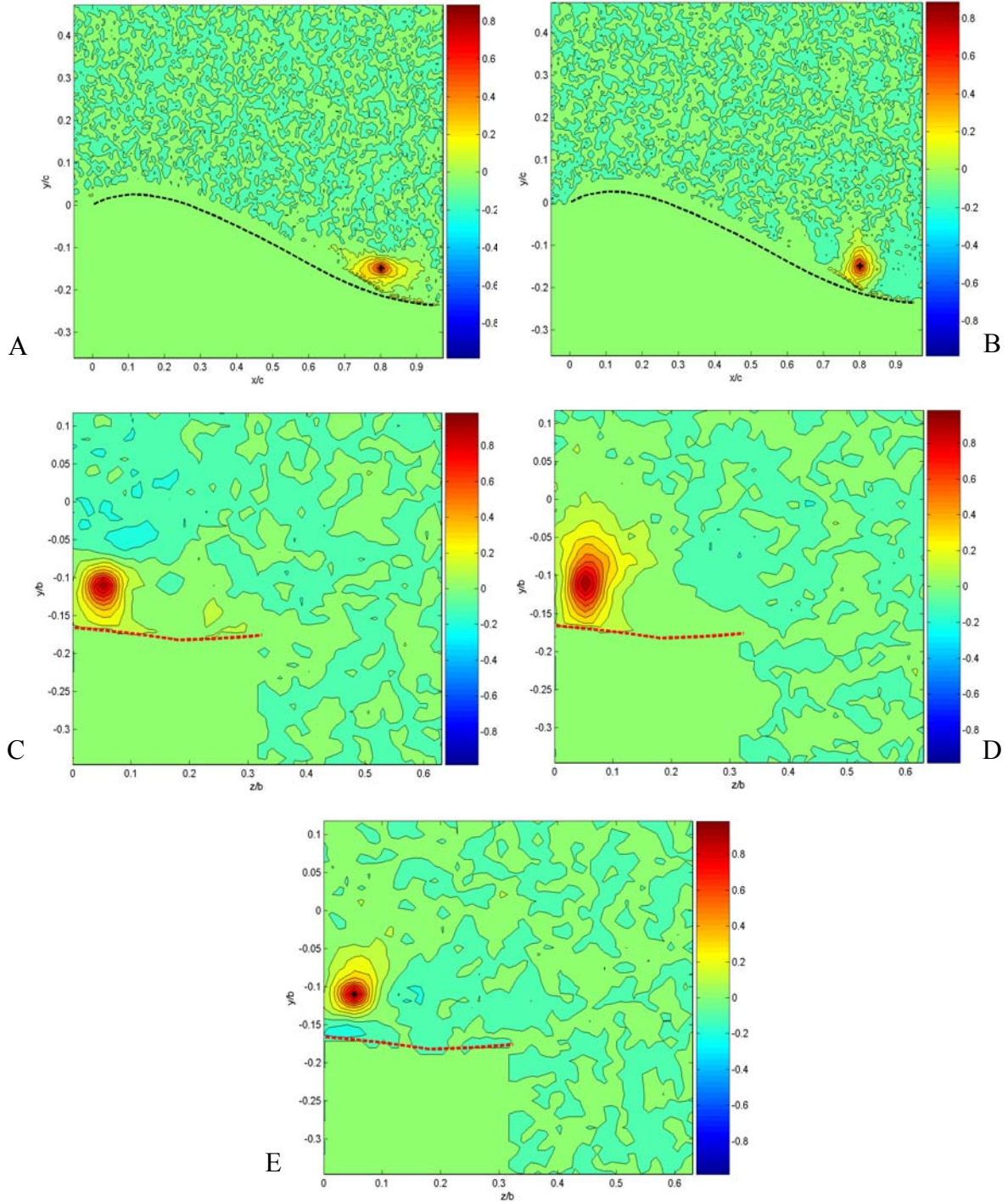


Figure 3-27. Spatial cross correlation in the fluctuating components of the flow at $\alpha = 15^\circ$; A) u' at $z/b = 0$, B) v' at $z/b = 0$, C) u' at $x/c = 0.8$, D) v' at $x/c = 0.8$, and E) w' at $x/c = 0.8$.

In fact, for $x/c \geq 0.4$, the fluctuating velocities in the shear layer were well correlated over the span of the wing for all three components of the flow. It was observed that out of the three components, the span-wise turbulent length scales were the smallest in this region. However, in the regions closest to the center of the wing-tip vortex, as it propagated downstream, the largest turbulent length scales were in the span-wise component of the velocity.

In the measurements where $x/c \geq 0.7$, the turbulent length scales for the stream-wise and span-wise components of velocity stopped growing larger, but L_{TV} was almost double the size of L_{TU} & L_{TW} . Measurements also indicated that once the flow completely passes over the wing, the turbulent length scales begin to shrink with each stream-wise measurement.

From the 2-component PIV results for $\alpha = 18^\circ$, $z/b = 0$ and $x/c = 0.8$, the spatial cross correlations in the fluctuating components of the flow in the shear layer above the airfoil, showed average turbulent length scales on the order of $L_{TUx} \sim 22$ mm, $L_{TUY} \sim 9$ mm, $L_{TVx} \sim 10$ mm & $L_{TVy} \sim 10$ mm. Spatial cross correlations in the fluctuating velocities from the 3-component PIV results showed that within the turbulent layer just above the wing, the stream-wise and vertical components of the velocity were well correlated, but the span-wise turbulence was limited to relatively small regions around the point of comparison, as seen in Figure 3-28. Similar to the previous case, at $x/c = 0.3$, the turbulent length scales in the shear layer were relatively small and confined to a region just outside the point of reference (on the order of the grid spacing, ~ 2 mm), but at $x/c = 0.4$, when the turbulent region is observed to grow to almost 4.5 mm in thickness, the fluctuating components in u & v were well correlated across the span of the wing. The turbulence in w showed smaller length scales, but also indicated a region of positive correlation over the dihedral of the wing and immediately below it, a region of negative

correlation (Figure 3-29). These regions are related to the span-wise re-circulation phenomenon that has been discussed earlier.

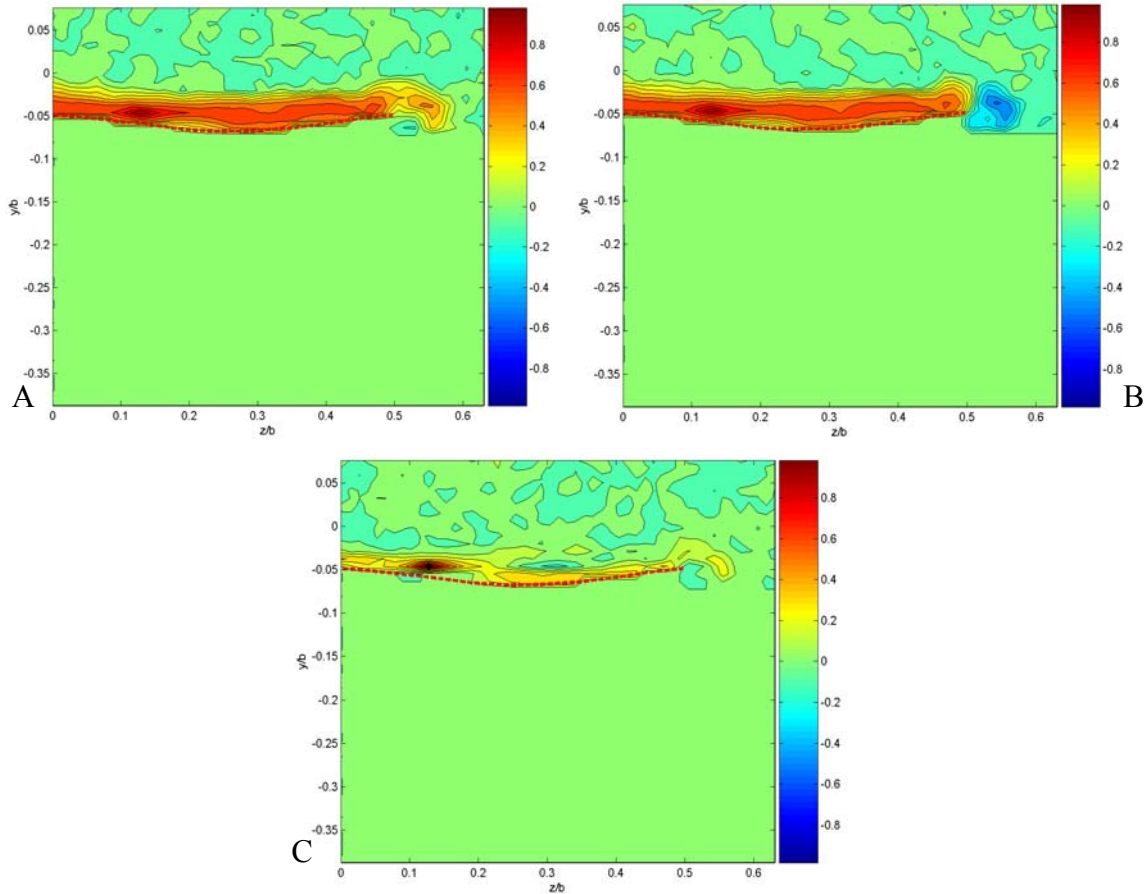


Figure 3-28. From measurements at $\alpha = 18^\circ$ & $x/c = 0.4$, spatial cross-correlations in:
A) u'_{rms}/\bar{U}_∞ , B) v'_{rms}/\bar{U}_∞ , and C) w'_{rms}/\bar{U}_∞ .

As was described for the velocity fluctuation levels in the wake of the wing at $\alpha = 18^\circ$, the turbulent length scales just aft of the wing at $x/c = 1.0$ are limited to the region just around the point of reference. However, at $x/c = 1.1$, the turbulent length scales in the wake of the airfoil suddenly grow larger in the region just behind the trailing edge of the wing. Also, just as there was some turbulence observed near the tip vortex center (Figure 3-24 A), the turbulent length scales in the same region are considerably large and correlate well with the size of the region indicated earlier by the distribution of the fluctuating velocities in u & w . On the other hand, the

turbulent length scales in v were smaller than those for the other two components of the flow in the same region, as is shown in Figure 3-30.

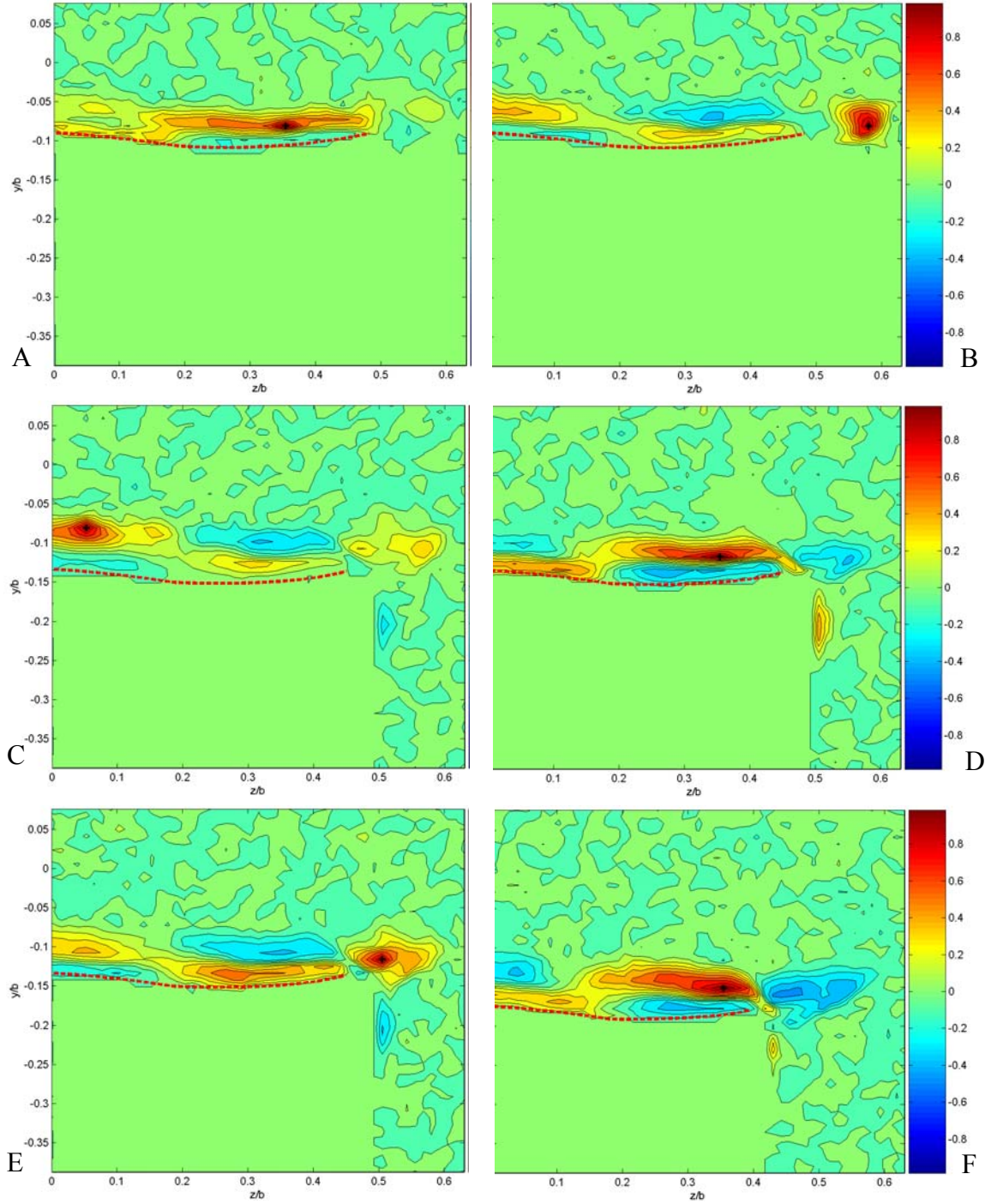


Figure 3-29. Spatial cross correlations in the fluctuating span-wise component of the flow $(w'_{rms}/\bar{U}_\infty)$ at $\alpha = 18^\circ$; $x/c = 0.5$ (A & B), $x/c = 0.6$ (C, D & E) and $x/c = 0.7$ (F).

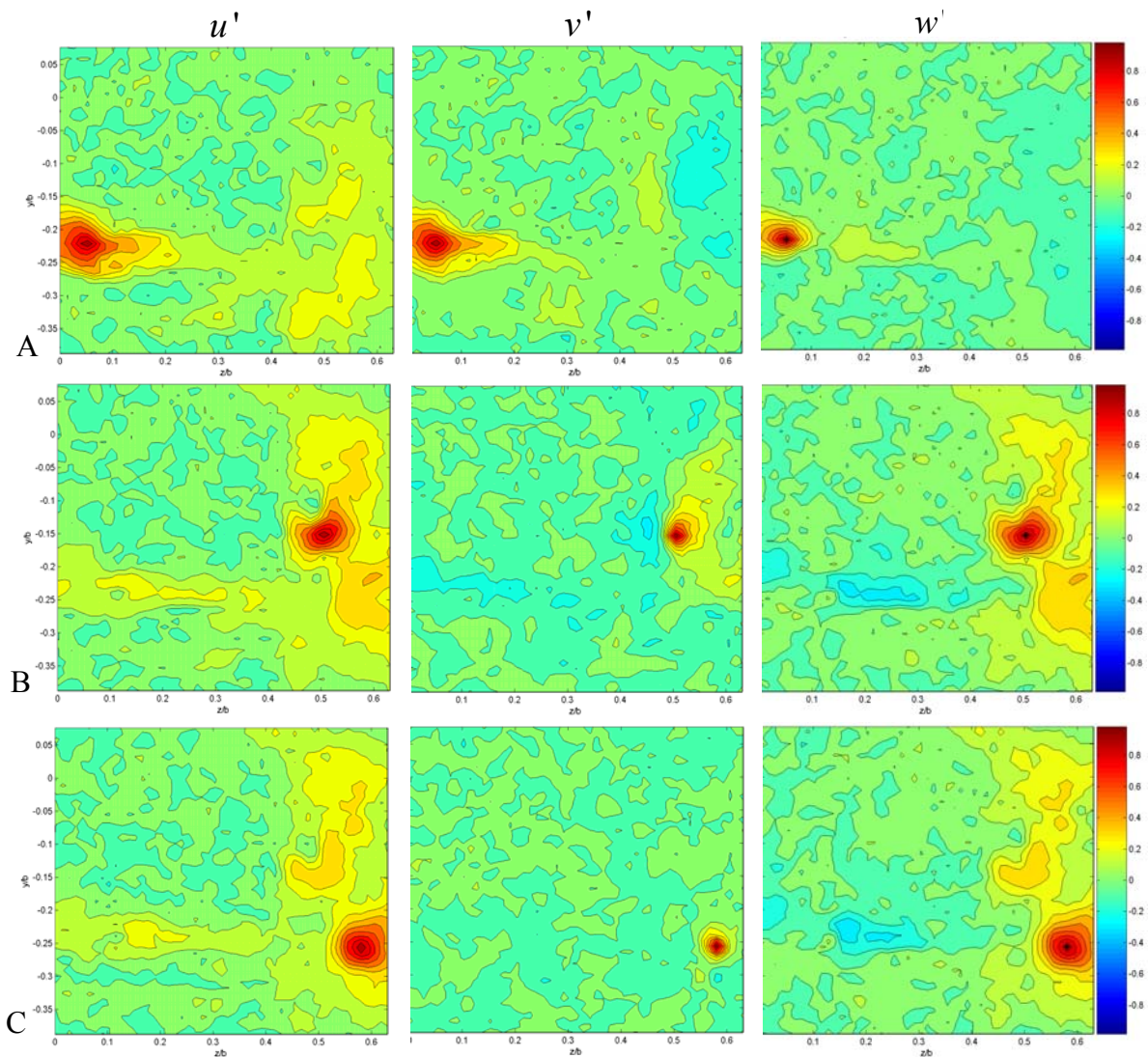


Figure 3-30. Spatial cross correlations in the fluctuating components of the flow at $\alpha = 18^\circ$ (compare with Figure 3-24A); u' (left), v' (center) & w' (right), at $x/c = 1.1$ and A) $z/b = 0.05$ & $y/b = -0.225$, B) $z/b = 0.5$ & $y/b = -0.05$ and C) $z/b = 0.06$ & $y/b = -0.25$.

Now the measurements at $x/c = 1.2$ showed relatively small turbulent length scales in the wake of the airfoil, but continued to indicate large regions of the turbulence near the wing-tip vortex that had propagated downstream. Finally, the measurements at $x/c = 1.4$ showed little indication of turbulence in the flow except in the center of the tip-vortex.

For $\alpha = 20^\circ$, the results from the spatial cross correlation performed on the fluctuating components of the velocity, indicated that the average turbulent length scales in the shear layer at $x/c = 0.6$ were $L_{TUx} \sim 16$ mm, $L_{TUy} \sim 10$ mm, $L_{TVx} \sim 8$ mm & $L_{TVy} \sim 10$ mm and at $x/c = 0.8$ were $L_{TUx} \sim 32$ mm, $L_{TUy} \sim 11$ mm, $L_{TVx} \sim 18$ mm & $L_{TVy} \sim 15$ mm.

For $\alpha = 21^\circ$, spatial cross correlations in the separation region in the 2-component PIV data showed that the average turbulent length scales were, $L_{TUx} \sim 44$ mm & $L_{TUy} \sim 12$ mm and $L_{TVx} \sim 16$ mm & $L_{TVy} \sim 12$ mm, at $x/c = 0.8$ and $z/b = 0$. Results from the 3-component PIV setup at $x/c = 0.4$, showed that the turbulent length scales in the region closest to the wing were on the order of L_{TUz} & $L_{TWz} \sim 8$ mm & L_{TUy} , L_{TVy} & $L_{TWy} \sim 3$ mm, where L_{TVz} spanned the top surface of the wing. However, within the shear layer at $x/c \geq 0.4$, the reference points begin to show a strong correlation with the large velocity fluctuations taking place in that region, similar to that in the $\alpha = 18^\circ$ case, (see Figure 3-28). The cross correlation results also corroborate the results that indicate a weakening of the turbulence levels at $x/c = 1.0$ through shrinking of the turbulent length scales, and then an unexpected strengthening of the turbulence levels at $x/c = 1.1$, with an increase in the average turbulent length scale in the region. The presence of a sizeable region with high levels of velocity fluctuations is also observed at the bottom right of the tip vortex at $1.1 \leq x/c \leq 1.4$ (similar to Figure 3-24 & Figure 3-30), and is verified by the results of the cross correlation.

For $\alpha = 25^\circ$, the distribution of the cross-correlation coefficients in the flow field, indicates that for u & v , there is always good correlation between the reference point and the rest of the data within the turbulent shear layer (as was previously noted for $\alpha = 18^\circ$ and $\alpha = 21^\circ$, Figure 3-28), whereas w tends to indicate much smaller turbulent length scales in the same region; similar to the results in Figure 3-29.

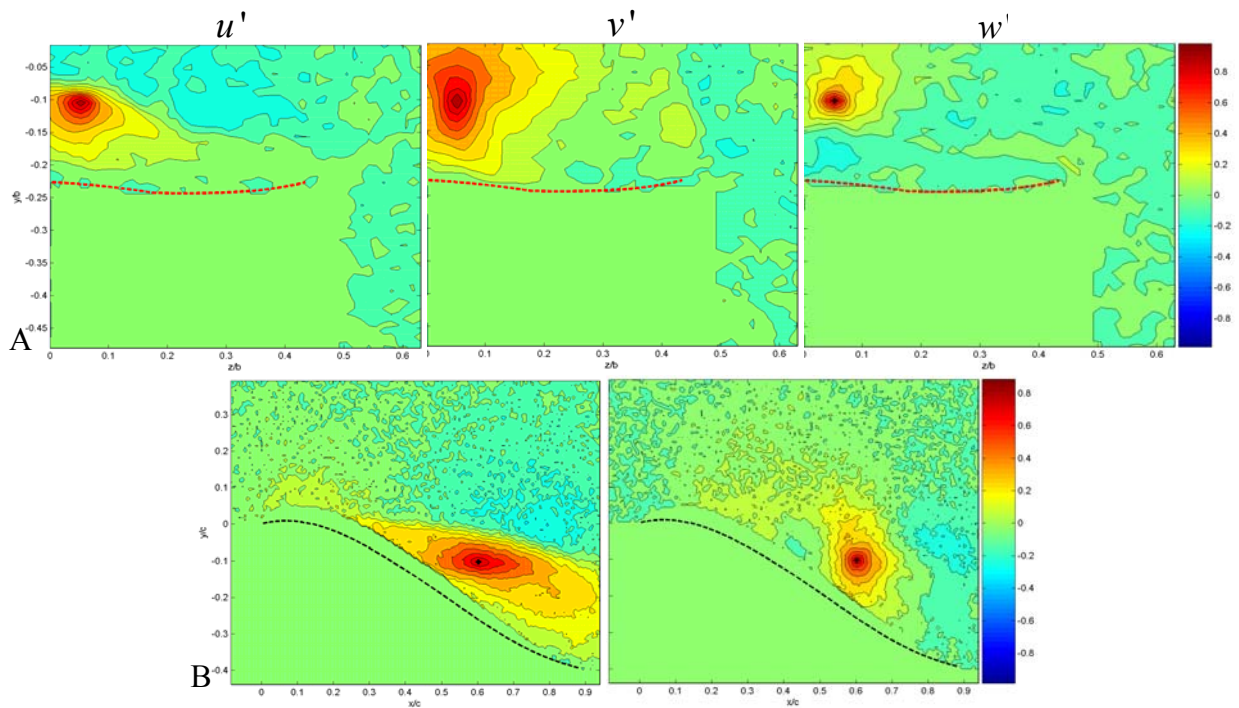


Figure 3-31. Spatial cross correlations at $\alpha = 25^\circ$, at $x/c = 0.6$ and $z/b = 0.08$; A) u' (left), v' (center) & w' (right), and in B) u' (left) & v' (right).

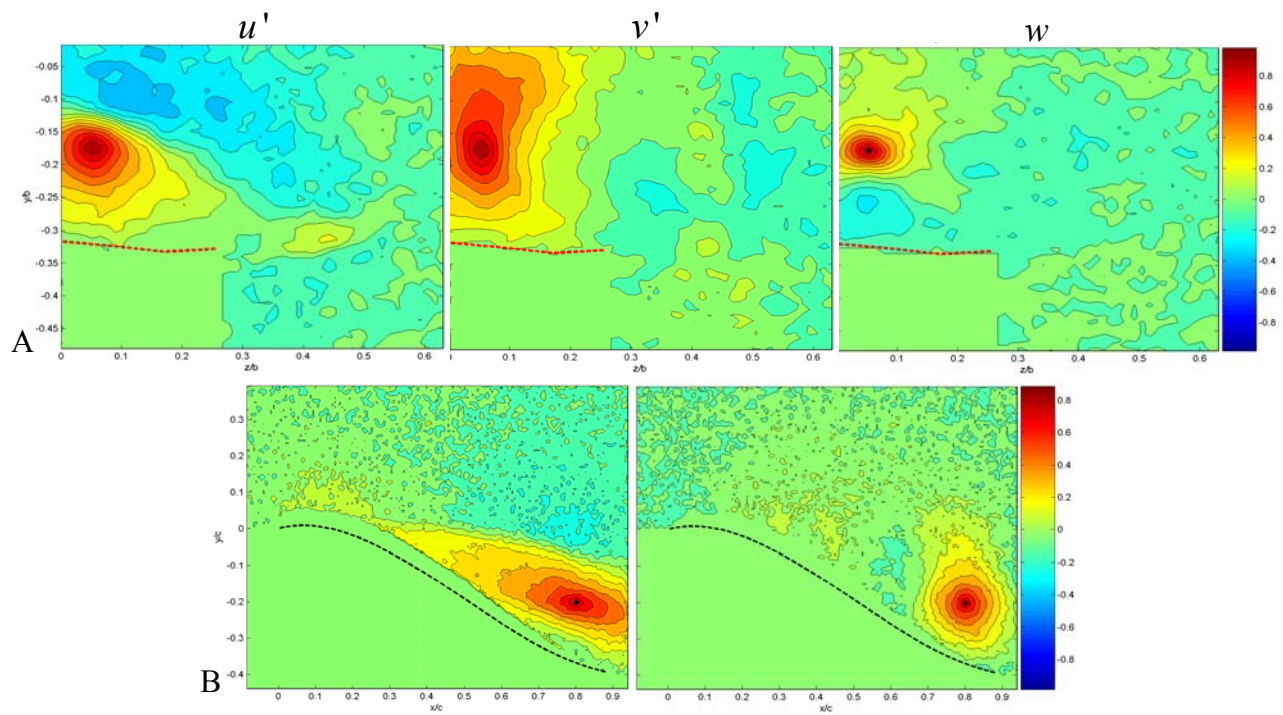


Figure 3-32. Spatial cross correlations at $\alpha = 25^\circ$, at $x/c = 0.8$ and $z/b = 0.08$; A) u' (left), v' (center) & w' (right), and in B) u' (left) & v' (right).

Within the separation layer just below the separated shear layer, at $x/c = 0.5$ and $z/b = 0$, the average turbulent length scales were L_{TUz} , L_{TVz} & $L_{TWz} \sim 12$ mm whereas $L_{TUy} \sim 4$ mm, $L_{TVy} \sim 8$ mm & $L_{TWy} \sim 6$ mm. Comparisons were also made to validate the turbulent length scale values obtained at similar locations in the flow for 2-component and 3-component PIV. Figure 3-31 shows comparisons between the cross-correlations at $x/c = 0.6$ and $z/b = 0.08$, $L_{TUx} \sim 80$ mm, $L_{TVx} \sim 25$ mm, $L_{TUz} \sim 42$ mm, $L_{TVz} \sim 50$ mm & $L_{TWz} \sim 19$ mm whereas $L_{TUy} \sim 18$ mm, $L_{TVy} \sim 40$ mm & $L_{TWy} \sim 14$ mm. Figure 3-32 shows similar plots for $x/c = 0.8$, and $z/b = 0.08$, which clearly show the increase in the turbulent length scales as the flow moves downstream. Figure 3-33 contains plots of the spatial cross correlation for reference points that; A) lie close to the upper boundaries of the separated shear layer, and B) lie within the region of re-circulating flow. Case A, lies within a region of high fluctuating velocities, for both components of the flow, and it may be observed that the contours in Figure 3-33A lie along a region that sits within the separated shear layer in the flow over the airfoil. It has been observed, from the results of numerous cross correlations, that the fluctuating velocities within the shear layer over the airfoil are often, well correlated.

This same trend was earlier observed in the results from the 3-component PIV data and was shown earlier in Figure 3-28. Figure 3-33B is in a region of relatively lower levels of fluctuation ($\sim 0.15\bar{U}_\infty$), within the flow that is re-circulating from the trailing edge of the airfoil to the leading edge. The turbulent length scales in the second case are clearly smaller. This may be attributed to the fact that the reference point in Case B is in an area where there are gradients in the fluctuating velocity levels of both components (10-15% of \bar{U}_∞); this in turn might lead to poor correlation between points that lie across such regions.

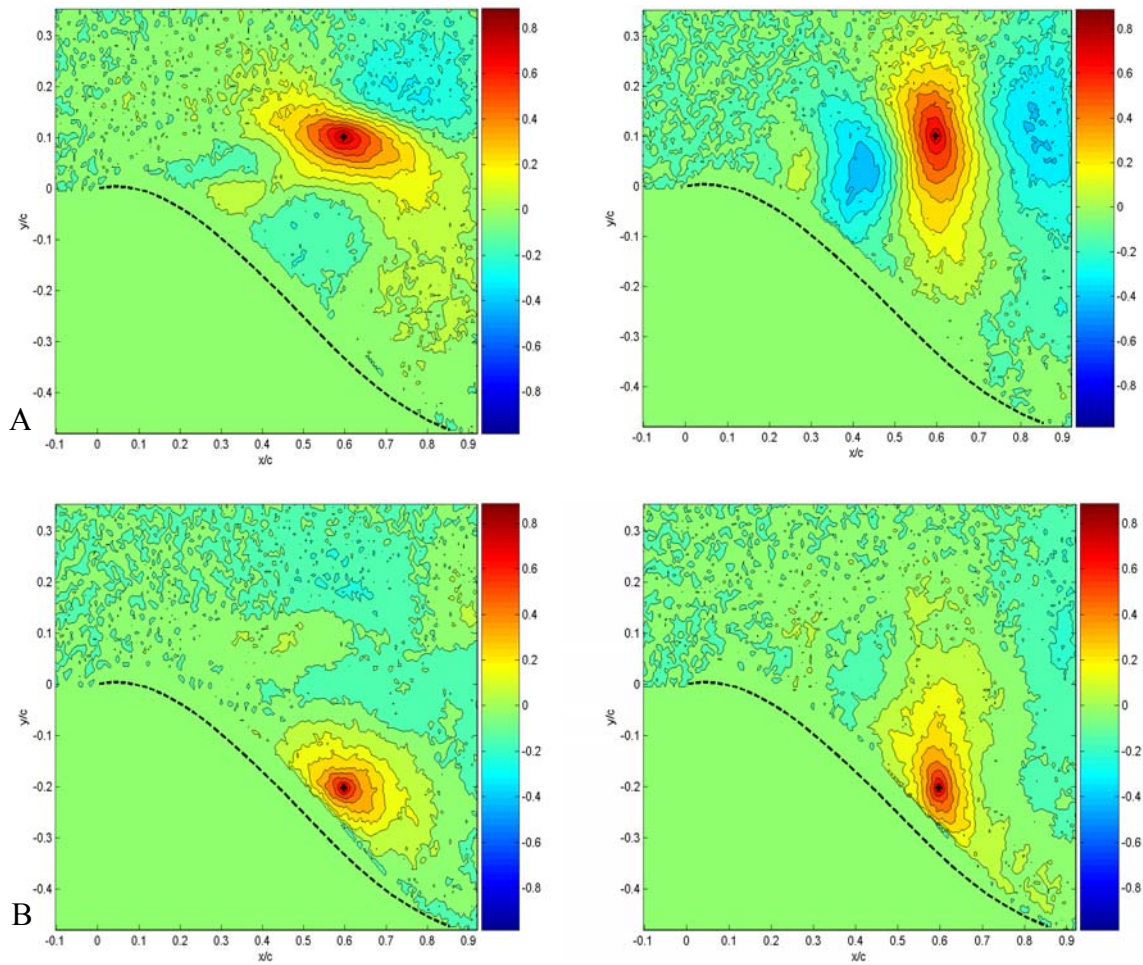


Figure 3-33. Spatial cross correlations in the stream-wise (left) and the normal (right) components of the flow, at $\alpha = 30^\circ$, $x/c = 0.6$ and at: A) $y/c = 0.1$ and B) $y/c = -0.2$.

For $\alpha = 30^\circ$, the spatial cross correlations performed on the 2-component PIV data indicated larger turbulent length scales than any of the previous cases. Figure 3-34 contains a series of plots where the point of reference for the cross correlations in u & v was moved along $z/b = 0$ and $y/c = 0.05$. All four reference points lie well within the separated flow behind the wing and as expected, the turbulent length scales increase in size as the flow moves further downstream of the point of separation.

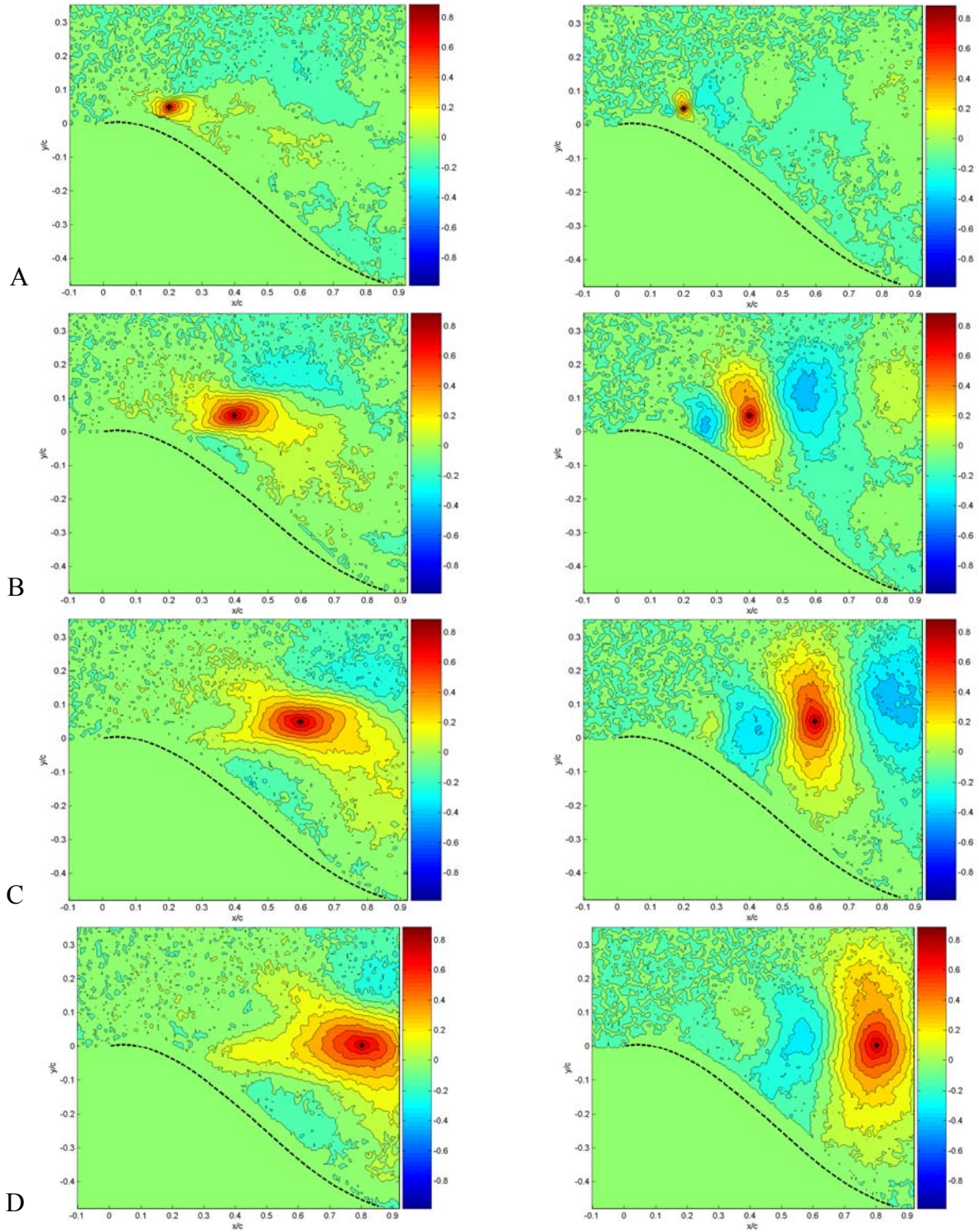


Figure 3-34. Spatial cross correlations in the stream-wise (left) and normal (right) components of the flow at $\alpha = 30^\circ$, $y/c = 0.05$ & $z/b = 0$ and at: A) $x/c = 0.2$, B) $x/c = 0.4$, C) $x/c = 0.6$ and D) $x/c = 0.8$.

Vorticity Calculations

Based on the results obtained for the stream-wise and normal components of the flow from the 2 & 3-component PIV measurements and the grid spacing that was used to calculate these results, the out of plane vorticity was computed using equations 3-1 & 3-2. Figure 3-35 is a compilation of graphs of the span-wise vorticity at various angles of attack and at $z/b = 0$ (from 2-component PIV data). The plots show that the vorticity levels within the shear layer over the airfoil, are weakest in the upper region (closest to the free-stream), and are strongest around the center regions of the shear layer at $z/b = 0$ (a similar gradient was observed for the turbulent shear stress levels in the region). As the shear layer thickens over the wing, the vorticity levels also appear to increase between $10^\circ \leq \alpha \leq 15^\circ$. However, at $\alpha = 18^\circ$, there is a reduction in the thickness of the shear layer and a subsequent decrease in the vorticity levels in that region.

Thereafter, between $20^\circ \leq \alpha \leq 21^\circ$, there is once again, a marked increase in the thickness of the shear layer followed by an increase in the span-wise vorticity. Finally, at $\alpha = 25^\circ$, the flow above the airfoil separates, leaving below it a region of re-circulating flow (clockwise-from trailing edge to leading edge), with relatively high levels of negative vorticity. In the massively separated case at $\alpha = 30^\circ$, it is observed that the strongest levels of span-wise vorticity are in the region where separation of flow is thought to occur over the wing. When examining the plots in Figure 3-2 & Figure 3-3, as expected, this same region also contains the highest gradients in the stream-wise and normal components of the flow at $z/b = 0$. As was previously mentioned, with the 2-component PIV setup used for these measurements, it was not possible to characterize the flow very close to the surface of the wing. However, the 3-component PIV setup did reveal some useful information regarding stream-wise vorticity that was being generated over the wing by a span-wise circulation of flow. This span-wise circulation happens to be a direct consequence of the circulatory flow induced by the strong wing-tip vortices in the region.

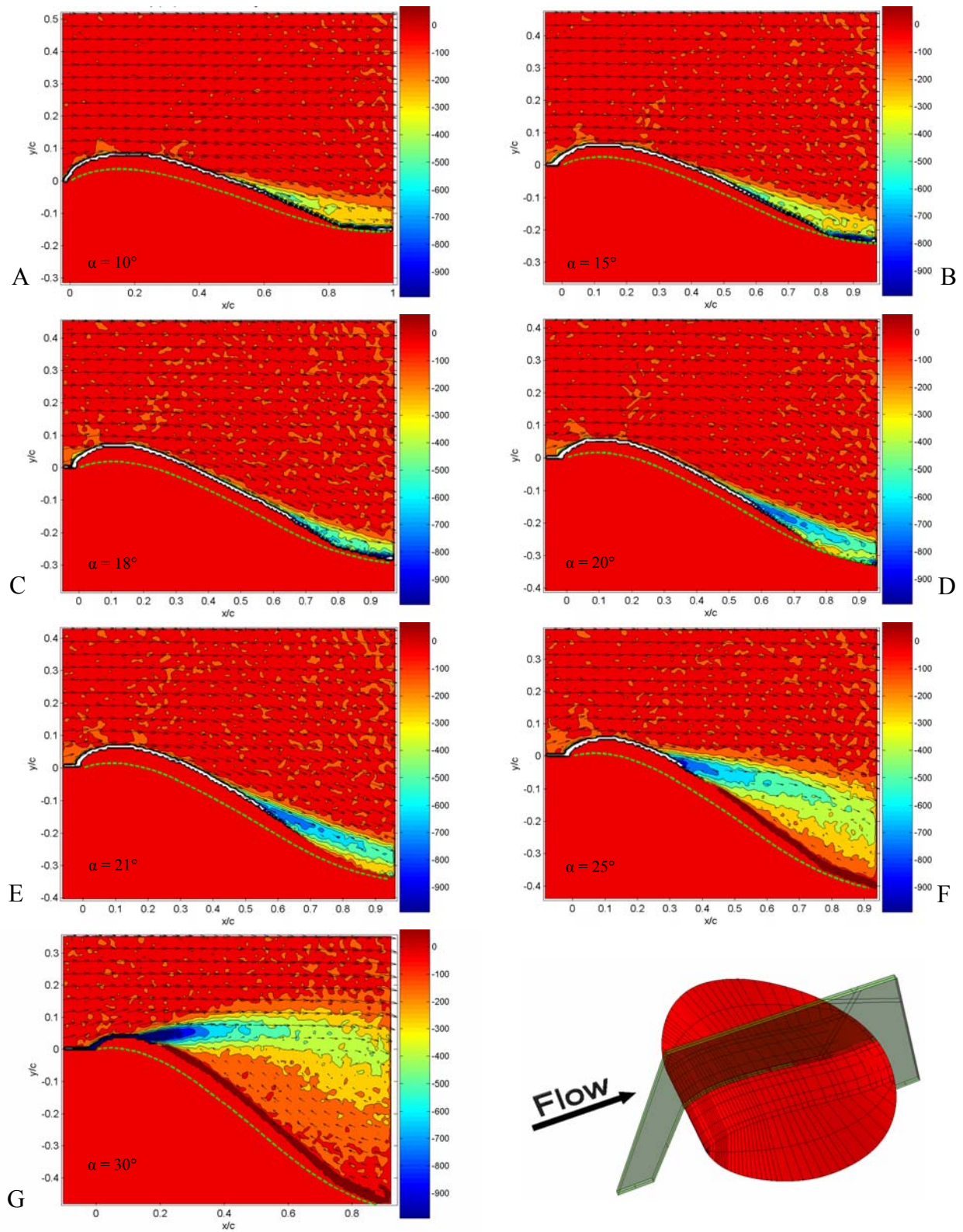


Figure 3-35. Span-wise vorticity, ω_z (s^{-1}), at various angles of attack ($z/b = 0$); A) 10° , B) 15° C) 18° , D) 20° , E) 21° , F) 25° and G) 30° .

For all the cases, 2-component PIV results showed that small pockets with high levels of span-wise vorticity were developing at the leading edge of the airfoil in the region close to the wing-tip. At first, this phenomenon is observed at $\alpha = 10^\circ$ and at $z/b = 0.46$, then it is observed at $\alpha = 15^\circ$ and $z/b = 0.46$ & 0.42 and again at $\alpha \geq 20^\circ$ and as far in as $z/b = 0.38$. As the angle of attack increases, these regions with high levels of vorticity are seen developing further in towards the root of the airfoil. At these span-wise locations, the flow can be seen going around (separating then re-attaching), what appears to be a separation bubble, and as the angle of attack increases past a particular threshold, the bubble becomes un-stable and separation of flow takes place at the leading of the wing at that span-wise location.

In the ensemble-averaged results at $\alpha = 15^\circ$ and $z/b = 0.46$, there is a small region ($\sim 0.25c$ in length), that appears over the leading edge of the airfoil, with strong velocity gradients in the vertical direction ($\bar{v} \sim 1.4\bar{U}_\infty$), Figure 3-36A. This appears to be valid since the normal component of the velocity would be strongest at the core of the wing-tip vortex, and at $x/c \sim 0.4$. This also goes to show that the phenomenon of high span-wise vorticity in pockets at the leading edge of the wing near the wing-tips could be the result of a complex interaction of the laminar flow over the airfoil and the circulatory flow induced by the wing-tip vortices.

The 3-component PIV results at $\alpha = 15^\circ$ also show the development and downstream progression of the wing tip vortex. The stream-wise vorticity, ω_u , in the center of the wing-tip vortex grows consistently stronger between $x/c = 0.3$ and $x/c = 0.6$, where it peaks. However, between the measurements at $x/c = 0.7$ and $x/c = 1.1$, the vorticity in the center of the wing-tip vortex grows weaker by 9-12% than what it was at $x/c = 0.6$.

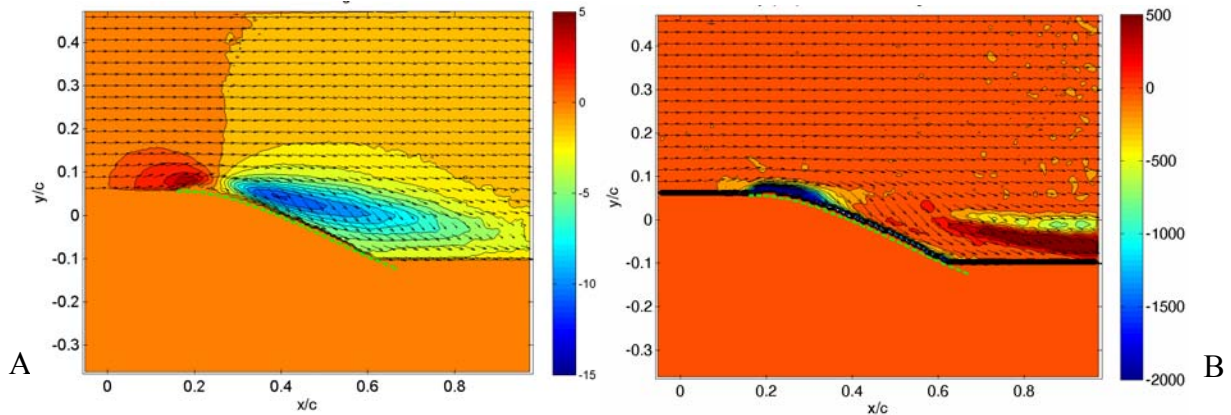


Figure 3-36. Distribution of the vertical component of the flow at $\alpha = 15^\circ$; A) showing a sharp velocity gradient in the stream-wise direction (m/s) and B) the vorticity at the LE of the airfoil, ω_z (s^{-1}).

As was previously discussed, it is first noted at $\alpha = 15^\circ$, that there is some negative stream-wise vorticity just above the wing surface and over the portion of the wing that forms the dihedral (Figure 3-8). However, the phenomenon of span-wise circulation is better observed at slightly higher angles of attack. Figure 3-11A, depicts the span-wise component of the flow at $\alpha = 18^\circ$ while Figure 3-11B depicts the development of the wing-tip vortex and span-wise circulation as the flow progresses downstream. Figure 3-37 shows the previously discussed phenomenon of span-wise circulation and stream-wise vorticity over the wing at $\alpha = 21^\circ$.

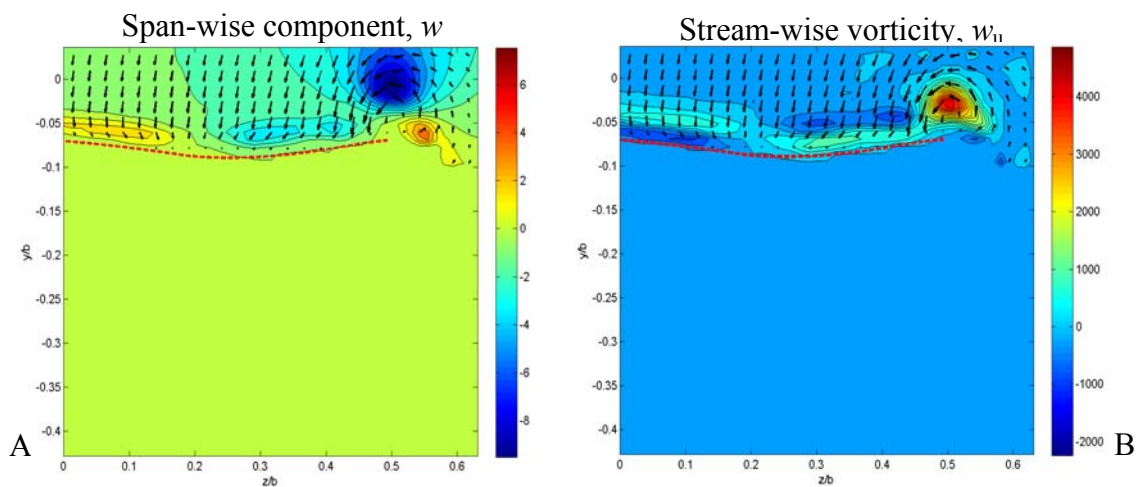


Figure 3-37. Distribution of the span-wise component (A), and the stream-wise vorticity (B), in the flow field at $\alpha = 21^\circ$.

At $\alpha = 25^\circ$ and at $z/b = 0.42$, the flow appears to separate at the leading edge of the airfoil, then re-attach behind it, creating high levels of span-wise vorticity within the separation bubble. However, in the ensemble-averaged data collected at $z/b = 0.46$ for the same angle of attack, this bubble appears to be unstable, leading to separation of the flow over the wing, and again creating high vorticity levels near the point of separation.

At $\alpha = 30^\circ$, the flow has fully separated over the entire span of the wing and the regions of highest span-wise vorticity, reside close to the point of separation over the airfoil and in the early stages of the separated shear layer, where the velocity gradients are the largest.

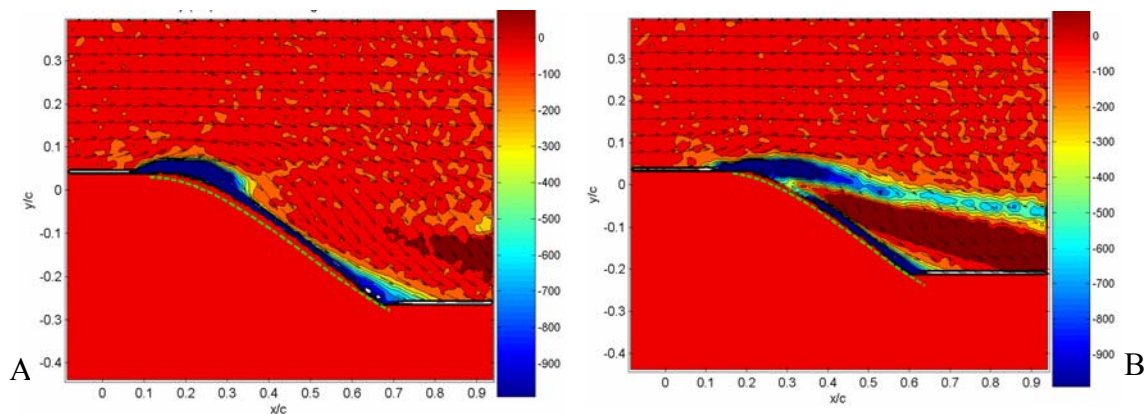


Figure 3-38. Span-wise vorticity, ω_z (s^{-1}), at $\alpha = 25^\circ$ and at: A) $z/b = 0.42$ and B) $z/b = 0.46$.

CHAPTER 4 SUMMARY AND CONCLUSIONS

Flow measurements were conducted over a thin rigid MAV wing using 2 & 3-component PIV techniques. The MAV wing has a wingspan of 0.15 m and a nominal chord length of 0.124 m. Experiments were conducted at various angles of attack and at a Reynolds number of $\sim 75,000$ based on the chord length of the wing model. A Dantec Dynamics TR PIV system was used to acquire the data from the experiments. The raw images were then processed using FlowManager v4.71 to obtain 2 & 3-component velocities from the two different setups. The precision error in the measurements was $\sim 2.8\%$ for the 2-component PIV setup and $\sim 1.04\%$ for the 3-component PIV setup.

The flow over the wing was described using figures depicting the mean velocity field, the fluctuating velocities in the three components of the flow, the turbulent shear stress levels and the out of plane vorticity. Spatial cross correlations were also performed on the results to try and identify turbulent length scales within the flow.

The mean velocity fields over the airfoil at various angles of attack showed that the thickness of the shear layer and the fluctuating velocity levels contained within it, undergo noticeable reduction at an angle of attack of 18° . The flow over the wing, visibly separates from the top surface of the airfoil between $21^\circ \leq \alpha \leq 25^\circ$. At $\alpha = 25^\circ$, a stable separation bubble is observed at the leading edge of the airfoil at $z/b = 0.42$ and an unstable separation bubble is observed at the leading edge of the wing at $z/b = 0.46$. The flow measurements also identified regions of span-wise circulation over the wing caused by the wing-tip vortices. It was also observed that with an increase in the angle of attack, there was an increase in the magnitude of the downward velocities over the top of the wing, due to stronger wing-tip vortices.

The downwash of the flow over the wing causes the vortex core to shift down as well, therefore, the higher the angle of attack, the stronger the downwash and the greater the shift. It was also interesting to note, that the turbulence levels drop unexpectedly just behind the trailing edge of the wing ($x/c = 1.0$), but suddenly increase in magnitude thereafter ($x/c = 1.1$), after which they subside by the time the flow reaches $x/c = 1.4$. Another unique characteristic was the formation of ensemble-averaged turbulent regions just off to the side of the wing tip vortex, at $1.1 \leq x/c \leq 1.2$, and how quickly it disappears by the time the flow reaches $x/c = 1.4$. It is possible that perhaps there is some vortex shedding taking place in the wake of the wing-tip vortices.

The spatial cross correlations provided insight into the turbulent length scales within the shear layer and the region of separated flow behind the wing. It appears that fluctuating velocity levels contained within the shear layer have good correlation. The turbulent length scales also validated regions of interest that had been identified from the flow measurements, the fluctuating velocity and vorticity calculations; for instance, the span-wise circulation on the top surface of the wing.

Although this research represented quite an extensive study, there are still many improvements and additions that could be undertaken:

- In terms of improvements from the existing data, the most glaring one would be to acquire the velocities near the wall for the stream-wise aligned measurements. There are several ways in which this might be accomplished which would include changing the angle of the camera to overcome the blockage caused by the dihedral of the wing and coating/painting the wing so that the blooming of the laser light is minimized.
- It would also be beneficial to measure all three components of the velocity in the x-y plane so that one can observe how the span-wise velocity affects the separation characteristics along the wing.
- The acquisition of time resolved measurements so that the time dependence of the many features in the flow may be examined more closely; such as, the angle of attack and the

point over the wing surface where massive separation occurs. This would also provide some insight into observing how steady or unsteady the closed separation bubble is.

- In terms of additional processing it would be nice to analyze the data in such a manner that a better three dimensional description of the flow field could be extracted from the measurements.

This clearly is only the first step in examining the flow over MAV wings and will serve as a set of baseline measurements for which to compare the various compliant wing structures that have been developed by the University of Florida MAVLAB such as the perimeter and batten reinforced configurations.

LIST OF REFERENCES

- Abdulrahim M. 2004. *Dynamic Characteristics of Morphing Micro Air Vehicles*. Master's Thesis. University of Florida, Gainesville. 69 pp.
- Abdulrahim M, Albertani R, Barnswell P, Boria F, Claxton D, Chifton J, Cocquyt J, Lee KH, Mitryk S, Ifju P. 2003. *Design of the University of Florida Surveillance and Endurance Micro Air Vehicles*. University of Florida, Gainesville.
- Adrian RJ. 1991. Particle-Imaging Techniques for Experimental Fluid Mechanics. *Annu. Rev. Fluid Mech.* Vol. 23:261-304.
- Albertani R. 2005. *Experimental Aerodynamic and Static Elastic Deformation Characterization of Low Aspect Ration Flexible Fixed Wings Applied to Micro Aerial Vehicles*. Ph.D. dissertation. University of Florida, Gainesville. 317 pp.
- Albertani R, Barnswell P, Boria F, Claxton D, Clifton J, Cocquyt J, Crespo A, Francis C, Ifju P, Johnson B, Jung S, Lee KH, Morton M. 2004. *University of Florida Biologically Inspired Micro Air Vehicles*. University of Florida, Gainesville.
- Albertani R, Boria F, Bowman S, Claxton D, Crespo A, Francis C, Ifju P, Johnson B, Lee KH, Morton M, Sytsma M. 2005. *Development of Reliable and Mission Capable Micro Air Vehicles*. University of Florida, Gainesville.
- Ansari SA, Zbikowski R, Knowles K. 2006. Aerodynamic Modeling of Insect-like Flapping Flight for Micro Air Vehicles. *Progress in Aerospace Sciences*. Vol. 42, Issue 2:129-172.
- Aubepart F, Franceschini N. 2007. Bio-inspired Optic Flow Sensors Based on FPGA: Application to Micro Air Vehicles. *Microprocessors and Microsystems*. Vol. 31, Issue 6:408-419.
- Banerjee JR. 1984. Flutter Characteristics of High Aspect Ratio Tailless Aircraft. *Journal of Aircraft*. Vol. 21, No. 9:733-736.
- Belser II TL. 2006. *Image Segmentation and Object Tracking for A Micro Air Vehicle*. Master's Thesis. University of Florida, Gainesville. 44 pp.
- Bennett RM, Farmer MG, Mohr RL, Hall Jr. WE. 1978. Wind-Tunnel Technique for Determining Stability Derivatives from Cable-Mounted Models. *Journal of Aircraft*. Vol. 15, No. 5:304-310.
- Biswas G, Eswaran V. 2002. *Turbulent Flows: Fundamentals, Experiments and Modeling*. Alpha Science International. Indian Institute of Technology, Kanpur, India.
- Brandon JM, Jordan, Jr. FL, Stuever RA, Buttrill CW. 1997. Application of Wind Tunnel Free-Flight Technique for Wake Vortex Encounters. *NASA Technical Paper*. Vol. 3672:74.

- Brendel M, Mueller TJ. 1988. Boundary Layer Measurements on an Airfoil at Low Reynolds Numbers. *Journal of Aircraft*. Vol. 25, No. 7:612-617.
- Causey RS. 2003. *A Lateral Vision-Based Control Autopilot for Micro Air Vehicles Using a Horizon Detection Approach*. Master's Thesis. University of Florida, Gainesville. 69 pp.
- Claxton DJ. 2007. *Development of a Parametric Software Tool for the Design and Manufacturing of Micro Air Vehicles*. Master's Thesis. University of Florida, Gainesville. 79 pp.
- Claxton D, Johnson B, Stanford B, Sytsma M. 2006. *Development of a Composite Bendable-Wing Micro Air Vehicle*. 2006 International Micro Air Vehicle Competition, Brigham Young University, Provo, Utah.
- Cosyn P, Vierendeels J. 2005. *Numerical Investigation of Low Aspect Ratio Wings at Low Reynolds Numbers*. AIAA 2005-4609. Paper presented at the 23rd AIAA Applied Aerodynamics Conference, Toronto, Canada.
- Culbreth M, Esterhuizen S, Gardner R, Mihok B, Russell S, Stewart B. 2003. *CMAV: Colorado Micro Air Vehicle Critical Design Review*. Project presented at the University of Colorado at Boulder.
- Galvao R, Israeli E, Song A, Tian X, Bishop K, Swartz S, Breuer K. 2006. *The Aerodynamics of Compliant Membrane Wings Modeled on Mammalian Flight Mechanics*. AIAA 2006-2866. Paper presented at 36th AIAA Fluid Dynamics Conference and Exhibit. Brown University, Providence, Rhode Island.
- George WK, Beuther PD, Shabbir A. 1987. *Polynomial Calibrations for Hot Wires in Thermally Varying Flows*. 1987 ASME Applied Mechanics, Bioengineering and Fluids Engineering Conference, FED-Vol. 53:3-6.
- Gharib M, Pereira F, Dabiri D, Hove JR, Modarress D. 2002. Quantitative Flow Visualization: Toward a Comprehensive Flow Diagnostic Tool. *Integr. Comp. Biol.* Vol. 42:964-970.
- Grant I. 1997. Particle Image Velocimetry: A Review. *Proc Instn. Mech. Engrs*. Vol. 211, Part C:55-76.
- Green WE, Oh PY. 2005. *A MAV That Flies Like an Airplane and Hovers Like a Helicopter*. Paper presented at the International Conference on Advanced Intelligent Mechatronics, Monterey, California. IEEE/ASME. Pp: 693-698.
- Grzywna JW. 2004. *A Flight Testbed with Virtual Environment Capabilities for Developing Autonomous Micro Air Vehicles*. Master's Thesis. University of Florida, Gainesville. 44 pp.
- Hanff ES. 2004. PIV Application in Advanced Low Reynolds Number Facility. *IEEE Transactions on Aerospace and Electronic Systems*. Vol 40, No. 1:310-319.

- Ho S, Nassef H, Pornsin-Sirirak N, Tai YC, Ho CM. 2002. ICAS2002 Congress. *Flight Dynamics of Small Vehicles*. Pp. 551.1-551.10.
- Ho S, Nassef H, Pornsin-Sirirak N, Tai YC, Ho CM. 2003. Unsteady Aerodynamics and Flow Control for Flapping Wing Flyers. *Progress in Aerospace Sciences* 39. Pp. 635-681. Elsevier Ltd.
- Hoerner SF, Borst HV. 1975. *Fluid-dynamic lift: Practical information on aerodynamic and hydrodynamic lift*. Research supported by the U.S. Navy; Brick Town, N.J., Hoerner Fluid Dynamics, pp. 505.
- Hoffman JM, Arnette SA, Porter CB, Sung B, Arik BE. 2000. Application of Particle Image Velocimetry in the Korea Aerospace Research Institute Low Speed Wind Tunnel. AIAA 2000-0411. 38th Aerospace Sciences Meeting and Exhibit, Reno, NV.
- Horton, HP. 1968. *Laminar Separation Bubbles in Two and Three-Dimensional Incompressible Flows*. Ph.D. dissertation. University of London.
- Jackowski JJ. 2004. *Nonlinear Simulation of a Micro Air Vehicle*. Master's Thesis. University of Florida, Gainesville. 70 pp.
- Jain A. 2005. *Optical Flow Based Obstacle Avoidance for Micro Air Vehicles*. Master's Thesis. University of Florida, Gainesville. 42 pp.
- Johnson B, Claxton D, Stanford B, Jagdale V, Ifju P. 2007. Development of a Composite Bendable-Wing Micro Air Vehicle. AIAA 2007-1044. 45th Aerospace Sciences Meeting and Exhibit, Reno, NV.
- Jonassen D, Settles GS, Tronosky MD. 2006. Schlieren "PIV" for Turbulent Flows. *Optics and Lasers in Engineering*. Vol. 44:190-207.
- Jones KD, Nakashima M, Bradshaw CJ, Papadopoulos J, Platzer MF. 2003. *On Flow Separation Control by Means of Flapping Wings*.
- Jung S. 2004. *Design and Development of Micro Air Vehicles (MAV): Test-Bed for Vision-Based Control*. Master's Thesis. University of Florida, Gainesville. 66 pp.
- Kaplan SM, Altman A, Ol M. 2007. Wake Vorticity Measurements for Low Aspect Ratio Wings at Low Reynolds Number. *Journal of Aircraft*. Vol. 44, No. 1:241-251.
- Karakus C, Akilli H, Sahin B. 2007. Formation, Structure, and Development of Near-Field Wing Tip Vortices. *Proc. IMechE*. Vol. 222, Part G: J. Aerospace Engineering:13-22.
- Keane RD, Adrian RJ. 1993. *Theory of Cross-Correlation Analysis of PIV Images*. Kluwer Academic Publishers, Netherlands.

- Khambatta P, Ukeiley L, Tinney C, Stanford B, Ifju P. 2008. Flow Characteristics of a Three-Dimensional Fixed Micro Air Vehicle Wing. AIAA 2008-3820. 38th Fluid Dynamics Conference and Exhibit, Seattle, WA.
- Kurtulus DF, Scarano F, David L. 2006. Unsteady Aerodynamic Forces Estimation on a Square Cylinder by TR-PIV. *Experiments in Fluids*. Vol. 42:185-196.
- Lian Y. 2003. *Membrane and Adaptively-Shaped Wings for Micro Air Vehicles*. Ph.D. dissertation. University of Florida, Gainesville. 126 pp.
- Lian Y, Shyy W, Viieru D, Zhang B. 2003. Membrane Wing Aerodynamics for Micro Air Vehicles. *Progress in Aerospace Sciences*. Vol. 39:425-465.
- Lin JL, Wei CY, Lin CY. 2007. Aerodynamic Performance of Thin Wings at Low Reynolds Numbers. *Aircraft Engineering and Aerospace Technology: An International Journal*. Vol. 79, No. 3:245-253.
- Lissaman PBS. 1983. Low-Reynolds-Number Airfoils. *Annual Review of Fluid Mechanics*. Vol. 15:223-239.
- Lourenco L, Krothapalli A. 1995. On the Accuracy of Velocity and Vorticity Measurements with PIV. *Experiments in Fluids*. Vol. 18:421-428.
- Lourenco L, Subramanian S, Ding Z. 1997. Time Series Velocity Field Reconstruction from PIV Data. *Meas. Sci. Technol.* Vol. 8:1533-1538.
- McKenna SP, McGillis WR. 2002. Performance of Digital Image Velocimetry Processing Techniques. *Experiments in Fluids*. Vol. 32:106-115.
- Meinhart C, Wereley S. 2003. The Theory of Diffraction-Limited Resolution in Microparticle Image Velocimetry, *Measurement Science and Technology*, Vol. 14, No. 2:1047-1053.
- Meinhart CD, Wereley JG, Santiago JG. 1999. PIV Measurements of a Microchannel Flow. *Experiments in Fluids*. Vol. 27:414-419.
- Melling A. 1997. Tracer Particles and Seeding for Particle Image Velocimetry. *Meas. Sci. Technol.* Vol. 8:1406-1416.
- Molezzi MJ, Dutton JC. 1993. Application of Particle Image Velocimetry in High Speed Separated Flows. *AIAA Journal*. Vol. 31, No. 3:438-446.
- Morse DR, Liburdy JA. 2006. *Dynamic Characteristics of Flow Separation from a Low Reynolds Number Airfoil*. Paper presented at Joint ASME/JSME Fluids Engineering Conference. FEDSM2007-37083.

- Mueller TJ. 1985. Low Reynolds number vehicles. In *Advisory Group for Aerospace Research and Development AGARD-AG-288*, ed. E Reshotko. Essex: Spec. Print. Serv. Ltd. 69 pp.
- Mueller TJ. 1999. *Aerodynamic Measurements at Low Reynolds Numbers for Fixed Wing Micro-Air Vehicles*. Paper presented at the RTO AVT/VKI Special Course on Development and Operation of UAVs for Military and Civil Applications.
- Mueller TJ. 1985. The Influence of Laminar Separation and Transition on Low Reynolds Number Airfoil Hysteresis. *Journal of Aircraft*. Vol. 22, No. 9:763-770.
- Mueller TJ, DeLaurier JD. 2003. Aerodynamics of Small Vehicles. *Annual Review Fluid Mechanics*. Vol. 35:89-111.
- Mueller TJ, Kellogg JC, Ifju PG, Shkarayev SV. 2007. Introduction to the Design of Fixed-Wing Micro Air Vehicles. *American Institute of Aeronautics and Astronautics, AIAA Education Series*.
- Murray N, Ukeiley L, Raspet R. 2007. Calculating Surface Pressure Fluctuations From PIV Data Using Poisson's Equation. AIAA 2007-1306. 45th AIAA Aerospace Sciences Meeting and Exhibit, Reno, NV.
- Muti Lin JC, Pauley LL. 1996. Low Reynolds-Number Separation on an Airfoil. *AIAA Journal*. Vol. 34, No. 8:1570-1577.
- OI MV, McAuliffe BR, Hanff ES, Scholz U, Kahler C. 2005. Comparison of Laminar Separation Bubble Measurements on a Low Reynolds Number Airfoil in Three Facilities. AIAA-2005-5149. 23rd AIAA Applied Aerodynamics Conference, Toronto.
- O'Meara MM, Mueller TJ. 1987. Laminar Separation Bubble Characteristics on an Airfoil at Low Reynolds Numbers. *AIAA Journal*. Vol. 25, No. 8:1033-1041
- Ortega JM, Bristol RL, Savas O. 2002. Wake Alleviation Properties of Triangular-Flapped Wings. *AIAA Journal*. Vol. 40, No. 4:709-721.
- Plew J. 2004. *Development of Flight Avionics System for an Autonomous Micro Air Vehicle*. Master's Thesis. University of Florida, Gainesville. 88 pp.
- Pornsirakorn TN, Lee SW, Nassef H, Grasmeyer J, Tai YC, Ho CH, Keennon M. 2000. *MEMS Wing Technology for a Battery-Powered Ornithopter*. Presented at Int. Conf. Micro Electro Mech. Syst., IEEE, 18th, Miyazaki, Japan.
- Prasad AK. 2000. Particle Image Velocimetry. *Current Science*. Vol. 79, No. 1: 51-60.
- Prasad AK. 2000. Stereoscopic Particle Image Velocimetry. *Experiments in Fluids*. Vol. 29: 103-116.

- Quenot GM, Pakleza J, Kowalewski TA. 1998. Particle Image Velocimetry with Optical Flow. *Experiments in Fluids*. Vol. 25:177-189.
- Sane SP. 2003. The Aerodynamics of Insect Flight. *The Journal of Experimental Biology*. Vol. 206:4191-4208.
- Santiago JG, Werely ST, Meinhart DC, Beebe DJ, Adrian RJ. 1998. A Particle Image Velocimetry System for Microfluidics. *Experiments in Fluids*. Vol. 25:316-319.
- Scheimpflug T. 1904. Improved Method and Apparatus for the Systematic Alteration or Distortion of Plane Pictures and Images by Means of Lenses and Mirrors for Photography and for other purposes. GB Patent No. 1196. Filed 16 January 1904, and issued 12 May 1904.
- Schmitz FW. 1980. The Aerodynamics of Small Reynolds Numbers. *NASA Technical Reports Server*. NTRS: 2005-10-13.
- Selig MS, Guglielmo JJ. 1997. High-Lift Reynolds Number Airfoil Design. *Journal of Aircraft*. Vol. 34, No. 1:72 – 79.
- Shih C, Lourenco LM, Krothapalli A. 1995. Investigation of Flow at Leading and Trailing Edges of Pitching-Up Airfoil. *AIAA Journal*. Vol. 33. No. 8:1369-1376.
- Shortal JA, Osterhout CJ. 1941. Preliminary Stability and Control Tests in the NACA Free-Flight Wind Tunnel and Correlation with Full-Scale Flight Tests. *National Advisory Committee for Aeronautics*. Technical Note No. 810.
- Shyy W, Ifju P, Viieru D. 2005. Membrane Wing-Based Micro Air Vehicles. *Applied Mechanics Reviews*, Vol. 58, No. 4:283-301.
- Stanford B, Lind R, Ifju P. 2007. Membrane Micro Air Vehicles with Adaptive Aerodynamic Twist: Numerical Modeling. AIAA 2007-1758. 48th AIAA/ASME/ASCE/AHS/ASC Structures, Structural Dynamics, and Materials Conference, Honolulu, Hawaii
- Stanford B, Sytsma M, Albertani R, Viieru D, Shyy W, Ifju P. 2007. Static Aeroelastic Model Validation of Membrane Micro Air Vehicle Wings. *AIAA Journal*. Vol. 45, No. 12.
- Sriram AP, Van Der Weide E, Kim S, Tomlin C, Jameson A. 2005. *Aerodynamics and Flight Control of Flapping Wing Flight Vehicles: A Preliminary Computational Study*. Paper presented at the 43rd Aerospace Sciences Meeting, Reno, Nevada.
- Stubbs MD. 2003. *Kinematic Design and Analysis of a Morphing Wing*. Master's Thesis. Virginia Polytechnic Institute and State University, Blacksburg, Virginia. 82 pp.

- Suhariyono A, Kim JH, Goo NS, Park HC, Yoon KJ. 2005. Design of Precision Balance and Aerodynamic Characteristic Measurement System for Micro Air Vehicles. *Aerospace Science and Technology*. Vol. 10:92-99.
- Sytsma MJ. 2006. *Aerodynamic Flow Characterization of Micro Air Vehicles Utilizing Flow Visualization Methods*. Master's Thesis. University of Florida, Gainesville. 152 pp.
- Tamai M, Murphy JT, Hu H. 2008. An Experimental Study of Flexible Membrane Airfoils at Low Reynolds Numbers. AIAA 2008-580. 46th AIAA Aerospace Sciences Meeting and Exhibit, Reno, NV.
- Tang J, Zhu K. 2004. Numerical and Experimental Study of Flow Structure of Low-Aspect-Ratio Wing. *Journal of Aircraft*, Vol. 41, No. 5:1196-1201.
- Torres G. 2002. *Aerodynamics of Low Aspect Ratio Wings at Low Reynolds Numbers with Applications to Micro Air Vehicle Design*. Ph.D. Dissertation. University of Notre Dame, South Bend, IN. 250 pp.
- Torres GE, Mueller TJ. 2004 Low-Aspect-Ratio Wing Aerodynamics at Low Reynolds Numbers. *AIAA Journal*. Vol. 42, No. 5:865 - 873.
- Unal MF, Lin JC, Rockwell D. 1997. Force Prediction by PIV Imaging: A Momentum-based Approach. *Journal of Fluids and Structures*. Vol. 11:965-971.
- Viiiru D. 2006. *Flapping and Fixed Wing Aerodynamics of Low Reynolds Number Flight Vehicles*. Ph.D. dissertation. University of Florida, Gainesville. 135 pp.
- Wanstrom M, George WK, Meyer KE, Westergaard C. 2007. *Identifying Sources of Stereoscopic PIV Measurements Errors on Turbulent Round Jets*. Paper presented at the 5th Joint ASME/JSME Fluids Engineering Conference, San Diego, California.
- Westerweel J. 1997. Fundamentals of Digital Particle Image Velocimetry. *Meas. Sci. Technol.* Vol. 8:1379-1392.
- Westerweel J. 2000. Effect of Sensor Geometry on the Performance of PIV Interrogation. *Laser Techniques Applied to Fluid Mechanics*, (Eds. Adrian, R.J., Durao, D.F.G., Durst, F., Heitor, M.V., Maeda, M., Whitelaw, J.H.), Berlin: Springer.
- Westerweel J, Dabiri D, Gharib M. 1997. The Effect of a Discrete Window Offset on the Accuracy of Cross-Correlation Analysis of Digital PIV Recordings. *Experiments in Fluids*. Vol. 23:20-28.
- Willert CE, Gharib M. 1991. Digital Particle Image Velocimetry. *Experiments in Fluids*. Vol. 10:181-193.

- Willert C, Raffel M, Kompenhans J, Stasicki B, Kahler C. 1997. Recent Applications of particle Image Velocimetry in Aerodynamic Research. *Flow Meas. Instrum.* Vol. 7. No. 3/4: 247-256.
- Young A, Horton H. 1966. Some Results of Investigation of Separation Bubbles. *AGARD Conference Proceedings*, No. 4:779-811.
- Zbikowski R, Ansari SA, Knowles K. 2006. On Mathematical Modeling of Insect Flight Dynamics in the Context of Micro Air Vehicles. *Bioinspiration and Biomimetics*. Vol. 1, No. 2:R26-R37.
- Zhang HJ, Zhou Y, Whitelaw JH. 2006. Near-Field Wing-Tip Vortices and Exponential Vortex Solution. *Journal of Aircraft*. Vol. 43, No. 2:445-449.
- Zhu R, Sun D, Zhou Z. 2007. Integrated Design of Trajectory Planning and Control for Micro Air Vehicles. *Mechatronics*. Vol. 17, Issue 4-5:245-253.

BIOGRAPHICAL SKETCH

Parvez Khambatta was born in a military hospital in Mhow, Indore, India in 1982. Starting from a very young age, Parvez had a love for airplanes. This fascination with flight led Parvez into the field of physics and engineering. Parvez secured a full scholarship to Muskingum College in August 2000 and enrolled into the Muskingum-Case Western Reserve University binary program in 2003. In 2005, Parvez graduated with his Bachelor of Science degrees in mechanical engineering and physics from Case Western Reserve University and Muskingum College. He then enrolled into the master's program at the University of Florida in Spring 2006, where he worked initially with Dr. Rick Lind in controls and systems engineering. He later transferred to the University of Florida Research and Engineering Education Facility to continue his education in fluid dynamics with Dr. Lawrence Ukeiley. Parvez currently resides in Fort Walton Beach, Florida with his wife, Jamie, and their dog, Winston.